ABSTRACT

Title: QUANTITATIVE GLOBAL HEAT-TRANSFER MEASUREMENTS USING TEMPERATURE-SENSITIVE PAINT ON A BLUNT BODY IN HYPERSONIC FLOWS

Inna Kurits
Master of Science, 2008

Directed by: Professor Mark J. Lewis
Department of Aerospace Engineering

A quantitative global intensity-based temperature-sensitive paint heat-transfer measurement system has been developed for use in the US Air Force Hypervelocity Wind Tunnel No. 9. Several data reduction approaches have been proposed for calculating the convective heat flux from the temperature-sensitive paint emission intensity data. The validity of the underlying assumptions and the sensitivity of the algorithms to perturbations in various system parameters have been analyzed numerically. Finally, the temperature-sensitive paint emission intensity data have been collected on a model of a NASA Crew Exploration Vehicle capsule in Mach 10 flow. The proposed data reduction algorithms have been applied to obtain an estimate of the thermal conductivity of the coating as a function of temperature and to generate high-resolution quantitative heat-transfer maps of the model's heat shield. On the majority of the heat shield surface, a good agreement between the heat-transfer maps and the baseline conventional instrumentation data has been revealed.

QUANTITATIVE GLOBAL HEAT-TRANSFER MEASUREMENTS USING TEMPERAURE-SENSITIVE PAINT ON A BLUNT BODY IN HYPERSONIC FLOWS

By

Inna Kurits

Thesis submitted to the Faculty of the Graduate School of the
University of Maryland, College Park, in partial fulfillment
of the requirements for the degree of
Master of Science
2008

Advisory Committee:
Professor Mark J. Lewis, Chair
Associate Professor Christopher Cadou
Associate Professor Kenneth Yu

Acknowledgements

I would like to extend my gratitude to Dr. Mark J. Lewis and the AEDC Hypervelocity Wind Tunnel No. 9 team for presenting me with the unique opportunity to conduct this research. Without their support and dedication this work would not have been possible. I would also like to thank Mr. Joseph D. Norris, Dr. Marvine P. Hamner, and Mr. Joe J. Coblish for their continuous guidance through all of the challenges I encountered along the way. Special thanks to my family and friends for their endless moral support and patience throughout my academic endeavors.

Table of Contents

List of Tables

List of Figures

List of Symbols

Roman Symbols

C_p	specific heat
c_p	specific heat of nitrogen at constant pressure, 0.248 BTU/lbm-°R
Fo	Fourier number
H_o	calculated total enthalpy, BTU/lbm
K	thermal conductivity
L	paint layer thickness
M_∞, M_{inf}	freestream Mach number
P_o	total pressure
P_∞, P_{inf}	freestream pressure
Q_{inf}	freestream dynamic pressure
$qdot$, $\dot{q}$	heat-transfer rate per unit area
R	radius of the heat shield
R^2	linear fit correlation coefficient squared
Re	unit Reynolds number, 1/length
r	radius of curvature
S	singlet state
s	distance along model's surface
Slp	slope
St	Stanton number
T	temperature
T	triplet state
T_{inf}	freestream temperature
T_o	total temperature
∇T	temperature gradient
t	time
U_{inf}, u	freestream velocity
x	distance normal to model's surface

Greek Symbols

α	thermal diffusivity
ρ	freestream density
Δt	time step
Δr, Δx	element size through the model wall in the numerical model

Superscripts

st	steel
tsp	TSP

Subscripts

i	time index
j	spatial (node) index
surf	surface
w	wall

Abbreviations

1D	one-dimensional
2D	two-dimensional
3D	three-dimensional
AEDC	Arnold Engineering and Development Center
A/D	analog to digital
CAM1	first camera, imaged the heat shield
CAM2	second camera, imaged the aft-cone
CCD	charge-coupled device
CEV	Crew Exploration Vehicle
CFD	computational fluid dynamics
CIC	clock induced charge
CUBRC	Calspan-University of Buffalo Research Center
EMCCD	electron multiplied charge-coupled device
FWHM	full width at half maximum
IC	internal conversion process
ISC	intersystem crossing process
JAXA	Japanese Aerospace Exploration Agency
LaRC	Langley Research Center
LENS	Large Energy National Shock Tunnel
NASA	National Aeronautics and Space Administration
PSP	pressure-sensitive paint
STS	space transportation system
TSP	temperature-sensitive paint
UV	ultraviolet

Units of Measurement

Btu	British thermal unit
Btu/ft^2 s	British thermal units per feet squared per second
Btu/in^2 s	British thermal units per inch squared per second
°C	degrees, Celcius
deg	degrees
deg/s	degrees per second
°F	degrees, Fahrenheit
fps	frames per second
ft	feet
ft/sec	feet per second
Hz	Hertz

in.	inch(es)
kg	kilogram
K	degrees, Kelvin
mil	thousandth of an inch
m/s	meters per second
mmHg	millimeters of Mercury
ms	millisecond
nm	nanometer
psia	pounds per square inch absolute
°R, degR	degrees, Rankine
s, sec	second
torr	pressure unit ≈ mmHg
μm	micrometer
W	watt
/ft	per foot

Chapter 1. Introduction

1.1. Motivation

Surface heat transfer is a critical design parameter for most vehicles that are expected to experience high aerodynamic heating loads for at least a portion of their trajectories. This includes the majority of hypersonic vehicles. For instance, heat-transfer rates are extremely important when designing a thermal protection system for an atmospheric reentry vehicle, such as the NASA Crew Exploration Vehicle (CEV). Ground test facilities, e.g. wind tunnels, are an important tool in the design and evaluation of future air- and spacecraft. They provide the capability to simulate segments of a vehicle's flight envelope and measure quantities essential for vehicle design process as well as for CFD code validation. More specifically, ground test facilities provide the capability to measure pressure, force, moment, and heat-transfer coefficients on parts or whole vehicle geometries.

The most common methods of heat-transfer measurements in ground test facilities involve discrete instrumentation, such as thermocouples or direct-reading heat-transfer gages. While these methods are well-established, they can only provide measurements at discrete locations. This makes important flow phenomena such as boundary layer transition, flow separation, and shock/boundary layer interactions hard to detect. These types of phenomena typically exhibit strong spatial gradients, thus making it difficult to resolve them using discrete measurements unless the instrumentation density is very high or there is an indication prior to the test of where the phenomena of interest may occur. In addition, installing large arrays of discrete instrumentation is not cost effective and can be labor-intensive, and some model areas such as control surfaces and leading edges may be

hard or impossible to instrument with discrete sensors. Discrete instrumentation tends to be intrusive, so great care must be taken to not alter surface geometry of a test article during the installation process.

Global heat-transfer measurement systems, on the other hand, are typically less intrusive and can provide high-resolution qualitative as well as quantitative heat-transfer maps of an entire model surface. In addition, they can be applied to almost any model shape, usually at a lower cost per application. The present work deals with the development of such a global heat-transfer measurement system for the use at Arnold Engineering and Development Center (AEDC) Hypervelocity Wind Tunnel No. 9. In particular, the work concentrates on the development and validation of the data processing and reduction algorithms for the system.

1.2. Review of Global Measurement Techniques

The majority of global temperature and heat-transfer measurement techniques can be grouped into four categories differentiated by the technology they employ: infrared camera imaging, liquid crystals, thermographic phosphors, and temperature-sensitive paints. This section provides a brief summary of each in the context of temperature and heat-transfer measurements in high-speed wind tunnel flows. Additionally, a pressure-sensitive paint technique, which is closely related to temperature-sensitive paints, is briefly described.

1.2.1. Infrared Camera Imaging

Infrared imaging has been used since the 1970's for surface temperature and heat-transfer measurements. The technique requires little or no surface treatment and does not require any outside illumination sources, but rather relies exclusively on the radiation

emitted by objects due to their temperature (0.7 – 50 μm bandpass of electromagnetic spectrum).[1,2] This makes it the most suitable global measurement technique for flight testing since almost no vehicle modifications are required; however, the technique is still mostly applied in wind tunnel testing.[1] In this technique, an imager detects the infrared radiation emitted by a test object, where emissive power of an object is proportional to T^4 of the object. The detector's output is proportional to the object's surface temperature, which can be used to calculate the heat-transfer rate using an appropriate data reduction algorithm.[2]

Early infrared imagers suffered from low optical and temporal resolutions, and the data could be converted into absolute temperatures only by using a reference blackbody radiant source maintained at a specific temperature and located in the field of view of the imager. More modern infrared imagers have improved optical and temporal resolutions and are capable of absolute temperature measurements through the use of internal blackbody radiant sources. The technique can be applied to both metallic and nonmetallic wind tunnel models over a large temperature range (-30 – 1500 °C). However, metallic models usually have to be coated with a layer of black paint or other high-emittance coating to increase the low emittance values characteristic of metallic surfaces, which result in low signal-to-noise ratio.[2]

The analysis of the infrared image data requires the knowledge of the radiant properties, such as emittance and reflectance, of the test article's surface. In general, the emittance of a surface can depend on wavelength, temperature, direction, and surface conditions, such as roughness, oxide layers, physical and chemical contamination, and the grain structure in the case of dielectric materials.[2] The total hemispherical and normal

emittance data are extensively tabulated in the literature, but there are discrepancies between different sources mainly due to variations in the surface conditions of the test articles, so the emittance of the surface of each specific test article may need to be measured. Additionally, the knowledge of the transmission losses due to intervening media (e.g. wind tunnel windows) and the ambient temperature are required.[2]

In summary, the infrared imaging technique can be successfully applied to temperature and heat-transfer measurements in high temperature environments, including hypersonic wind tunnel flows, or for imaging of reentry vehicles. However, measurements at room temperatures, for example at the start of a wind tunnel run, are challenging due to relatively high levels of background radiation (i.e. low signal-to-noise ratio).[3] Additionally, the infrared thermography technique requires expensive equipment and special windows to minimize the transmission losses. The measurements are sensitive to a test article's emissivity and spectral characteristics, which can be hard to accurately measure and/or control.

Examples of infrared imaging use in flight testing at hypersonic speeds include the aerodynamic heating measurements on the lower surface of the Space Shuttle during reentry. The first successful infrared image was obtained in 1982 during the STS-3 mission. More recently, infrared imaging was used in support of the Shuttle Return-to-Flight mission to qualitatively capture the temperature increase associated with the hypersonic boundary layer transition on the Shuttle's windward surface.[4] Hypersonic wind tunnel tests employing an infrared imaging system in the NASA Langley Research Center (LaRC) 31-in. Mach 10 Tunnel on the 4-in.-diam. hemisphere model and a generic orbiter windward model are reported in Ref. 2.

A feasibility test was conducted at AEDC Hypervelocity Wind Tunnel No. 9 to determine whether it was possible to use a commercially available infrared imaging system for surface temperature measurements on typical untreated stainless steel models. An 8° half-angle cone model with a cylindrical protuberance was tested at Mach 14, and the resulting infrared measurements were compared to the standard coaxial thermocouple temperature measurements. It was concluded that accurate surface temperature measurements cannot be made with the commercial infrared imaging system due to low emittance of the untreated metal model surface. The results of this test are reported in Ref. 5.

1.2.2. Liquid Crystals

The use of liquid crystals for temperature and shear stress measurements was first investigated in the late 1960's and is described in Refs. 6 and 7. Their application in hypersonic flows was first reported in the late 1970's in Ref. 8. At present, liquid crystal thermography is widely used in low-speed flows with low heat fluxes. In this technique liquid crystals are applied to a model's surface in a thin layer. When the coating is illuminated with a white light source, the color of the reflected light is a function of temperature. Subsequently, the surface temperature can be used to calculate the heat transfer using an appropriate data reduction algorithm.[9]

In general, the technique is relatively cheap and simple to implement, but there are certain difficulties and limitations especially when applied in hypersonic environments. Nevertheless, with careful planning and data analysis the technique can produce high-fidelity results even for high-speed high-heat-transfer tests.[9] A brief summary of how liquid crystal thermography works and some of its limitations as applied

to hypersonic wind tunnel testing are presented below. For a more detailed description refer to Ref. 9.

The property of liquid crystals to change color depending on temperature is due to their molecular structure. The molecules are thin, rod-like structures that in the non-isotropic liquid form (i.e. temperature-sensitive phase) have their long axes aligned in a certain direction. Temperature variations cause the molecules to gradually change their alignment directions from one layer to the next to form a helical configuration, as illustrated in Fig. 1. In other words, temperature changes cause changes in the helical pitch of the structure, which causes the reflected wavelength, and hence the color, to change. When heated, the liquid crystals will transform from the optically inactive (colorless) phase to the optically active (chiral nematic) phase through the visible light spectrum and then turn colorless again at high temperatures as the crystals undergo a second phase change to an isotropic liquid structure. The color variation with temperature is nonlinear, with red usually occupying a rather small temperature range and blue a much larger range. The composition of the coating can be adjusted to fit different temperature ranges and sensitivity requirements.[9]

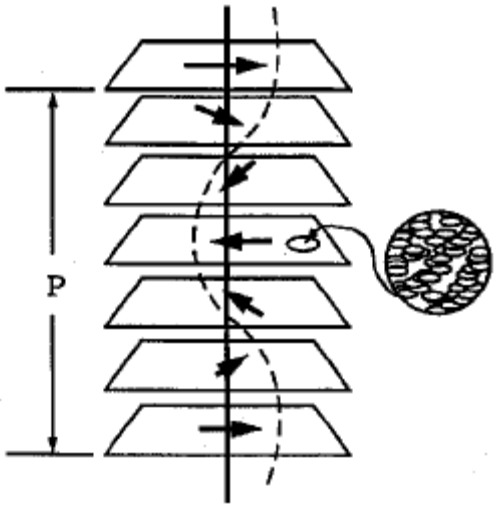

Fig. 1. Liquid crystals in optically active (chiral nematic) phase, Ref. 9.

One of the issues encountered with liquid crystal thermography is that the perceived color response is sensitive to the angle and the uniformity of illumination as well as to the viewing angle of the detector.[2,3,9] If not accounted for properly in the data

reduction, these perceived color variations can be misinterpreted as significant temperature changes, especially on models with highly curved surfaces.[9] One of the biggest issues for short duration wind tunnel testing, however, is the slow response time of the liquid crystal layer.[3,9,10] The response time has been determined experimentally to be on the order of a few milliseconds, which means the technique cannot be applied if the heating load is changing rapidly or if run times are very short (i.e. shock tunnels).[9] Another major drawback is that each chemical composition can only cover a relatively narrow temperature range, and there is a tradeoff between the temperature resolution and the span covered.[2] This means that if a test article is expected to experience a large range of temperatures during a test, it may not be possible to measure over the entire model surface or for the entire duration of the test, or the temperature resolution will have to be low.

Several examples of liquid crystal thermography use for heat-transfer measurements in hypersonic facilities are reported in Ref. 11. A number of simple geometries, such as compression corners and swept blunt fins, were tested in Mach 8 gun tunnel with typical flow duration of 25 ms and in Mach 5 blowdown tunnel with run times of up to 8 sec; qualitative as well as quantitative data were extracted during these tests using the liquid crystal thermography technique.

1.2.3. Thermographic Phosphors

A relative-intensity two-color phosphor thermography technique for hypersonic wind tunnel testing was developed at NASA LaRC in the late 1980's – early 1990's and is still in active use. The two types of phosphor crystals (one emitting in the red and one emitting in the green portions of electromagnetic spectrum) are mixed with ceramic

cement and applied to a test article, usually by spraying.[12] Final coating thicknesses are on the order of 25 μm. This application method provides robust coatings that can withstand multiple wind tunnel runs.[13] Typical thermographic phosphor formulations are insoluble and thus are suspended in an applicable ceramic binder. The result is a rough coating surface (as compared to temperature-sensitive paints) due to aggregation of phosphor molecules. This in turn results in grainy images at high spatial resolutions.[14]

The phosphor molecules in the coating are excited when illuminated by an ultraviolet (UV) light source. The excitation energy of the molecules is then dissipated by a number of non-radiative and radiative processes. One of the radiative processes is phosphorescence, which occurs when molecules relax from an excited triplet state to a ground energy state by emitting a photon. The intensity of the phosphorescence depends on the amount of incident UV illumination and the surface temperature. For a more detailed discussion of phosphorescence phenomenon refer to Section 1.2.5. The phosphorescent emission of the coating is detected by a video or a charge-coupled device (CCD) camera, which in part determines the spatial and temporal resolution of the resulting data. The ratio of the green to red emissions is found at each pixel to eliminate any emission intensity variations due to spatial non-uniformities in the illumination field.[10,12,13] Thus, only the temperature-dependent variations in the phosphorescent emission intensity remain.

The luminescent intensity of the phosphor molecules deceases as their temperature increases due to an increasing number of molecules taking thermal paths to de-excitation (i.e. thermal quenching). A direct relationship between the relative emission intensity and the phosphor temperature exists and is found via a calibration process. The

calibration can then be used to determine the temperature on a test article's surface. The usable temperature range is 22 – 170 °C and depends on the particular phosphor formulation.[13]

The surface heat flux is calculated from the surface temperature data using a simplified one-dimensional heat conduction model described in more detail in Section 1.3 and in Refs. 12 and 13. To obtain accurate heat-flux results using this model, the test articles need to be made out of a low thermal diffusivity material with uniform, isotropic thermal properties. Additionally, the test articles must be durable enough to withstand multiple wind tunnel tests in high-speed flows and exhibit minimal deformation when thermally cycled. To meet these requirements a rapid prototyping silica ceramic slip casting method was developed at NASA LaRC. The resulting fused silica test articles are robust enough for testing at NASA LaRC hypersonic facilities and exhibit thermally insulative properties necessary for the semi-infinite slab assumption in the heat-transfer data reduction model.[13] For this latter reason the thermographic phosphor technique has not been successfully applied to metal test articles.[2]

The thermographic phosphor technique was applied to the studies of the boundary-layer transition on the Shuttle Orbiter, the parametric full configuration X-33 phase 1 concepts, the full configuration heating on the X-33 phase 2, X-34, and X-38 configurations, to name a few.[13]

1.2.4. Temperature- and Pressure-Sensitive Paints

Temperature-sensitive paints (TSP), and their equivalent in pressure measurements, pressure-sensitive paints (PSP), have been developed based on the luminescence quenching mechanisms in the 1980's. These coatings are typically

comprised of a host material, usually a polymer, and luminescent molecules, which are dispersed within the host material, or binder. In general, the binder and the luminophores are dissolved in a solvent, which allows the coating to be applied with a brush or a spray. The polymer "cures" as the solvent evaporates and only a smooth hard coating remains on a surface.[15]

The overall TSP and PSP systems' operating principle is similar to that of the thermographic phosphor technique described in the previous section, but is based on a different luminescent process (i.e. fluorescence). The luminophores become excited when illuminated with a light of an appropriate wavelength (usually UV or blue), and the resulting fluorescence is red-shifted relative to the excitation wavelength. The luminescent emission from PSP decreases as the partial pressure of oxygen (air pressure) increases, i.e. PSP is able to sense pressure through oxygen sensitivity (oxygen quenching). For this reason the binders used in PSP formulations are oxygen-permeable. TSP, on the other hand, measures temperature by means of thermal quenching, i.e. as the surface temperature increases the luminescent intensity decreases since more excited luminophores take thermal paths to de-excitation.[15] This is analogous to the thermographic phosphors' operating principle described in the previous section.

The temperature-sensitive coating is usually applied over a base coat, which can be thick relative to the active layer if a metallic test article is used. This provides an insulating layer, which can simplify the data reduction in short-duration flows, e.g. shock tunnels, where the insulating layer is sufficient to prevent any heat conduction into the test article itself.[16,17] White pigment is often added to the base coat to create a diffuse

reflection of the excitation light through the paint layer and thus increase the paint emission intensity.[18]

In both TSP and PSP systems, the emitted light intensity is detected by a photodetector (e.g. a CCD camera) filtered at the emission wavelength. The detection device largely determines the resolution and the number of images that can be acquired during each run. For intensity-based measurements ratioing of run (wind-on) images by a reference (wind-off) image is required. This is done to eliminate spatial coating and illumination non-uniformities so that only the intensity changes associated with changes in pressure and/or temperature fields remain. Usually model displacement is observed between the wind-off and the wind-on conditions, so the images have to be mapped to a three-dimensional grid of the test article to ensure proper image alignment prior to the ratioing procedure. The ratioed intensity data are subsequently converted into temperature histories in the case of TSP and pressure histories in the case of PSP by applying pre-determined calibration curves or through an *in situ* calibration procedure. The temperature calibration for TSP is logarithmically linear with respect to the reference-to-run intensity ratio and can be written as $T = C + D\ln\left(\frac{I_{ref}}{I}\right)$, where T is the surface temperature, I is the run image intensity, I_{ref} is the reference image intensity, and C and D are the calibration coefficients.[16] The corresponding calibration for PSP can be expressed as $P = \frac{P_{ref}}{B}\left(\frac{I_{ref}}{I} - A\right)$, where P is the pressure at a run condition, P_{ref} is the pressure at a reference condition, and A and B are the calibration coefficients.[18] Note that pressure-sensitive luminophores are typically also temperature sensitive, so a correction has to be applied to PSP data if there is a temperature rise during a PSP test.

Temperature-sensitive luminophores also exhibit some oxygen sensitivity, but to a much lesser extent.[19] Oxygen-impermeable binders are used in TSP formulations to minimize the oxygen quenching effect.[14] With an appropriate data reduction algorithm the TSP temperature data can be converted into heat-transfer rates. This type of intensity-based TSP system was selected as the most suitable candidate for performing global heat-transfer measurements at Tunnel 9.

In addition to intensity-based TSP and PSP systems, so-called lifetime-based systems exist. Theoretically, a reference image is not required for lifetime TSP and PSP systems, which is their biggest advantage. The lifetime methods are based on the response of luminescence to a time-varying (i.e. pulsed or flashed) excitation light. The exponential decay of the excited state luminescence is utilized to determine a time constant, i.e. lifetime, which can then be used to determine pressure in the case of PSP systems or temperature in the case of TSP systems. More specifically, the lifetime constant is determined from the ratio of integrated energies of the fluorescent emission at two gates (i.e. camera exposures) acquired during the decay process, as illustrated in Fig. 2, where $t_o - t_1$ is the duration of the 1st gate and $t_2 - t_3$ is the duration of the second gate.[20] The time constant can then be found as $\tau = \frac{t_1 - t_0}{\ln(1 + m_1 / m_2)}$, where m_1 and m_2 are the integrals of the exponential decay functions over gates 1 and 2, respectively. The pressure is then found using the lifetime Stern-Volmer relation: $\tau_A / \tau = 1 + kP$, where τ_A and τ are the time-integrated decay time

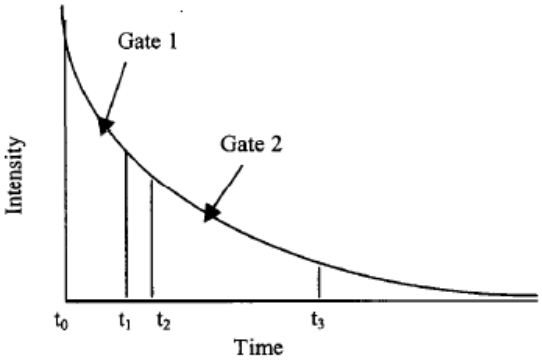

Fig. 2 Fluorescent lifetime measurement, Ref. 20.

constants in the absence and in the presence of quenching molecules (i.e. oxygen), respectively, P (torr) is the air pressure, and k (torr^{-1}) is a modified Stern-Volmer constant that converts the partial pressure of oxygen to the atmospheric pressure.[21] The same principles are applicable to the lifetime TSP measurements, although the majority of research to date has concentrated on the lifetime PSP technique.

In theory, the excited state lifetime measurements are independent of illumination, paint layer thickness, and luminophore concentration, which is why the reference wind-off image is not required in contrast to intensity-based systems. In practice, however, there is an issue with aggregation of luminophores as the paint cures, which results in perceptible point-to-point variation in lifetime constants on a surface with uniform pressure and temperature fields. This means that a wind-off reference image may once again be required for accurate quantitative measurements.[15,18] This issue in some cases negates the main advantage of lifetime-based systems as compared to intensity-based systems. A chapter on lifetime-based methods can be found in Ref. 15.

Examples of successful TSP implementation for heat-transfer measurements in high-speed flows include indented cone tests at the CUBRC LENS I short-duration hypersonic tunnel facilities[16], the three-dimensional shock/turbulent boundary layer interaction in an inlet flow tests at the Purdue University blowdown supersonic tunnel[10], and the tests of the surface interactions of reaction control system jets with the aft body of capsule reentry vehicle shapes in the NASA LaRC 31-inch Mach 10 tunnel[14], to name a few.

The TSP and the thermographic phosphor techniques both sense temperature through the process of luminescence, which is described in the next section. For a more in-depth discussion of photochemical processes, see Ref. 22.

1.2.5. Luminescent Processes

A photochemical reaction occurs when a molecule in its ground singlet state absorbs a photon of light and becomes electronically excited. Each excited state has distinct energy, lifetime, and structure. Excited molecules are chemically different from the same molecules in the ground singlet electronic state and are expected to behave differently.[22] Photon absorption and radiative and non-radiative de-excitation processes can be described by the Jablonski energy level diagram pictured in Fig. 3, where S_o is the ground singlet state, $S_1 - S_n$ are the excited singlet states, and $T_1 - T_n$ are the excited triplet states. The solid arrows represent radiative energy transfer processes (i.e. processes that involve photon absorption or emission), and the dashed arrows represent non-radiative energy transfer processes. Each electronic state (e.g. S_1, T_1) is split into several

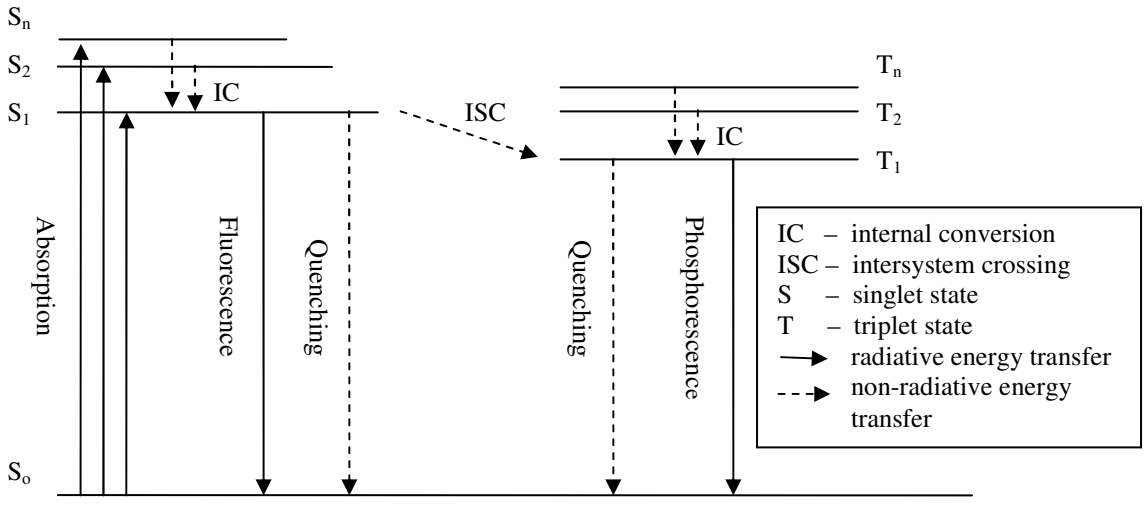

Fig. 3. Jablonski energy level diagram

vibrational levels, which in turn are split into a number of rotational levels (both vibrational and rotational levels are omitted from the diagram for ease of viewing).

The excitation energy of an excited molecule may be dissipated by a number of different competing processes. When a molecule becomes electronically excited by absorbing a photon, it typically is excited to one of the higher vibrational levels within the electronic state. However, it tends to relax to the lowest vibrational level of that state on ~ 10^{-14} sec timescale, which is short compared to other de-excitation processes.[23] Additionally, the excited molecules can transition between excited energy states. The internal conversion (IC) process is the radiationless transition between energy states of the same spin state (e.g. S_2 to S_1) and generally occurs on the same time scale as the vibrational relaxation process. The intersystem crossing (ISC) process is a radiationless transition between different spin states (e.g. S_1 to T_1) and occurs on a ~ 10^{-8} sec timescale.[22,23] Note that the intersystem crossing is the predominant process for molecules to populate the excited triplet states, as shown in Fig. 3 (i.e. population of triplet states from the ground singlet state by photon absorption is negligible).

There are two types of radiative processes (known as luminescence) that can occur: fluorescence, which is a spin-allowed radiative transition between two states of the same multiplicity (e.g. S_1 to S_o) and phosphorescence, which is a spin-forbidden radiative transition between two states of different multiplicity (e.g. T_1 to S_o). Statistically fluorescence is much more likely to occur than phosphorescence. This is because the phosphorescence process takes place on a much slower timescale, i.e. ~ 10^{-5} – 10 sec, as compared to fluorescence, which occurs on ~ 10^{-9} – 10^{-7} sec timescale.[23] This means that non-radiative paths to de-excitation (i.e. quenching, which is a non-radiative conversion

of electronic energy to heat) become more likely for a molecule in an excited triplet state as compared to a molecule in an excited singlet state, which also means that phosphorescence is less likely to occur than fluorenscence.[22] Note that intersystem crossing and fluorescence occur on a similar time scale, and thus are competing processes. Thermographic phosphors make use of the phosphorescence process, while TSP's make use of the fluorescence process. Both phosphorescence and fluorescence are less likely to occur with increasing temperature, i.e. the excited molecules are more likely to be thermally quenched. Thus, the inverse relationship between the temperature and the radiant intensity of these molecules allows using thermographic phosphors and TSP as temperature sensors, as was described in Sections 1.2.3 and 1.2.4, respectively.

1.3. Heat-Transfer Data Reduction Techniques for Global Measurement Systems in Hypersonic Facilities

A range of global temperature and heat-transfer acquisition techniques has been utilized at various hypersonic facilities. In all cases, reducing global temperature data into heat flux is a difficult task; therefore, simplifying assumptions related to specific test conditions usually have to be made to develop a practical data reduction methodology. In other words, the choice of simplifying assumptions that define the heat-flux data reduction algorithm depends on the facility and the types of models tested. This section covers several examples of the heat-transfer data reduction methodologies applied to coating-based global measurement systems at various hypersonic ground test facilities.

A two-color thermographic phosphor technique described in Section 1.2.3 has been successfully applied to ceramic wind tunnel models at NASA LaRC.[12,13] For this technique, the test articles at a uniform initial temperature are injected into the flow when the desired test conditions have been established in the test cell. This allows modeling the

heating load as a constant step input in the mathematical heat-transfer model used for data reduction. Thus, the two factors that greatly simplify the heat-transfer calculations are: 1) step input heating load due to model injection, and 2) semi-infinite wall assumption (i.e. no temperature rise on the back wall), which is valid for ceramic models of an appropriate thickness. Additionally, the phosphor coating is assumed to have a negligible thickness, the local radius of curvature of the surface is assumed to be large, and the heat is assumed to propagate normally through the model's surface, which implies that the heat conduction can be assumed one-dimensional (1D).[13] Applying these assumptions to the 1D heat conduction equation yields a simple solution, which only requires an initial temperature image and a run temperature image to calculate the heat transfer. In other words, the temperature time history is not required. An example of a global heat-transfer map obtained using this method on a model of X-38 is shown in Fig. 4.[24]

The heat-transfer data reduction methodology described by Roberts et al.[9] for a liquid crystal thermography technique applied in hypersonic flows with duration on the order of 1 sec involves matching of the thermal product $\sqrt{(\rho cK)}$ of the model material with that of the liquid crystals. This ensures a homogeneous thermal behavior of the test article so that a one-layer heat-transfer model can be applied. Additionally, a step heating load, constant heat flux, 1D heat conduction, and semi-infinite model wall are assumed just as in the previous method. As a result, a

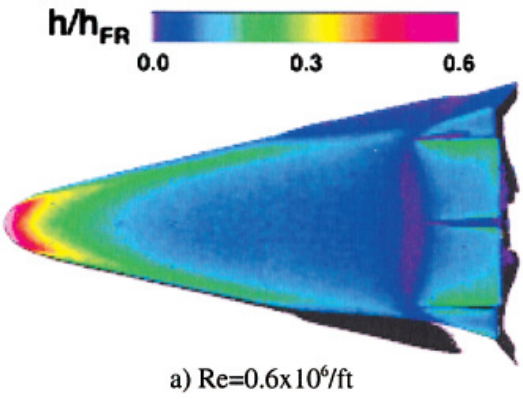

Fig. 4 Global heating on a subscale X-38 model for M_∞ = 10, α = 40 deg, and body flap deflection angle = 20 deg, Ref. 24.

straightforward analytical solution is possible. The step heating load assumption implies that this methodology can be applied to the data reduction either at shock-tunnels or if a test article is injected into the flow when the desired steady conditions are already reached. A quantitative global heat-flux estimate on a model of the BAE HOTOL aerospace plane obtained using liquid crystal thermography technique in the Light Piston, Isentropic Compression (LPIC) hypersonic wind tunnel is shown in Fig. 5.[25]

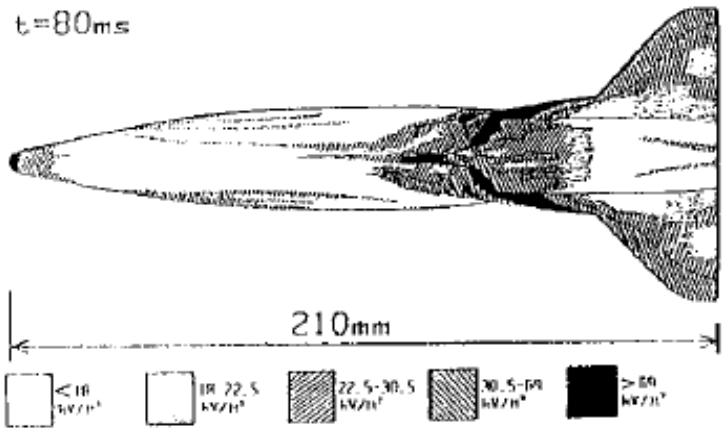

Fig. 5. Quantitative heat-flux estimation on undersurface of HOTOL model, Ref. 25.

An example of a luminescent paint technique successfully applied in a hypersonic ground-test facility includes the research at the JAXA Hypersonic Shock Tunnel facility by Nakakita et al.[26] The approach taken in this facility in order to simplify the heat-transfer data reduction is to utilize a very thin TSP layer so that the influence of the typically insulative coating on the surface temperature response can be neglected. Using typical polymer material properties, the authors estimated that the paint layer can be ignored in the data reduction if its thickness is less than 1 μm thick, and a 2-percent error in the heat-transfer rate calculation is acceptable. Then, an assumption of a uniform, semi-infinite media can be made in the heat-transfer rate calculation, making the data

reduction straightforward. Ohmi et al.[27] conducted a follow-up experimental study to evaluate this assumption. They tested ceramic models painted with a very thin TSP layer (0.2 to 3 μm) and used the same simple, 1D, semi-infinite heat conduction model to calculate the heat-transfer rate. They ignored the TSP layer in the data reduction and calculated the error associated with this simplification. They concluded that the paint layer can be ignored in the data reduction if it is less than 0.5 μm, and not 1 μm, as previously estimated by Nakakita et al. because of the differences between the actual TSP material properties and the handbook tabulated polymer material properties. Additionally, the error in calculated heat flux changed nonlinearly with the change in the paint layer thickness. An example of a heat transfer map obtained using this method on a compression corner in the JAXA 0.44-m Hypersonic Shock Tunnel is shown in Fig. 6, where the white dashed line indicates the location of the corner.[28]

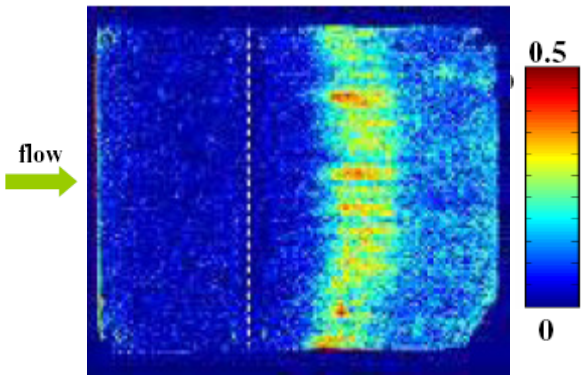

Fig. 6 Normalized heat flux image of compression corner flow at α = 0 deg, M_∞ = 10.4 at t = 15 ms, Ref. 28.

Hubner et al. used TSP to measure the full-field surface heat-transfer rates in short-duration hypersonic flow (run times under 10 ms) at the LENS1 shock tunnel at CUBRC on metal test articles.[16] A thick, insulating polyurethane layer (100 to 150 μm) was applied between the thin (approximately 5 to 10 μm) active TSP layer and the metal model surface. As was mentioned earlier, the thick insulating layer is used in short-duration flows to prevent the heat conduction into the test article's wall, thus simplifying the data reduction. The heat transfer was calculated assuming an adiabatic wall condition

(i.e. zero heat transfer), constant step input heating load, and temperature-independent thermal conductivity, K, and thermal diffusivity, α of the TSP formulation. These assumptions are applicable only because of the short run time of the facility. An example of a heat-transfer map obtained using this technique in LENS1 shock tunnel on a sharp-nose indented cone model is shown in Fig. 7.[16]

Fluorescent paint use for heat-transfer measurements on a waverider model was reported in 1995 at AEDC Hypervelocity Wind Tunnel No. 9, which is a hypersonic blowdown wind tunnel described in detail in Section 1.4. In this experiment the aluminum model's windward surface was covered with an insulative white Mylar film (0.1-mm thick), over which the temperature-sensitive coating was applied (~10 μm thick). The heat flux was calculated using the Fourier's law of conduction discretized over the insulating layer as follows: $\dot{q}_s(t) = K(T_s(t) - T_b)/L$, where $\dot{q}_s(t)$ is the surface heat flux, K is the thermal conductivity of the Mylar film, $T_s(t)$ is the surface temperature measured by the fluorescent coating, T_b is the temperature at the interface between the insulating layer and the metal base, which is assumed to be equal to the model's initial temperature, and L is the thickness of the insulating layer. This model assumes linear temperature gradient through the insulating layer, ignores the fluorescent paint layer in the thermal modeling, and assumes the base temperature T_b is constant for the duration of

Fig. 7 Heat transfer for the sharp-nose indented cone model in at M_∞ = 9.6, Re = .27×10^6/m flow. Color scale range: violet = 0 W/cm^2 to red = 100 W/cm^2, Ref. 16.

a run (i.e. short run times). The knowledge of the thermal conductivity of Mylar is also required. One of the heat-transfer maps obtained during this test is shown in Fig. 8.

Taking into consideration the uncertainties in measured quantities (i.e. T_s and T_b), variations in the reported K values for Mylar (± 20%), and the deviation of T_b from the initially measured value, the overall uncertainty in the calculated heat transfer was estimated to be ± 21% for an aluminum model and ± 25% for a steel model.[29] In addition to the large uncertainty in the reported K value for Mylar, problems may be encountered in trying to apply the film to complex-shaped models. Additionally, the constant T_b assumption breaks down for long run times and/or high heating rates.

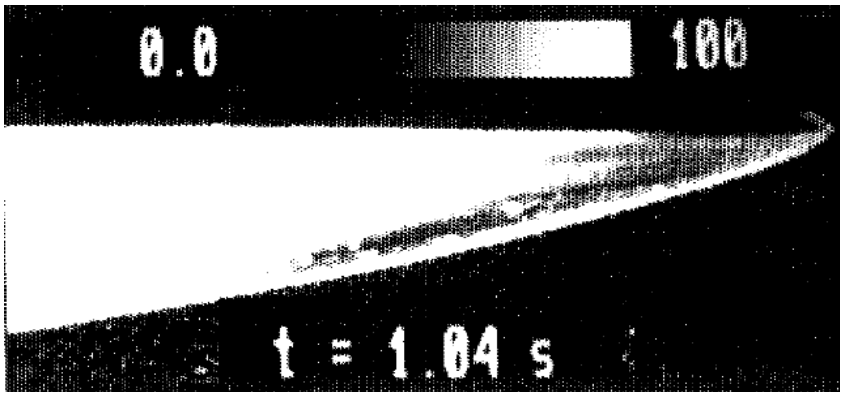

Fig. 8 Heat-transfer map of waverider bottom at t = 1.04 sec during a M_∞ = 9.7, Re = 2×10^6/ft run. The gray intensity bar units are kW/m^2, Ref. 29.

A new effort has been underway at Tunnel 9 aimed at developing a global TSP heat-transfer measurement system that does not require an insulative layer, but instead the heat conduction into the metal test article is dealt with through the use of an appropriate data reduction algorithm. The system also employs the improved illumination and photodetection technologies, data processing systems, and paint formulations available today. This development effort is the subject of the remainder of the present work.

The next two sections present a Tunnel 9 description and highlight some of the unique challenges associated with implementing a global heat-transfer measurement system in the facility, and in particular with developing a suitable data reduction algorithm.

1.4. Tunnel 9 Facility Description

Tunnel 9 is a unique blowdown facility that utilizes pure nitrogen as the working fluid and currently operates at Mach numbers of 7, 8, 10, and 14. An operational envelope showing Reynolds number equivalent altitudes vs. Mach number for Tunnel 9 operating conditions is presented in Fig. 9. The unit Reynolds number range for the facility is from 0.05×10^6/ft (useful for high-altitude/viscous interaction simulation) to 48×10^6/ft (duplication of flight dynamic pressure). Tunnel 9 nominal test conditions are summarized in Table 1. The "good flow" period refers to the time interval during each run when the desired test conditions are reached and are maintained for the duration of the interval.

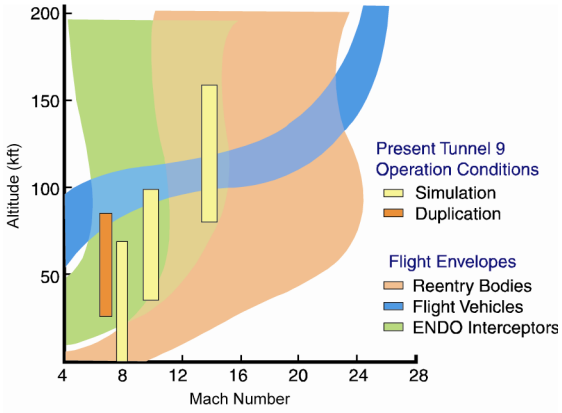

Fig. 9. Hypervelocity Wind Tunnel 9 operational envelope.

The test section is over 12 ft long and has a diameter of 5 ft, enabling testing of large-scale model configurations that can include simultaneous force and moment, pressure, and heat-transfer instrumentation. The test cell features a model support system that is capable of dynamically pitching large test articles through an angle-of-attack sweep from -5 to +45 deg at rates of up to 60 deg/s during a typical run. The Mach 10 and 14 nozzles are 40 ft in length with a 60-in.-diam exit. The Mach 8 nozzle is 40 ft in

length with a 35-in.-diam exit and operates as a free jet when it is mated to the 60-in.-diam test cell. A photo of the Tunnel 9 Mach 10 nozzle and test cell is provided in Fig. 10, and a schematic of the entire facility is shown in Fig. 11. Note that the flow direction is from left to right in these figures.

Fig. 10. AEDC White Oak Hypervelocity Wind Tunnel No. 9 Test Cell and Mach 10 Nozzle.

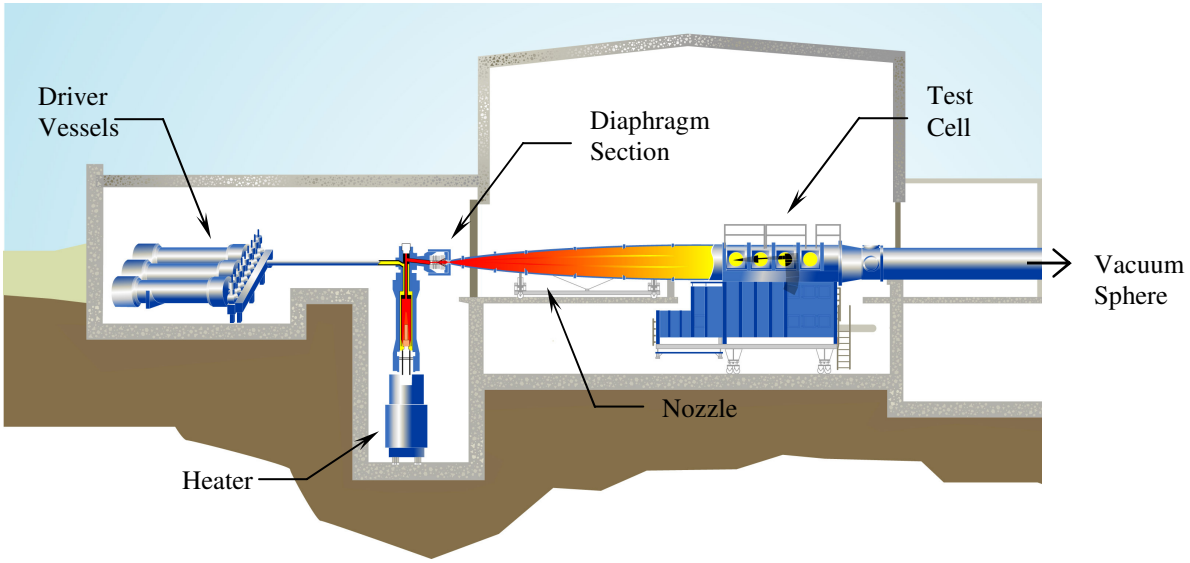

Fig. 11. Tunnel 9 facility schematic.

Table 1. Tunnel 9 Nominal Test Conditions

Mach 7 Nozzle/AeroThermal Leg (11.5" exit freejet to a 60" test cell)

Re/ft (E6)	P_0 (psia)	T_0 (degF)	Pitot (psia)	M_{inf}	P_{inf} (psia)	T_{inf} (degR)	U_{inf} (ft/sec)	Good Flow Period (sec)
4.080	2821	2800	45.605	6.68	7.880E-01	363.60	6353	-
7.56	5521	2894	88.115	6.73	1.499E+00	373.40	6486	-

Mach 8 Nozzle (34.84" exit freejet to a 60" test cell)

Re/ft (E6)	P_0 (psia)	T_0 (degF)	Pitot (psia)	M_{inf}	P_{inf} (psia)	T_{inf} (degR)	U_{inf} (ft/sec)	Good Flow Period (sec)
4.09	1030	1123	12.34	7.41	0.174	136.0	4308	0.50 - 1.90
8.06	2087	1152	25.10	7.44	0.349	138.3	4365	0.45 - 0.95
17.5	5007	1216	56.71	7.66	0.746	139.2	4503	0.30 - 0.80
23.4	6466	1200	74.96	7.68	0.980	138.1	4498	0.30 - 0.71
31.6	8518	1158	95.70	7.84	1.20	131.2	4472	0.30 - 0.55
47.9	12548	1150	145.1	7.96	1.77	129.8	4516	0.20 - 0.42

Mach 10 Nozzle (60" nozzle exit and test cell)

Re/ft (E6)	P_0 (psia)	T_0 (degF)	Pitot (psia)	M_{inf}	P_{inf} (psia)	T_{inf} (degR)	U_{inf} (ft/sec)	Good Flow Period (sec)
0.57	314	1210	1.220	9.44	1.059E-02	91.19	4498	1.50 - 6.50
1.16	730	1310	2.630	9.61	2.200E-02	94.20	4649	1.00 - 4.00
2.03	1334	1353	4.840	9.61	4.057E-02	97.13	4721	1.21 - 2.01
4.00	2640	1322	8.952	9.82	7.182E-02	91.91	4695	0.40 - 1.10
4.78	3405	1397	11.389	9.87	9.049E-02	95.59	4812	0.40 - 1.30
5.41	3515	1290	11.715	9.91	9.229E-02	89.21	4667	2.00 - 2.55
7.67	4875	1264	16.104	10.01	1.244E-01	86.77	4648	1.90 - 2.40
9.24	6502	1382	21.659	10.03	1.668E-01	93.50	4834	0.25 - 0.80
11.78	7878	1779	27.302	10.16	1.941E-01	88.66	4768	1.20 - 1.60
14.35	10086	1369	32.946	10.24	2.432E-01	90.85	4866	0.25 - 0.50
16.76	11875	1796	42.228	10.51	2.553E-01	85.84	4852	0.70 - 0.90
20.00	14000	1350	51.510	10.20	3.834E-01	92.60	4890	-

Mach 14 Nozzle (60" nozzle exit and test cell)

Re/ft (E6)	P_0 (psia)	T_0 (degF)	Pitot (psia)	M_{inf}	P_{inf} (psia)	T_{inf} (degR)	U_{inf} (ft/sec)	Good Flow Period (sec)
0.054	115	1764	0.106	12.65	5.150E-04	70.97	5315	15.00 - 25.00
0.070	168	1882	0.148	12.76	7.050E-04	73.92	5471	12.00 - 22.00
0.11	262	1997	0.262	12.79	1.240E-03	77.66	5619	4.00 - 12.00
0.24	881	2313	0.636	13.21	2.827E-03	83.55	6020	4.00 - 9.00
0.50	2117	2545	1.505	13.22	6.675E-03	91.58	6305.9	1.00 - 3.50
1.26	5936	2668	3.928	13.51	1.670E-02	92.90	6494	1.25 - 2.40
2.13	11402	2864	7.330	13.70	3.030E-02	98.32	6773	0.80 - 1.45
3.56	19311	2811	11.661	14.16	4.511E-02	92.84	6803.85	0.65 - 1.40

During a typical run, the vertical heater vessel (left side of Fig. 11) is used to pressurize and heat a fixed volume of nitrogen to a predetermined pressure and temperature defined by the desired freestream conditions. The test cell and the vacuum sphere are evacuated to approximately 1 mmHg and are separated from the heater by a pair of metal diaphragms located upstream of the throat. When the desired temperature and pressure are reached in the heater, the diaphragms are ruptured. The gas then flows from the top of the heater vessel, expanding through the contoured nozzle into the test section at the desired freestream test conditions. As the hot gas exhausts from the top of the heater, cold nitrogen gas from the pressurized driver vessels enters the heater base. This cold gas drives the hot gas out of the top of the heater in a piston-like fashion, thereby maintaining constant conditions in the nozzle supply plenum and in the test section during the run. A run is completed once the supply of hot, pressurized gas is exhausted. A more complete description of the Tunnel 9 facility and its capabilities can be found in Ref. 30.

1.5. Challenges Associated with Implementing a TSP System at Tunnel 9

As discussed in Section 1.3, the choice of the global heat-transfer measurement technique and the data reduction algorithm implemented at each test facility depends on the nature of the facility itself. Some of the primary challenges associated with developing a high-productivity TSP system for the use at Tunnel 9 can be summarized as follows: high dynamic and thermal loading environment (i.e., large freestream Reynolds numbers), long run times relative to other hypersonic facilities of similar freestream conditions, non-negligible tunnel startup time, and ramp-like startup heating profiles. The two latter conditions are important since the test articles are not injected into the flow and

are subjected to heating during the startup portion of a run, which complicates the data reduction as will be explained in a later section. Some of these challenges are illustrated in Fig. 12, where the startup and the "good flow" periods are marked on the plot of the total pressure versus time for a static $M_\infty = 10$, $Re = 5\times10^6$/ft run. The startup time for this condition is on the order of 0.2 sec and the useful flow period is on the order of 1 sec, which is considered long for a hypersonic wind tunnel. Additionally, the harsh environment of the facility necessitates the use of robust stainless steel models for force and moment testing. It is desired to use the same test articles for TSP measurements as for force and moment tests to reduce the cost and complexity of a test program to a customer wanting to collect several types of data at Tunnel 9. The temperature-sensitive coating must also be robust enough to survive the tunnel test conditions. Finally, it is desired to have the capability to perform the global heat-transfer measurements while dynamically pitching the model during a run, which imposes additional requirements on all of the components of the TSP system. The present work deals with the development of such a global heat-transfer measurement system, and in particular with the development of a suitable data reduction algorithm. The next section outlines the objectives and provides a brief summary of the present work.

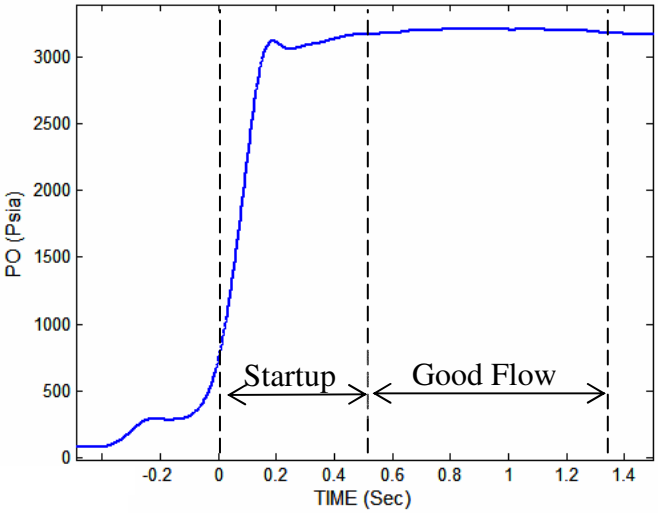

Fig. 12. Total pressure versus time for a static $M_\infty = 10$, $Re = 5\times10^6$/ft run.

1.6. Research Objectives and Thesis Overview

The goal of the present work is to develop an intensity-based TSP global quantitative heat-transfer measurement system based on the previous research and successful proof of principle tests conducted at Tunnel 9. The effort includes the development of the data processing as well as of the data reduction techniques that will enable high-resolution quantitative heat-transfer measurements on steel models in long-duration hypersonic flows in Tunnel 9.

After taking into consideration some of the facility-related challenges described in the previous section along with several other practical data reduction considerations presented later in the work, three data reduction approaches were developed to reduce the TSP emission intensity/temperature data into heat transfer. Each of these data reduction algorithms is based on a common basic approach, but each is applicable to a different situation based on the unknowns in the system. These data reduction approaches are described in detail along with their uses and limitations. The underlying simplifying assumptions of each approach are also discussed. One of the main assumptions made in all three data reduction algorithms is analyzed using the finite-element modeling software. The sensitivity of the basic heat-transfer data reduction algorithm to the perturbations in the thermophysical properties and the thickness of the temperature-sensitive coating layer was also evaluated using finite-element modeling.

Finally, the TSP emission intensity data were acquired on a model of a NASA CEV capsule during a five-run TSP test to evaluate the system's ability to acquire multiple high-resolution images during a single run and to validate the proposed data processing and reduction approaches. Qualitative as well as quantitative results from the

test are presented and compared to the baseline heat-transfer data obtained with the conventional instrumentation (i.e. thermocouples). An estimate of the thermal conductivity of the temperature-sensitive coating layer as a function of temperature is made using the TSP and the thermocouple data from one of the runs. Future improvements to the TSP system and the data reduction algorithms aimed at improving the quality of the acquired data and expanding the capabilities of the system are also discussed. The next chapter provides a description of the TSP system development effort at Tunnel 9.

Chapter 2. TSP System Development at Tunnel 9

2.1. Previous Work and Current State of the Art

TSP systems have been successfully applied to the study of flows from low subsonic to hypersonic speeds over a wide range of Reynolds numbers and under a variety of test conditions, e.g., cryogenic and high-temperature (high-enthalpy) conditions. However, as was mentioned earlier, each facility is unique and presents its own unique challenges for successful implementation of these systems to quantitative heat-transfer measurements. Recent advancements in CCD camera and illumination technologies have prompted an effort to create a high-quality quantitative intensity-based TSP global heat-transfer measurement system at Tunnel 9.[31]

The development was undertaken jointly by AEDC White Oak, LeaTech LLC, and the University of Maryland. These efforts resulted in an intensity-based TSP system capable of withstanding the harsh environment of the facility and acquiring high-resolution temperature maps of complex, three-dimensional surfaces. Previously, two successful feasibility studies were conducted at Mach 10 and 14 over a wide range of Reynolds numbers on a wedge with a protruding fin model. A number of potential illumination and photodetection systems were also evaluated. From these studies the need for improvements in detection and illumination systems necessary to make quantitative measurements was identified. A study was conducted to assess various possible illumination sources for their intensity, stability, and operational qualities, which led to the selection of an optimal illumination source for the next stage of the TSP system development. Additionally, the survivability of the temperature-sensitive coating was demonstrated. This system and experimental results from its use have been reported in

Ref. 31. In that previous study, however, the temperature maps were acquired at frame rates that were too slow to extract quantitative heat-transfer data. Nevertheless, the images are valuable in that they provide a very high level of qualitative information about the model's surface flow patterns. An example of a temperature map obtained during one of the runs of the feasibility study is shown in Fig. 13.

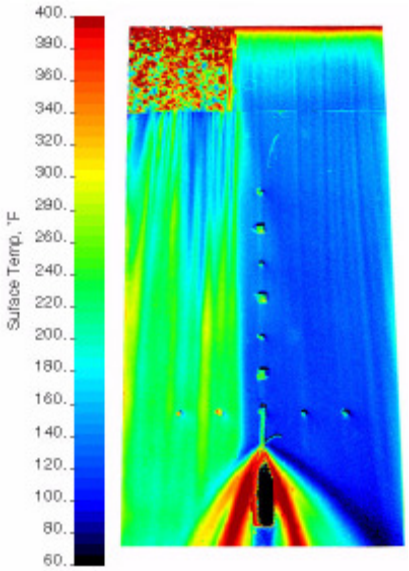

Fig. 13. Static wedge TSP image: M_∞ = 14, *Re* = 1.3×10^6/ft, Ref. 31.

Based on the studies described above, a TSP system capable of high-resolution qualitative as well as quantitative measurements was developed and tested on a model of NASA's Crew Exploration Vehicle in 2006. Similar to the TSP systems used in other ground test facilities, the system developed for the use in Tunnel 9 consists essentially of four main components: an illumination system, a detection system, the temperature-sensitive coating, and the data-processing algorithms. A brief description of each system component is presented below.

Photon Technologies 200W mercury-xenon arc lamps were chosen as the optimal illumination source based on their superior stability, intensity, and operational qualities assessed in the study described in Ref. 31. The lights are filtered with UG-1 bandpass filters centered at 355 nm (with ~53 nm FWHM) to match the excitation wavelength of the TSP formulation used at Tunnel 9. The lamps are operated continuously, i.e., not flashed.

PI/Acton PhotonMax 512B cameras were chosen as the photodetection devices to enable acquisition of continuous, high-quality images required for quantitative heat-

transfer measurements in a transient facility such as Tunnel 9. Per the manufacturer's description, the 512Bs are low-noise CCD cameras with on-chip multiplication gain via electron multiplication CCD (EMCCD), which multiplies photoelectrons by an impact ionization process prior to readout.[32] The 512Bs feature a 512×512 pixel CCD array and a 16 bit A/D converter. The camera CCD chips are back-illuminated and have quantum efficiency of over 90% at the emission wavelength of the TSP formulation used at Tunnel 9. Quantum efficiency is defined as the percentage of photons hitting the photoreactive surface of a photodetector that will excite a photoelectron, i.e. the efficiency of photon conversion to electric charge. The quantum efficiency curve for the 512Bs is shown in Fig. 14. The cameras are equipped with the broadband bandpass filters centered at 600 nm (with ~80 nm FWHM) to match the emission wavelength of the TSP formulation. Each of the CCD cameras is connected to a computer, which stores all of the acquired images in its memory. Once the cameras are triggered, the images are acquired continuously at a frame rate determined by the region of interest, spatial resolution, and the exposure time set by the user.

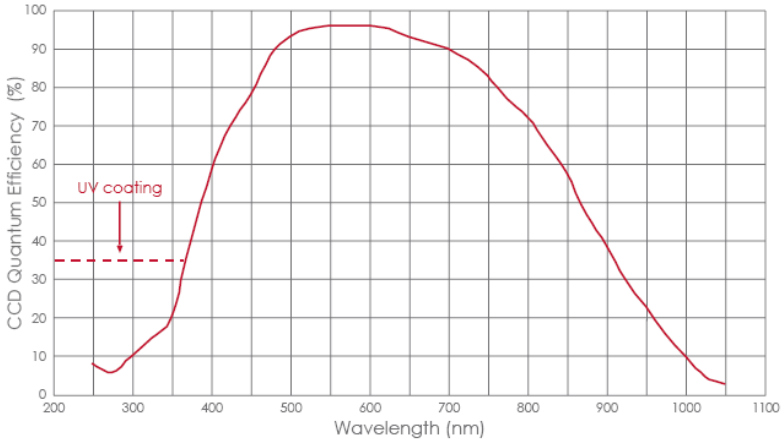

Fig. 14. CCD quantum efficiency versus wavelength for PI/Acton PhotonMax 512B cameras, Ref. 32.

The temperature-sensitive coating used at Tunnel 9 was developed by LeaTech LLC. The TSP formulation utilizes a Europium complex as the temperature-sensitive luminophore. This paint formulation has a broad absorption spectrum (relative to Europium alone) with excitation centered at 365 nm. The formulation's emission is centered at 614 nm.[31] Utilization of Europium gives this formulation temperature sensitivity on the order of tenths of a degree Fahrenheit. The luminophore is combined with a high-temperature polyurethane binder resulting in a paint formulation that can withstand temperatures up to 360°F. Also, there is no uncertainty associated with the paint acting as a pressure sensor via oxygen quenching since the tunnel uses nitrogen as the working fluid.

Application of the TSP to the test articles used in Tunnel 9 is done by airbrushing a white basecoat followed by a temperature-sensing layer onto the metal model's surface. The white basecoat is used to enable diffuse reflection of the excitation light through the paint layer and thus increase the paint emission intensity. It is important to note that the basecoat is not used to create an insulating layer, as is done in TSP systems used with metallic wind tunnel models in other facilities.[16,17] As was mentioned earlier, the Tunnel 9 run times are relatively long for a hypersonic facility, and so the insulating layer would have to be impractically thick to prevent any heat conduction into the test article's base. Thus, an approach was developed to deal with the heat conduction effects by means of the data reduction algorithms, which are the subject of the next section.

The basic data acquisition and processing steps are summarized as follows. The reference (wind-off) and the run (wind-on) images are acquired using PI/Acton's Winview32 software. The reference and the run raw image data are imported into

Greenboot image-processing software[33] as TIF images and are subsequently mapped to a 3D grid with the help of the registration marks on the surface of a test article. The run images are then ratioed by a reference image to correct for non-temperature related intensity variations, and can subsequently be converted to engineering units if a calibration is available. The surface temperature or ratioed intensity data are output globally from Greenboot and are subsequently analyzed using Matlab. The methodologies developed to reduce the data into heat transfer are discussed in the next section.

2.2. Data Reduction Methodologies

2.2.1. Basic Approach

The current approach for evaluating the heat transfer from the global surface temperature measurements in Tunnel 9 follows a somewhat different path from that of most other hypersonic facilities. This is partly because of the operational behavior of the wind tunnel and the need to use the structurally robust stainless steel models that are well suited for force and moment testing in the high Reynolds number environment, as was discussed in Section 1.5. The goal is to be able to use the same test articles for TSP tests as are used for force and moment testing in order to reduce the complexity and the cost resulting from multiple models for a single test program.

Additional factors that differ from other hypersonic facilities and influence the data reduction algorithm include tunnel startup time, which is on the order of 200 ms (see Fig. 12). The heating profiles during the startup are ramp-like since models are located in the flow (not injected) while the facility is started. This means that a step change in heat-transfer rate cannot necessarily be assumed, as in the cases of short-duration hypersonic

facilities[16] or model injection into the flow.[12] Furthermore, it is desired to acquire the TSP data while dynamically pitching models during a single run. As a result, since the heating input to a model for this application is a function of the angle of attack, it is also a function of time.

Other factors that must be accounted for in the data reduction include the highly non-linear temperature-dependent thermophysical properties (i.e. K and α) of the paint formulation over the range of temperatures encountered in Tunnel 9. In other words, K and α of the coating cannot be assumed constant in the data reduction. This means that either the thermophysical properties need to be accurately measured over the appropriate temperature range or a data reduction technique that does not require the knowledge of the thermophysical properties must be devised. Furthermore, the temperature-sensitive coating is an insulator with the thermal conductivity several orders of magnitude lower than that of steel. The paint layer applied to Tunnel 9 models is approximately 2 mil (~ 51 μm) thick. This thickness, which is larger than that used by most facilities, is desired in order to increase the paint's emission so that good signal-to-noise ratios can be obtained even for short exposure times. It is currently considered too thick to be ignored in the heat-transfer modeling, and thus must be accounted for in the data reduction (i.e. two-layer heat conduction model may be required).[26,27]

In general, the algorithm used to calculate the heat flux from the TSP data at Tunnel 9 is based on the same analysis that is applied to reducing the coaxial thermocouple temperature data into heat transfer and is driven by the transient nature of the facility. In essence, to calculate the heat transfer from the coaxial thermocouple data at Tunnel 9 a time history of the surface temperature is applied as a boundary condition in

a transient, 1D, heat-transfer conduction model. This model employs a second-order, Euler-explicit, finite-difference approximation method to solve the transient 1D heat equation. The method allows obtaining a 1D temperature distribution at nodes at varying depths through a steel model wall of finite thickness at each time step of the algorithm. The local convective heat-transfer rate is calculated based on Fourier's law using a second-order approximation of the temperature profile at the model's surface.

At the beginning of the run (initial condition), the model is assumed to be at a uniform initial temperature. Zero heat transfer at the back wall inside the model is the remaining boundary condition required to solve the heat equation numerically. The latter assumption has been validated for the thick-walled models (0.375 in.) that are typically tested at Tunnel 9. The explicit finite-difference scheme is subject to a convergence criteria expressed by [Eq. (1)], where α is the thermal diffusivity of the wall material, Δt is the time step, and Δx is the differential element size. In the final data reduction step, the calculated convective heat-flux data are usually non-dimensionalized by the run conditions and the local wall temperature and presented as the Stanton number defined as $St = \frac{\dot{q}}{\rho u (H_o - C_p T_w)}$, where ρ and u are the freestream density and velocity, H_o is the calculated total enthalpy, C_p is the specific heat of nitrogen at constant pressure, and T_w is the measured wall temperature. The calculated heat-flux uncertainty from the coaxial thermocouple data using this approach is quoted ±6 percent for fully laminar or fully turbulent regions. A detailed description of the coaxial thermocouple data reduction methods used at Tunnel 9 can be found in Ref. 34.

$$Fo = \frac{\alpha \Delta t}{\Delta x^2} \leq \frac{1}{2}$$

$$\alpha = \frac{K}{\rho C_p} \tag{1}$$

To develop an analogous data reduction methodology for evaluating the heat transfer using the TSP data, a second layer comprising the temperature-sensitive coating was added to the 1D heat-transfer model described above. In reality, the temperature-sensitive coating consists of two layers: the base coat and the active layer. However, the two layers can be treated as one in the data reduction algorithm since they are made of the same host matrix material and are assumed to have the same thermophysical properties.

The two-layer numerical model is represented schematically in Fig. 15, where $\dot{q}$ is the heating rate, L is the paint layer thickness, Δx is the differential element size through the model wall, T_1 is the surface temperature, T_2 – T_n are the temperatures through the model wall at node locations, and K, ρ, and C_p with subscripts 1 and 2 are the material properties of the TSP formulation and steel, respectively. In this case the TSP data provide the input boundary condition (T_1) at the surface of the model. Then, the heat-flux balance at the interface between the two materials (the TSP and the model wall material) is enforced using the Fourier's law of conduction, and the interface temperature T_2 is calculated. After finding the interface temperature, the algorithm proceeds in exactly the same way as described above for coaxial thermocouples. One additional assumption is made to simplify the algorithm: the temperature gradient through the paint layer is assumed to be linear. This assumption eliminates the need for dividing the very thin TSP layer into differential elements and solving for the internal temperature distribution as is

done for the metal model wall, thus eliminating the need for knowledge of the overall thermal diffusivity of the temperature-sensitive coating. However, the thermal conductivity of the coating is still required.

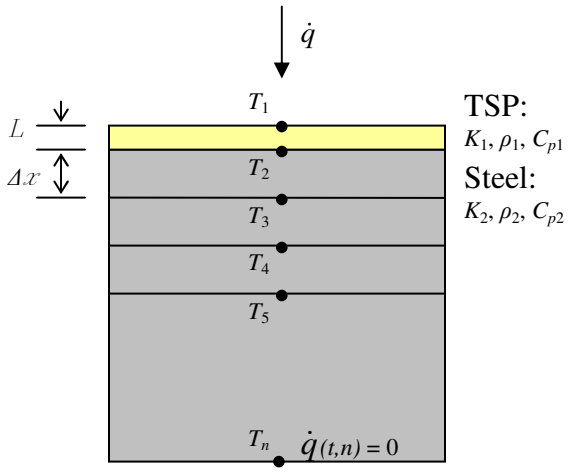

Fig. 15. Schematic representation of the numerical model.

The data reduction approach described above for both the coaxial thermocouple data and the TSP data relies on the 1D heat conduction assumption. The assumption is very common when calculating the heat transfer from surface temperature data and is employed by all of the coating-based global heat transfer measurement systems described in Section 1.3. The 1D heat conduction assumption applies as long as the model's surface can be assumed locally flat (i.e. the radius of curvature is large), the surface spatial heat-flux gradients are moderate, and the model wall is thick and uniform enough that for the duration of a run there are no lateral heat-conduction effects. If a model's surface is not locally flat, but instead can be better represented by a spherical or a cylindrical surface element, the 1D heat conduction equation can still be applied, but should be solved in spherical or cylindrical coordinates, respectively.[34] The majority of the models tested at Tunnel 9 are manufactured with a 0.375-in.-thick wall. This wall thickness was shown

more than sufficient for 1D heat conduction assumption to hold for most conditions test articles are subjected to at Tunnel 9.

The validity of the linear temperature gradient through the paint layer assumption is addressed in Section 2.3. The next three sections describe the three methodologies developed for reducing the TSP data into heat transfer including the advantages and the limitations of each.

2.2.2. 1st Methodology

The first data reduction algorithm developed to reduce the TSP data into heat-transfer rates assumes that the surface temperature histories are known from the calibrated TSP data. Additionally, the algorithm requires that the coating layer thickness L and the thermal conductivity K as a function of temperature are known. Then, the Fourier's law of conduction [Eq. (2)] can be discretized as shown in [Eq. (3)] to produce a very simple expression for enforcing the heat-flux balance at the interface of the two layers (see Fig. 15). The heat-flux balance is used to find the interface temperature T_2.

$$\dot{q} = -K(\partial T/\partial x) \tag{2}$$

$$K_1 \cdot \frac{T_1 - T_2}{L} = K_2 \cdot \frac{T_2 - T_3}{\Delta x} \tag{3}$$

Subsequently, the temperature history at nodes through the metal model wall and the local heat transfer at the surface are found using the same numerical method as that described above for coaxial thermocouples. More specifically, the one-dimensional, transient heat equation [Eq. (4)] is solved for nodal temperatures numerically using the second-order, Euler-explicit, finite-difference approximation [Eq. (5)]. Once the temperature distribution through the model wall is known, Fourier's law of conduction [Eq. (6)] is applied at the surface of the model to calculate the convective heat transfer

using the second-order approximation of the temperature profile at the model's surface [Eq. (7)].

$$\partial T/\partial t = \alpha(\partial^2 T/\partial x^2) \tag{4}$$

$$\frac{T_{i+1,j} - T_{i,j}}{\Delta t} = \alpha_2 \left(\frac{T_{i,j+1} - 2T_{i,j} + T_{i,j-1}}{\Delta x^2} \right) \tag{5}$$

$$\dot{q} = -K(\partial T/\partial x)_{\text{surf}} \tag{6}$$

$$\dot{q} = \frac{-K_1}{L} \left[-3T_{i+1,1} + 4\left\{ \frac{1}{2}\left(T_{i+1,1} + T_{i+1,2}\right) \right\} - T_{i+1,2} \right] \tag{7}$$

Note that [Eq. (4)] and [Eq. (5)], which can be equivalently rewritten as [Eq. (8)], are the 1D heat conduction equations expressed in Cartesian coordinates. They are only applicable to the locally flat geometries, as described in the previous section. For surfaces that are better represented by cylindrical elements, the 1D heat conduction equation and its second-order, Euler-explicit, finite-difference representation are expressed as [Eq. (9)] and [Eq. (10)], respectively.

$$T_{i+1,j} = F_o(T_{i,j+1} - T_{i,j-1}) + T_{i,j} + 2F_o(T_{i,j-1} - T_{i,j}) \tag{8}$$

$$\frac{1}{r}\frac{\partial}{\partial r}\left(Kr\frac{\partial T}{\partial r} \right) = \rho C_p \frac{\partial T}{\partial t} \tag{9}$$

$$T_{i+1,j} = \left(1 + \frac{\Delta r}{2r} \right) F_o(T_{i,j+1} - T_{i,j-1}) + T_{i,j} + 2F_o(T_{i,j-1} - T_{i,j}) \tag{10}$$

Similarly, [Eq. (11)] and [Eq. (12)] can be used to solve the 1D heat conduction problems for geometries best described in spherical coordinates.

$$\frac{1}{r^2}\frac{\partial}{\partial r}\left(Kr^2\frac{\partial T}{\partial r} \right) = \rho C_p \frac{\partial T}{\partial t} \tag{11}$$

$$T_{i+1,j} = \left(1 + \frac{\Delta r}{r} \right) F_o(T_{i,j+1} - T_{i,j-1}) + T_{i,j} + 2F_o(T_{i,j-1} - T_{i,j}) \tag{12}$$

Note that the only difference between [Eq. (8)], [Eq. (10)], and [Eq. (12)] is the coefficient multiplying the first right-hand term in each of the equations. In the cylindrical and spherical coordinates this coefficient incorporates the local radius of curvature of the finite-difference elements. The coefficient can be used to determine if the influence of the surface curvature is great enough to warrant the use of cylindrical or spherical coordinates for the data reduction. In other words, if $\Delta r/2r$ in [Eq. (10)] or $\Delta r/r$ in [Eq. (12)] is << 1, then the surface curvature is negligible. In this manner, the heat transfer can be calculated from the calibrated TSP data at each pixel on the surface of a test article assuming the thickness and the thermal conductivity of the paint layer are known with sufficient accuracy.

2.2.3. 2nd Methodology

Unfortunately, accurate determination of the coating's temperature-dependent thermophysical properties is a difficult task. Therefore, a method was developed to estimate the thermal conductivity, K, of the coating as a function of temperature using the TSP and the thermocouple data. It is assumed that there is a pair of standard thermocouples installed on the model's surface symmetrically (i.e. they experience the same heating load), and the entire model's surface is coated with the temperature-sensitive coating except for one of the thermocouples. A pair of these symmetrically located thermocouples can be modeled as is graphically represented in Fig. 16, where T_1^{tsp} is the TSP temperature data over the painted thermocouple; T_2^{tsp} is the painted thermocouple data; T_1^{st} is the unpainted thermocouple data; T_2^{st} is the temperature calculated using the 1D heat conduction finite-difference model; $K_1(T)$ is the thermal conductivity of TSP; $K_2(T)$ is the thermal conductivity of the model material (stainless

steel); *St* (Stanton number) is the nondimensionalized heat input; Δx is the differential element size through the model wall, and *L* is the paint layer thickness. The Stanton number was assumed to be equal at the two symmetrically located points on the model that correspond to the painted and unpainted thermocouples ([Eq. (13)]). A linear temperature profile through the paint layer was assumed once again, thus allowing the use of the discretized Fourier's law of conduction at the surface [Eq. (14)] in the same way as in the 1st methodology described in the previous section [Eqs. (15) and (16)].

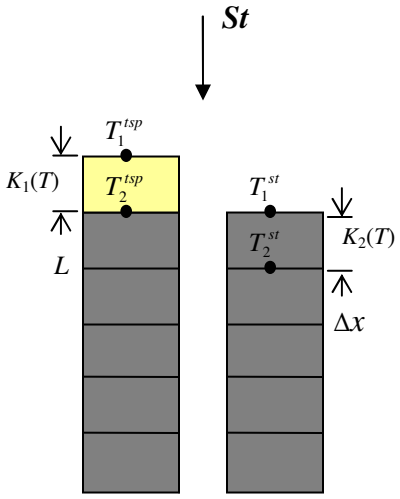

Fig. 16. Graphical representation of two symmetrically located thermocouples. One is painted with TSP, and the other is unpainted.

$$St_1 = St_2 \tag{13}$$

$$\dot{q} = -K\,(dT/dx)_{\text{surf}} \tag{14}$$

$$\dot{q}_{tsp} = K_1 \frac{T_1^{tsp} - T_2^{tsp}}{L} \tag{15}$$

$$\dot{q}_{st} = K_2 \frac{T_1^{st} - T_2^{st}}{\Delta x} \tag{16}$$

From the Stanton number definition:

$$St = \frac{\dot{q}}{\rho u\left(H_o - C_p T_w\right)} \text{ and Eq. (13)}$$

$$\frac{\dot{q}_{st}}{\rho u\left(H_o - C_p T_1^{st}\right)} = \frac{\dot{q}_{tsp}}{\rho u\left(H_o - C_p T_1^{tsp}\right)} \tag{17}$$

Substituting [Eqs. (15) and (16)] into [Eq. (17)] and solving for K_1 yields [Eq. (18)], where K_1 is the only unknown:

$$K_1 = K_2 \frac{L}{\Delta x}\left[\frac{T_1^{st} - T_2^{st}}{T_1^{tsp} - T_2^{tsp}}\right]\left[\frac{H_o - C_p T_1^{tsp}}{H_o - C_p T_1^{st}}\right] \tag{18}$$

Once the estimate of $K(T)$ of the coating is available, the 1st methodology can be applied as before to convert the TSP temperature data into heat transfer. The thermal conductivity estimate obtained using this method is presented in Section 4.1.

2.2.4. 3rd Methodology

The 3rd data reduction approach developed for the TSP data reduction once again exploits the assumption of the linear temperature gradient through the paint layer to further simplify the data analysis. This method requires that several thermocouples (~ 6 to 8) are installed on the surface of a test article at locations that are deemed to be representative of the range of temperatures that the model is expected to experience during the test, such as areas with large temperature gradients. Subsequently, the entire model is coated with the TSP, including all of the thermocouples. The paint emission intensity during a wind tunnel run can then be anchored directly to the painted thermocouple temperature readings at the thermocouple locations to create a calibration. The calibration, which relates the TSP emission intensity to the temperature under the paint layer, can be applied to the entire model to create global temperature maps. These global temperature maps can subsequently be used as boundary conditions in a one-layer heat-transfer data reduction algorithm identical to the one used for coaxial thermocouple data reduction to obtain the global convective heat-transfer maps at any desired point in time (assuming 1D heat conduction assumption holds). The justification for this data reduction scheme is as follows.

Starting with the linear temperature gradient through the temperature-sensitive coating layer assumption and expressing the heat-transfer balance at the interface of the two layers as is done in [Eq. (3)] repeated below, the terms can be rearranged to solve for the thermal conductivity of the coating, K_1 (shown in [Eq. (19)]).

$$K_1 \cdot \frac{T_1 - T_2}{L} = K_2 \cdot \frac{T_2 - T_3}{\Delta x} \tag{3}$$

$$K_1 = K_2 \cdot \frac{L}{\Delta x} \cdot \frac{T_2 - T_3}{T_1 - T_2} \tag{19}$$

Substituting [Eq. (19)] into [Eq. (7)] repeated below without the time index subscripts and simplifying the common terms yields the expression in [Eq. (20)].

$$\dot{q} = \frac{-K_1}{L}\left[-3T_1 + 4\left\{\frac{1}{2}(T_1 + T_2)\right\} - T_2\right] \tag{7}$$

$$\dot{q} = \frac{K_2}{\Delta x}(T_2 - T_3) \tag{20}$$

[Eq. (20)], which is simply the first-order approximation of the heat flux at the interface between the two layers, implies that whenever the temperature gradient through the paint layer is linear, the terms related to the TSP temperature and properties drop out, and the surface heat transfer can be calculated directly from the painted thermocouple data as if there were no paint layer. As was mentioned earlier, this method requires a few thermocouples installed on the surface of the model underneath the paint. These thermocouples are used to create a calibration relating the ratioed paint emission intensity to the temperature under the paint layer for the range of temperatures encountered during a test. In this manner, the paint emission intensity histories over the entire surface can be converted into temperatures, which can subsequently be used as inputs into a one-layer

heat-transfer data reduction algorithm identical to the one used for thermocouple data reduction. The advantage of this approach is that no knowledge of the properties of the paint, the coating thickness, or even of the temperature on the surface of the test article (i.e. calibration) is required. Additionally, already established one-layer data reduction code can be used for the heat-flux calculations. Note that all three data reduction methodologies presented above rely on the linear temperature gradient through the paint layer assumption. The next section examines this assumption for models coated with TSP layers of various thicknesses for different magnitude heating loads to better define the applicability of the data reduction methods presented in this chapter.

2.3. Validation of the Linear ∇T through the Paint Layer Assumption

One of the underlying assumptions made in all of the data reduction methods presented in this chapter is that the temperature gradient through the temperature-sensitive coating layer is linear at least during the "good flow" period of each run. This assumption greatly simplifies the data reduction routines; however, its validity under various conditions should be carefully examined. The assumption was evaluated using a 1D two-layer model created using ANSYS, which is a powerful, commercially available finite-element modeling tool for structural and thermal analysis.

The ANSYS simulation was designed to closely represent a typical Tunnel 9 test article in 1D: 0.375–in.-thick stainless steel model wall (broken up into 200 elements) coated with a TSP layer. Three different TSP layer thicknesses were tested to cover the useful range identified for Tunnel 9 TSP tests. Namely, coating thicknesses of 1 mil (6 elements), 2 mil (12 elements), and 3 mil (18 elements) were evaluated. A schematic illustration of the ANSYS model with a 1-mil-thick TSP layer is shown in Fig.17, where

$T_1 - T_{207}$ represent the nodal temperatures through the model wall. The thermophysical properties of steel are well documented. The properties for 15-5 stainless steel typically used to manufacture Tunnel 9 test articles were input into the ANSYS model. The exact properties of the TSP coating are not yet known, so an estimate of $K(T)$ made using the method described in Section 2.2.3 along with the C_p and ρ values reported by Paul et al.[35] for a similar coating were used in the ANSYS model. The $K(T)$ estimate used in the ANSYS model is presented and discussed in more detail in Section 4.1. The heating loads were modeled as a linear ramp from 0 to 0.1 sec followed by a constant heat flux until the end of a simulation to represent a finite tunnel startup time followed by a "good flow" period (see Fig. 12). Four heating loads ranging from 5 to 20 Btu/ft^2 s were tested. A 0.001-sec time step was used to ensure the convergence of the finite-element model. All of the simulations were 2 sec long, which is a representative run time for Tunnel 9.

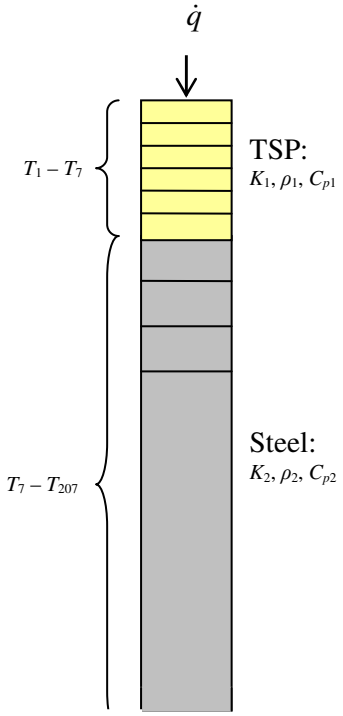

Fig.17. Graphical representation of the 1D two-layer ANSYS model with 1-mil-thick TSP layer.

Fig. 18 depicts the resulting temperature gradient through the paint layer for a 15 Btu/ft^2 s load applied to a model coated with a 2-mil-thick TSP layer. The location corresponding to x = 0 in. represents the interface between the steel model wall and the temperature-sensitive coating, and x = 0.002 in. represents the surface of the coating exposed to the heating load. The curves in the plot are the temperature profiles through

the paint layer at different times during the simulation. From this plot it is evident that the temperature gradient thorough the TSP layer starts out non-linear and approaches linear later in the simulation for the particular set of conditions (i.e. heating load and coating thickness). It was observed that the duration and the extent of non-linear behavior varied depending on the simulation conditions.

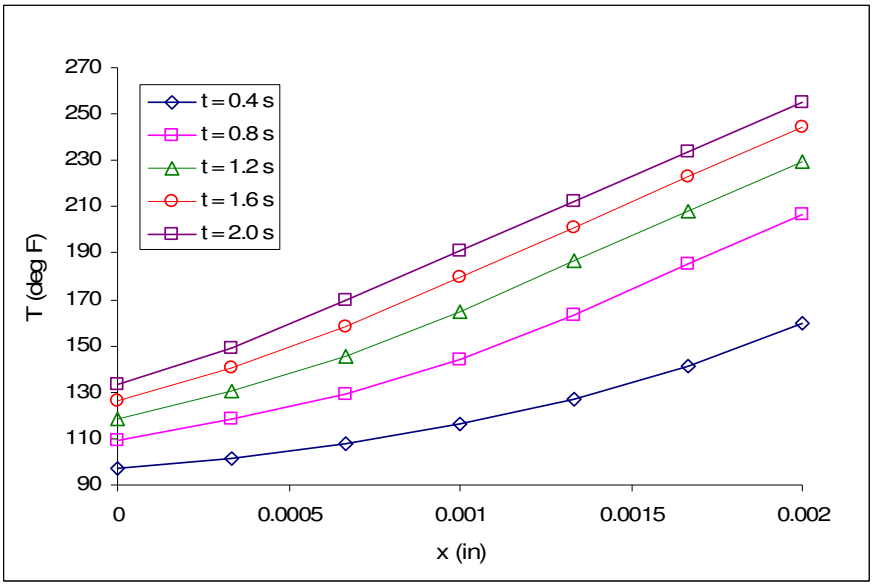

Fig. 18. Simulated temperature gradient through the paint layer at different instances in time for a 15 Btu/ft^{2}s heating load applied to the model coated with 2-mil-thick TSP layer.

To quantify this behavior, each of the temperature gradient curves (similar to the ones plotted in Fig. 18) at each instant in time for all of the conditions tested was fitted with a straight line. The resulting squares of the correlation coefficients (R^2) of the linear fits were plotted versus time and are presented in Fig. 19, Fig. 20, Fig. 21, and Fig. 22, which correspond to the 5 Btu/ft^2 s, 10 Btu/ft^2 s, 15 Btu/ft^2 s, and 20 Btu/ft^2 s heating load cases, respectively. Each figure contains 3 curves, one for each coating thickness tested (i.e. 1, 2, and 3 mil). From these plots it appears that there is a finite lag time, which depends on the heating load and the coating thickness, necessary for the heat to penetrate

the insulative paint layer and for the linear temperature gradient to be established. As expected, the cases where the coating is the thinnest (1 mil) or the heating loads are the largest are the most favorable, i.e. the linear temperature gradient is established faster.

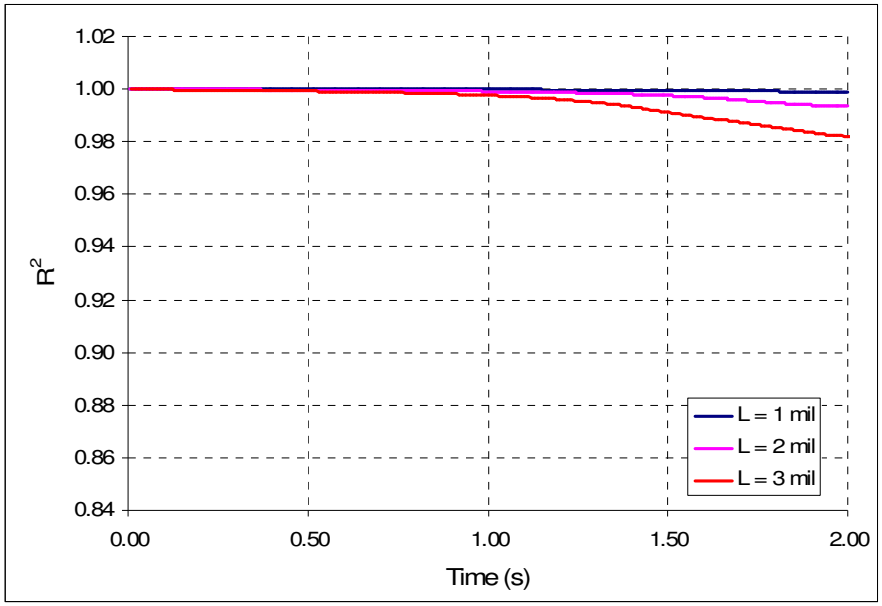

Fig. 19. R^2 of a linear fit of the temperature at nodes within the TSP layer for 5 Btu/ft^2 s heating load for three TSP layer thicknesses.

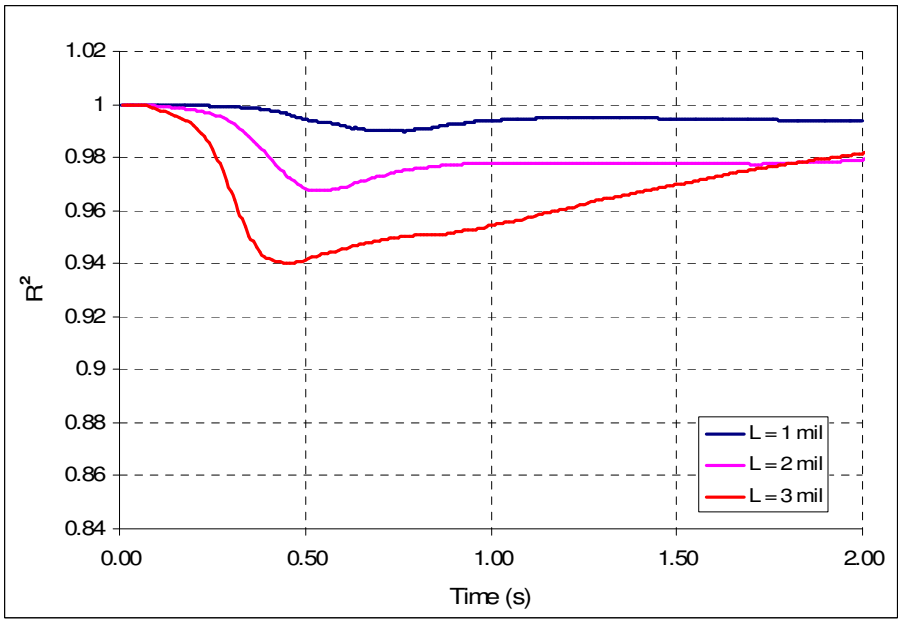

Fig. 20. R^2 of a linear fit of the temperature at nodes within the TSP layer for 10 Btu/ft^2 s heating load for three TSP layer thicknesses.

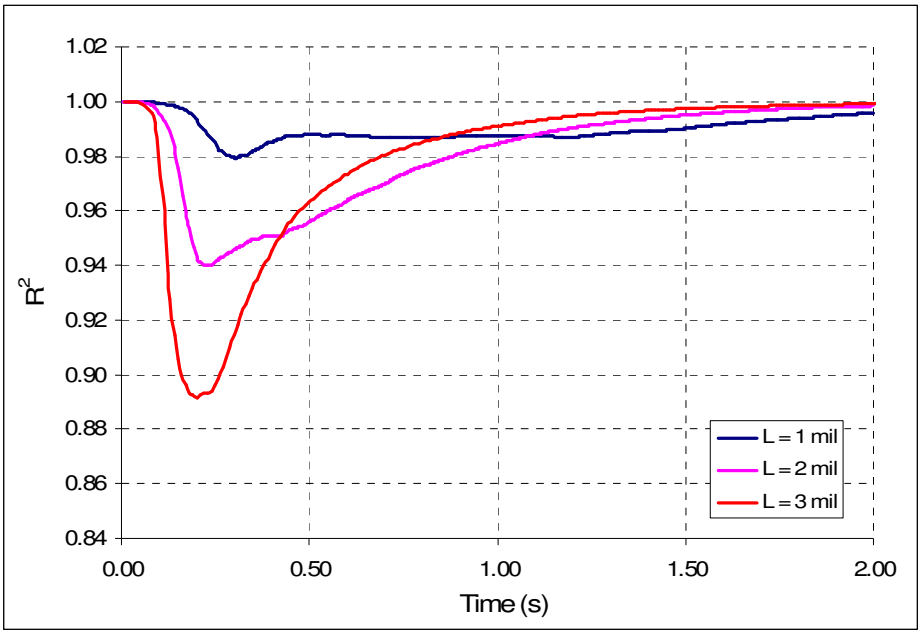

Fig. 21. R^2 of a linear fit of the temperature at nodes within the TSP layer for 15 Btu/ft^2 s heating load for three TSP layer thicknesses.

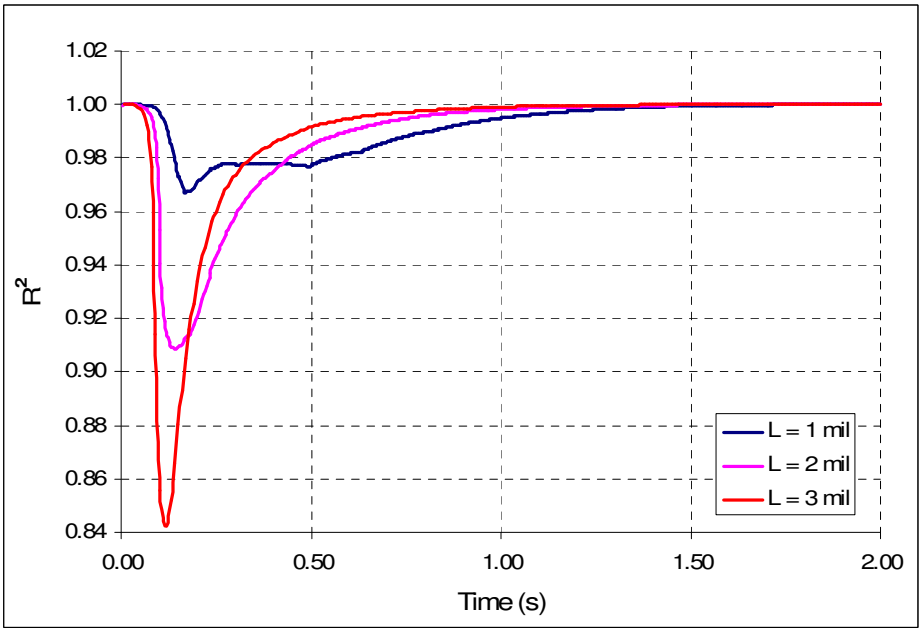

Fig. 22. R^2 of a linear fit of the temperature at nodes within the TSP layer for 20 Btu/ft^2 s heating load for three TSP layer thicknesses.

Another numerical study was conducted using the ANSYS model depicted in Fig.17 to simulate the data reduction procedure described in Section 2.2.4 (i.e. the 3rd

methodology) for the cases illustrated in Fig. 20, Fig. 21, and Fig. 22. The purpose of the study was to establish a relationship between the deviation of R^2 values from unity (i.e. not perfectly linear temperature gradient) and the resulting error in calculated heat flux due to the $R^2 = 1$ assumption in the data reduction algorithm. This was done by taking the temperature time-history at the interface of the temperature-sensitive coating and the metal model wall for each of the cases illustrated in Fig. 20 – Fig. 22 and applying it as a boundary condition to the same model with coating removed (i.e. bare metal model). The surface heat flux resulting from the uncoated model simulation was then compared to the nominal heat flux (i.e. heat flux used to generate the temperature histories). In effect, this procedure simulates the heat-flux calculation algorithm proposed in Section 2.2.4, where the temperature data under the paint layer obtained through a calibration are used to calculate the heat transfer as if there is no paint layer. The errors associated with the linear temperature gradient through the paint layer assumption for the cases presented in Fig. 20, Fig. 21, and Fig. 22 are shown in Fig. 23, Fig. 24, and Fig. 25, respectively.

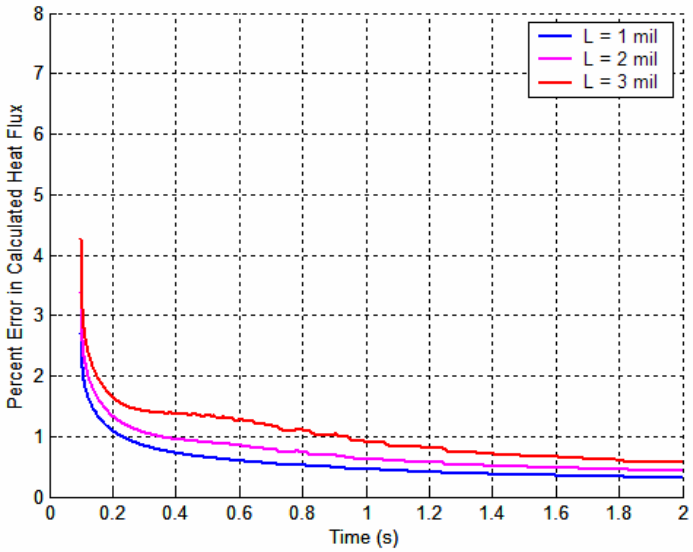

Fig. 23. Error in calculated heat flux due to linear temperature gradient through the TSP layer assumption for the 10 Btu/ft^2 s heating load for three TSP layer thicknesses, *L*.

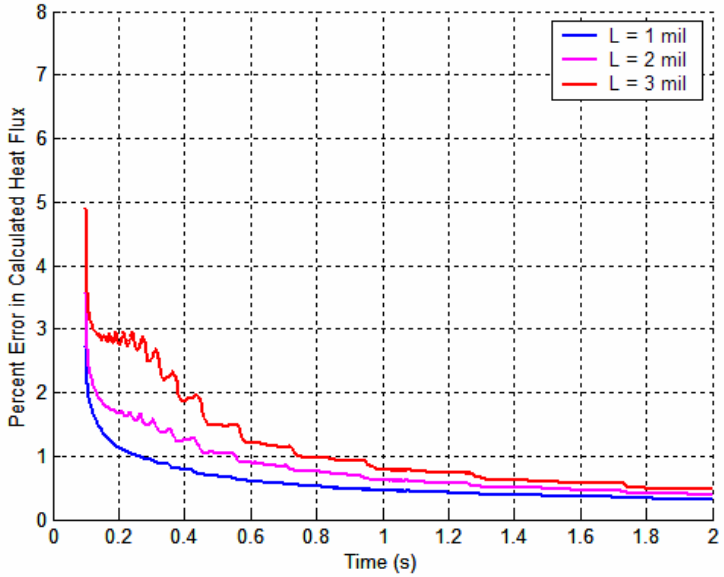

Fig. 24. Error in calculated heat flux due to linear temperature gradient through the TSP layer assumption for the 15 Btu/ft^2 s heating load for three TSP layer thicknesses, *L*.

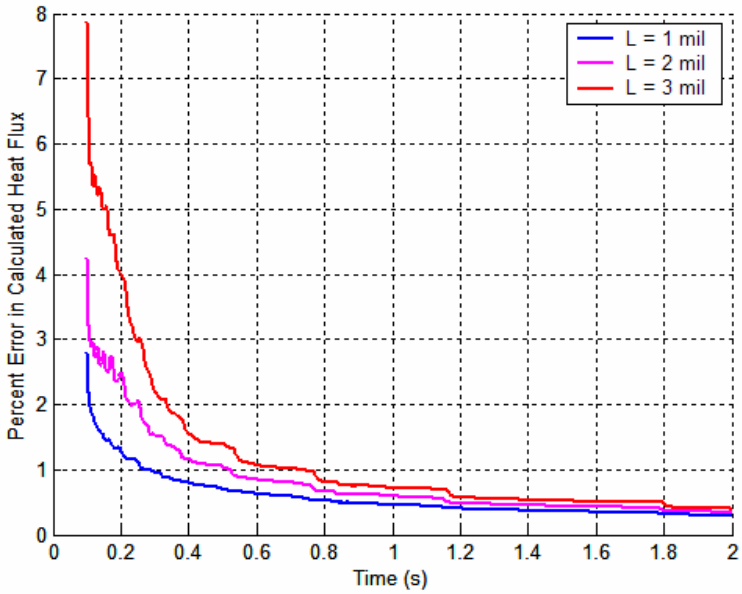

Fig. 25. Error in calculated heat flux due to linear temperature gradient through the TSP layer assumption for the 20 Btu/ft^2 s heating load for three TSP layer thicknesses, *L*.

Note that only the error in calculated heat flux during the "good flow" period is of interest here. For the test conditions available at Tunnel 9, the earliest time of the "good flow" start is at 0.2 sec for M_∞ = 8, Re = 47.9×10^6/ft condition (see Table 1), in which

case the error in calculated heat flux for the thickest coating and the largest load tested in the study (i.e. L = 3 mil, $\dot{q}$ = 20 Btu/ft^2 s) would be 4%. For majority of the test conditions listed in Table 1, however, the error during the "good flow" period due to the deviation of the temperature gradient from linear would be on the order of just 1%.

It is important to keep in mind that the observed temperature gradient behavior is a strong function of the estimated TSP properties used by the ANSYS model. In fact, if a constant thermal conductivity value is used in the simulation, the temperature gradient through the coating layer is essentially always linear after a short lag time regardless of other simulation conditions. However, the thermal conductivity of the coating is believed to be a non-linear function of temperature, as will be demonstrated in Section 4.1. Thus the trends illustrated in Fig. 19 – Fig. 25 are valid and should be considered in the TSP test planning in the context of expected run times and heating loads if the data reduction algorithms proposed in this chapter are to be utilized for the heat-transfer calculations.

Chapter 3. NASA CEV TSP Test

3.1. Test Description & Objectives

Recently, extensive aerothermodynamic testing of a model of the NASA CEV capsule was conducted at Tunnel 9. The model was instrumented with coaxial gages to measure surface temperature and heat transfer and to provide an indication of the boundary-layer-transition location. Following the completion of that test program, a temperature-sensitive coating was applied to the test article and a five-run TSP test program was conducted. The main objectives of the program were to implement the system improvements that resulted from the feasibility and trade studies briefly outlined in Section 2.1 and detailed in Ref. 31., obtain high-resolution qualitative as well as quantitative global measurements, and validate the proposed data reduction methodologies outlined in Section 2.2.

3.2. Experimental Setup

The test article was a 7–in.-diam model of the generic representation of the current NASA CEV capsule constructed out of 15-5 stainless steel. The geometry is similar to that of the Apollo capsules flown in the 1960s. During the Tunnel 9 tests, the pitch angle was fixed at 28 deg for all of the TSP runs. The test article coated with the TSP and illuminated with a UV light source is shown in Fig. 26. The physical setup of the model, the TSP system, and the test cell is sketched in Fig. 27.

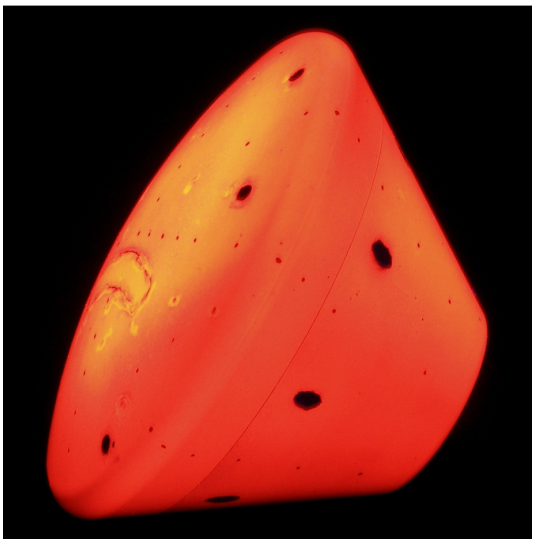

Fig. 26. CEV capsule coated with TSP and illuminated with UV light.

Three illumination sources were located on top of the test cell, and there were two on the side to ensure the entire model surface was illuminated as evenly as possible, with sufficient radiant intensity to provide 0.75-to-0.80-percent full-well potential, or maximum light capacity, of the CCD cameras. Both of the CCD cameras were initially mounted on top of the test cell to provide images of the heat shield (CAM1) and the aft body (CAM2). Later in the program one camera was relocated to the side of the test cell in an attempt to map the flow over the side of the aft cone. Note that only the heat shield data from two of the five runs are considered in the present work.

To protect the paint from potential photodegradation by the ultraviolet illumination, the light from each lamp was blocked during the periods in which the model did not need to be illuminated. The lamps were water cooled, and the output of each one was monitored by a photodiode to ensure stable output for the duration of each run. The room lights were turned off for each run to reduce the noise in the acquired data.

The run conditions and the camera settings for all 5 runs of the test program are summarized in Table 2. A variety of camera settings were tested to increase the frame rate, which results in decreased spatial resolution. For example, with the full 512×512 CCD array, the effective maximum frame rate for the 512B (including the exposure time and the readout rate) was 25 fps, which resulted in the spatial resolution of about 0.014 in/pixel. 2×2 pixel binning resulted in 42 fps frame rate and the spatial resolution of about 0.027 in/pixel. Binning of areas larger than 4×4 pixels, which corresponded to the resolution of about 0.056 in/pixel, was not attempted since further decrease in spatial resolution was undesirable.

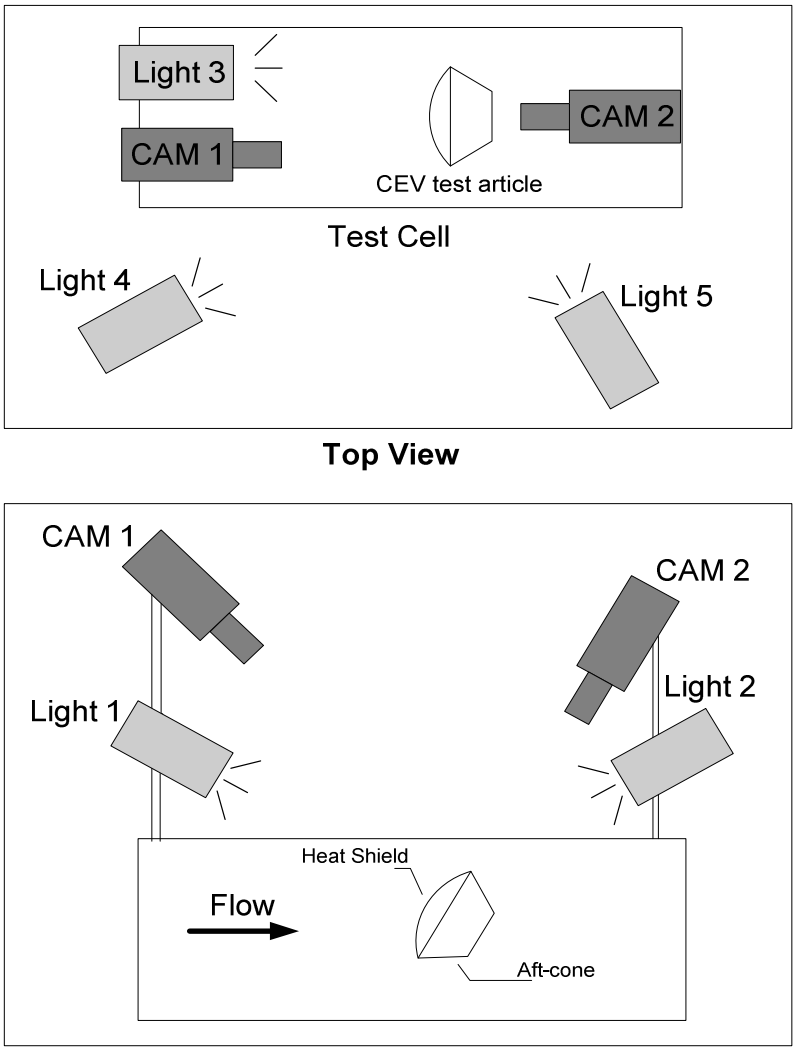

Fig. 27. Schematic of lights and cameras for NASA CEV test in Tunnel 9.

The required frame rate for the heat-transfer calculations will vary depending on the test conditions, i.e. high heating rates and/or pitching runs will require data sampled at a higher rate than low heating load static runs. The thermocouple data at Tunnel 9 is acquired at 500 Hz, which ensures a small enough time step Δt for the data reduction scheme to satisfy the convergence criteria with a reasonably-sized wall element Δx (see [Eq. (1)]). The effective sample rate, however, is much lower since the data is low-pass

filtered at 30 Hz. A numerical study conducted to assess the required sample rate for heat-transfer calculations at Tunnel 9 is described in Section 3.5.

Table 2. Run Matrix

Run	M_∞	***Unit Re, 10^6/ft***	***Nominal Good Flow (s)***	***Binning of the CCD Array***		***Frame Rate, fps***		***Exposure Time (ms)***
				Heat Shield (CAM 1)	Aft Cone (CAM 2)	Heat Shield (CAM 1)	Aft Cone (CAM 2)	
1	10	5.00	0.4 – 1.3	4 × 4	4 × 4	61	61	1.9
2	10	10.00	0.25 – 0.8	2 × 2	1 ×1	42	25	1.9
3	10	5.00	0.4 – 1.3	2 × 2	2 × 2	42	42	1.9
4	10	10.00	0.25 – 0.8	2 × 2	2 × 2	42	42	1.9
5	10	5.00	0.4 – 1.3	2 × 2	2 × 2	42	42	1.9

The paint was applied to both the heat shield and the aft body of the test article over the majority of the coaxial thermocouples that were included in it to measure the heat transfer at discrete locations during the non-TSP runs of the test program. A few thermocouples were left unpainted on the heat shield for comparison with symmetrically located painted thermocouples and to make it possible to estimate the $K(T)$ of the TSP formulation as described in Section 2.2.3. The locations of the painted and unpainted thermocouples are indicated in Fig. 28. The red dashed circles were added to the left side of the picture to indicate the locations of the painted thermocouples. The black solid dots on the surface of the paint are the registration marks used to align and map the images in the image-processing software. The thermocouple layout on the heat shield of the test article is shown in Fig. 29. Due to the physical damage to the coating as a result of small particles impacting the model and denting the paint on the surface, the coating had to be reapplied after the fourth run. The damage occurred as a result of the combination of severe test conditions (i.e. $Re = 10\times10^6$/ft) and a blunt model shape. For less severe test

conditions and/or less blunt body shape (e.g. wedge, as described in Ref. 31) no significant damage to the coating was observed.

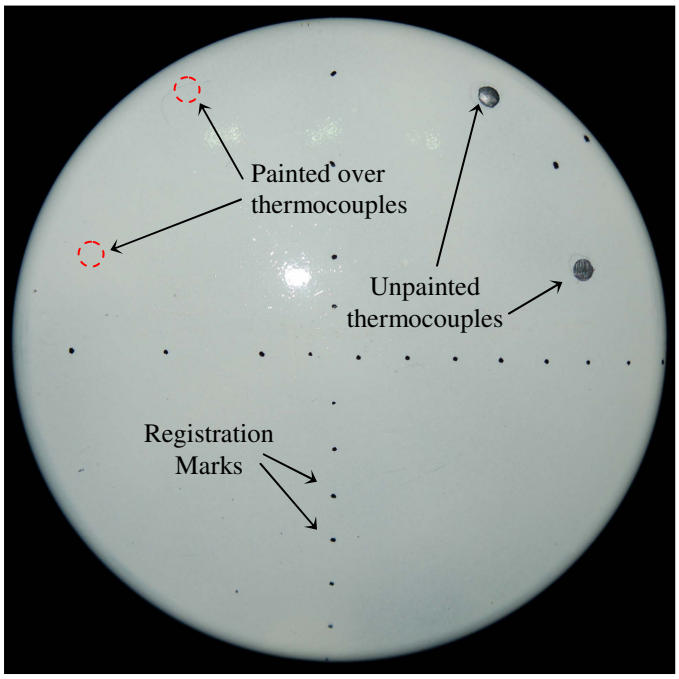

Fig. 28. Heat shield of the CEV model painted with temperature-sensitive coating (prior to Run 5).

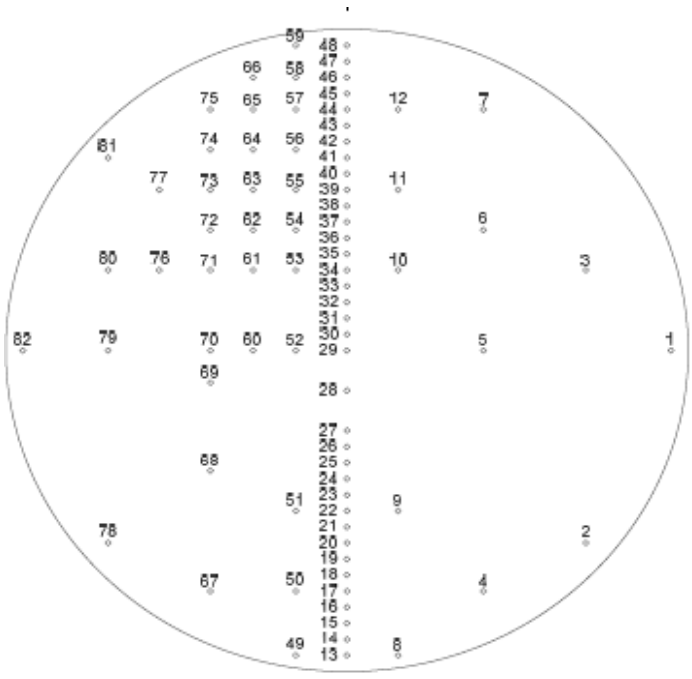

Fig. 29. Thermocouple layout on the surface of the test article's heat shield.

For each of the two paint jobs the coating thickness was measured using a Fischer Dualscope MP4C magnetic induction probe, which has accuracy of 0.02 mil (~ 0.5 μm) for measurements of coatings of up to 100 μm thick. One hundred measurements were made on the heat shield and the aft body to assess the uniformity of the coating. The average paint layer thicknesses were found to be 2.1 mil (approximately 53 μm) with a standard deviation of 0.15 mil and 1.7 mil (approximately 43 μm) with a standard deviation of 0.16 mil for the first and second paint jobs, respectively. The data collected using the experimental setup and the model described above are discussed in the next section.

3.3. Image Data Acquired

A number of pre-run and post-run images (between 10 and 230) were obtained to enable data correction for spatial non-uniformities. Note that in each set of run images there were two sequences of "dark" images corresponding to the two condensation clouds passing through the test cell during the startup portion of the run. For the $M_\infty = 10$, $Re = 5\times10^6$/ft run condition the first condensation cloud passes in about 70 ms, and the second one passes in about 120 ms. Fig. 30 shows the camera trigger and the condensation cloud passage times marked on the plot of the thermocouple temperature rise on the surface of the model during Run 3 ($M_\infty = 10$, $Re = 5\times10^6$/ft). Both condensation clouds obstruct the optical path to the camera and result in "dark" images, i.e. no data during those periods of time. The first condensation cloud has no significance for the data reduction since it passes through before there is any detectable temperature rise on the surface of the model as can be seen in Fig. 30. The second cloud, however, presents a problem for the data reduction algorithms proposed in Chapter 2 since the temperature starts rising rapidly at

the time of its passage. The methods presented in Chapter 2 require continuous temperature histories from the time when the model is at a uniform initial temperature, so a technique must be devised to deal with this issue. Several methods for filling in the data gaps are presented in Section 3.5.

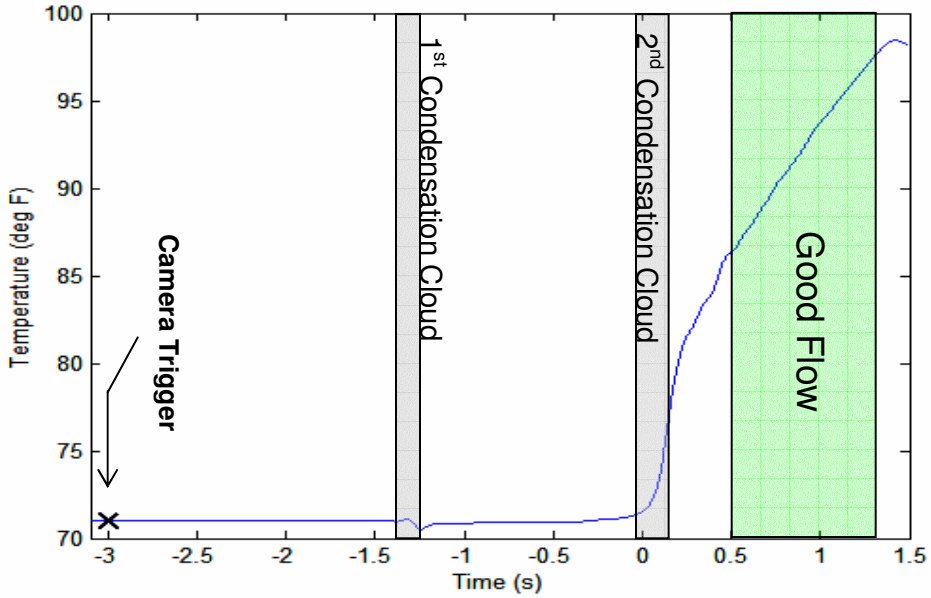

Fig. 30. Thermocouple temperature history on the surface of the model during Run 3 overlaid with important events and flow phenomena.

A sequence of raw run images acquired during Run 5 is shown in Fig. 31. The first image in the sequence was acquired before the start of the flow, and the remaining images were acquired during the "good flow" portion of the run. The number underneath each image indicates the frame number. The two black circles in the top right-hand quadrant of each image are the two unpainted thermocouples, so no TSP data are available at those locations. The "streaks" appearing in the images result from increased localized heating induced by particles impacting the model surface and effectively developing discrete roughness elements in the paint layer, which in turn disturbs the boundary layer and creates localized higher convective heating.

Fig. 32 illustrates when the TSP images were acquired compared with the data acquisition from the thermocouples for Run 3. The red line represents the surface temperature rise recorded by a thermocouple. Note that the thermocouple output is captured at 500 samples/s. Each gray bar corresponds to a TSP image acquired during the run, where the width of the bar represents the camera exposure time and the spacing between the bars represents the camera frame rate. It is evident that the temperature change during each 1.9-ms exposure is insignificant (i.e., it is reasonable to assume that the temperature captured by each frame represents an instantaneous reading at the time of the frame exposure.) It is also evident that the 42-fps frame rate, which was achieved by 2×2 camera pixel binning, is sufficiently high to resolve the heating rate encountered during this particular run. The next section discusses the data processing procedure to convert the raw TSP images into a useful format for the heat-transfer calculations.

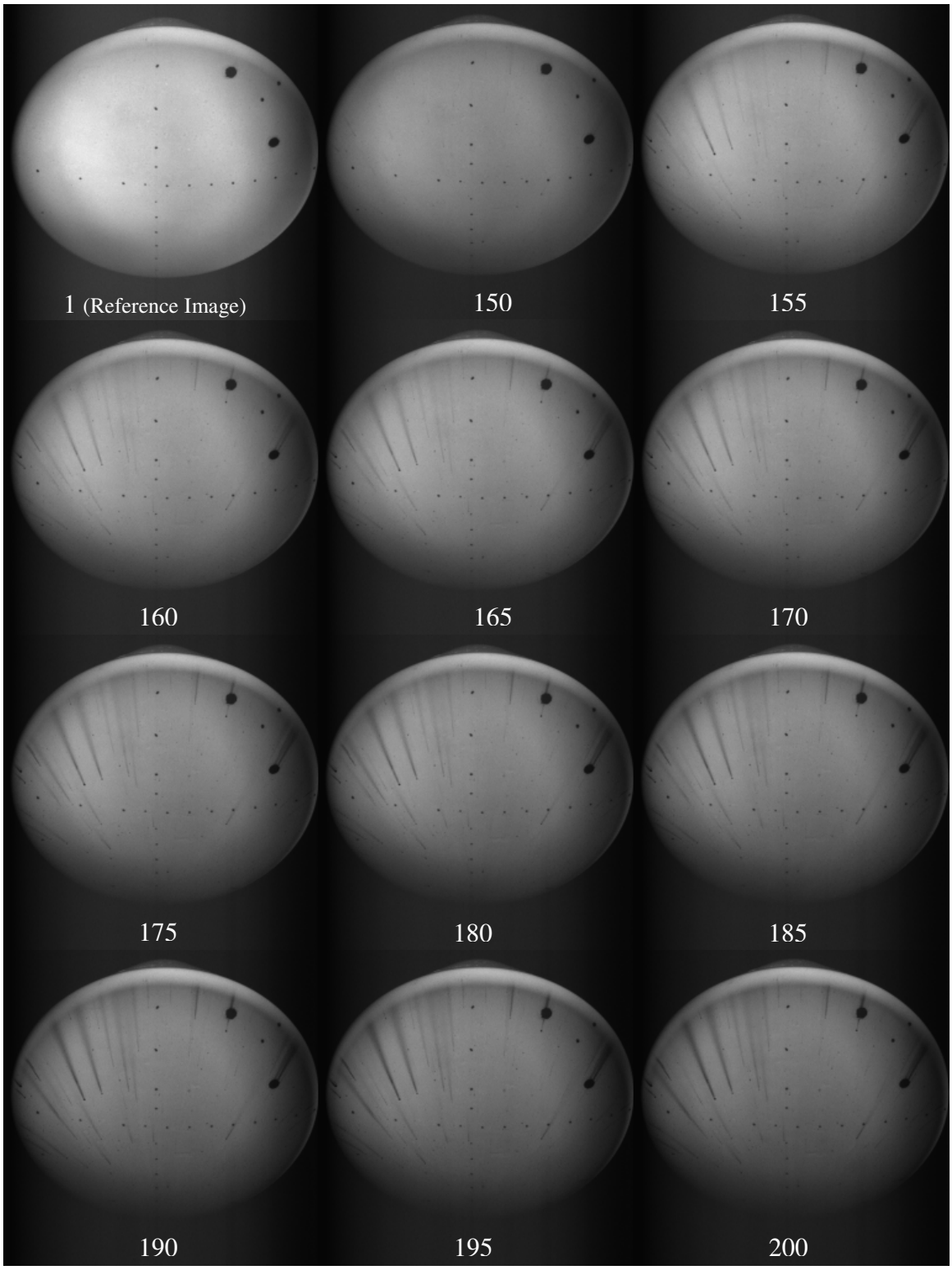

Fig. 31. A sequence of raw run images with corresponding frame numbers from Run 5.

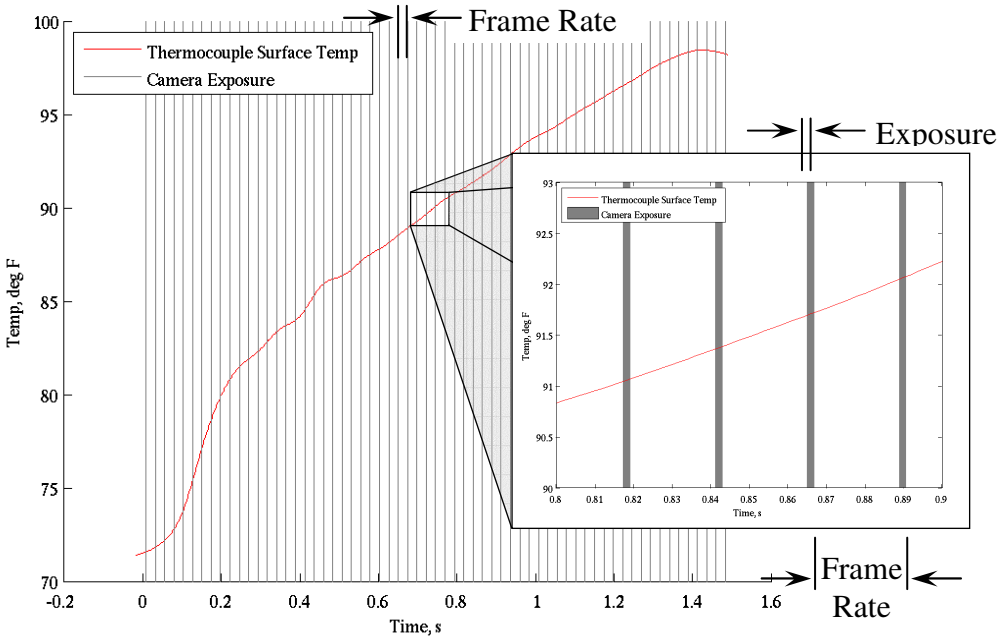

Fig. 32. Time history of TSP image acquisition for Run 3, Ref. 36.

3.4. Image Data Processing

This section describes the data processing steps that were necessary to prepare the raw image data for the heat-transfer calculations. First, the raw reference and run images were imported into Greenboot image-processing software as TIF images, where they were mapped to a 3D grid of the model's surface using an array of registration marks shown in Fig. 28. The grid was created in spherical coordinates since they were the most appropriate for the particular model geometry. Fig. 33 depicts the heat shield grid similar to the one used for the data mapping, but with

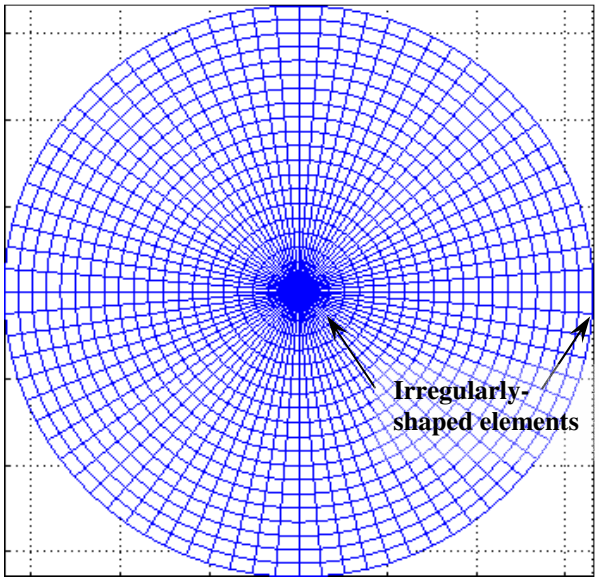

Fig. 33. Front view of the CEV grid.

reduced resolution (i.e. every 72nd element) for ease of viewing. The spherical grid resulted in high aspect ratio pie-shaped grid elements in the center of the heat shield and trapezoid-like elements at the edges of the heat shield, which caused some data distortions at those locations due to mapping of square pixels onto irregularly-shaped grid elements. To minimize this effect, the grid element size was matched to the pixel size as closely as possible at the half-radius locations.

Once mapped to a common grid, the run images were ratioed by a reference image. In general, a reference image is selected such that it is taken at a wind-off condition when the test article is at a uniform initial temperature. In this case, the 1st image of each run image sequence (e.g. 1st image in Fig. 31) rather than one of the pre-run images was selected as a reference image. The choice was justified since the cameras were triggered a few seconds prior to the start of the flow as shown in Fig. 30, and there were a large number of wind-off images in each run sequence. For instance, frame number 89 was the first wind-on frame of Run 5.

A sample mapped, ratioed image of the model's heat shield is shown in Fig. 34. Note that the raw images shown in Fig. 31 appear black and white, and the color in Fig. 34 was assigned by the image-processing software based on the intensity counts recorded by the CCD array. Also note that blue color

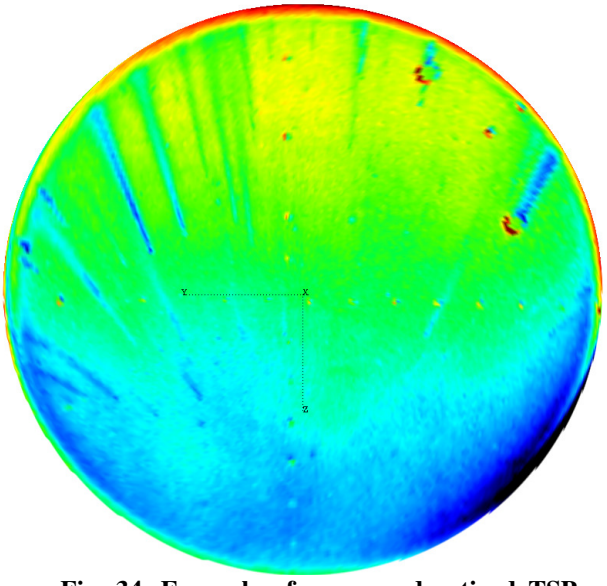

Fig. 34. Example of a mapped ratioed TSP image from Run 5.

corresponds to lower paint emission intensity and thus higher surface temperatures, which means the bottom of the heat shield is hotter than the top. This is expected since the test article was fixed at a 28° angle of attack during all of the TSP runs (i.e. the stagnation point was on the lower portion of the heat shield).

It should be noted that even though the image in Fig. 34 was acquired over a very short exposure time (1.9 ms) and at a relatively high frame rate (42 fps), the image quality and the signal-to-noise ratio are very good. This is attributed to the high quantum efficiency of the temperature-sensitive paint, the high intensity level of the illumination system, and an appropriately optimized camera system. The two unpainted thermocouples can be seen in the top right-hand quadrant of the heat shield in Fig. 34. No TSP data are available in those locations, so any apparent color in those spots is due to the image processing software extrapolating between pixels and minor image registration and mapping errors. The deepest blue color appearing in the lower right corner of the heat shield in the image does not represent aerodynamic heating, but is rather a combined result of the overlapping of two illumination sources and the peculiarity of the model geometry at this location, which resulted in inaccurate emission intensity data reading. As was mentioned earlier, the "streaks" appearing in the image are caused by particles impacting the model during the run and disturbing the boundary layer, which in turn resulted in increased local convective heating rates.

For each run, the sequence of mapped ratioed images, like the one in Fig. 34, was converted into surface temperature maps for the use with the 1st and 2nd data reduction methodologies described in Chapter 2 using an *a priori* calibration. The images were subsequently exported as data files (one for each frame) for the heat-transfer calculation

stage. For the 3rd data reduction methodology, the ratioed intensities were not converted into temperatures and were exported as is. The resulting data files contained a pixel number, a temperature or a ratioed intensity value, and an (x, y, z) coordinate of each pixel in an image. Note that the data files were not all the same size, i.e. same cell number in two different files (frames) does not necessarily correspond to the same (x, y, z) coordinate. These files were loaded into Matlab and used as the input boundary conditions for the data reduction algorithms described in Chapter 2.

An additional data processing step was required to apply the 3rd methodology. As described in Chapter 2, the 3rd methodology relies on anchoring of the ratioed intensity TSP data to the temperatures on the metal surface under the paint as opposed to applying an actual calibration to convert the TSP data into surface temperatures as in the 1st and 2nd methodologies. A sequence of "good flow" images was examined and six painted over thermocouples were selected for the calibration procedure for each run. It was found that for best results the calibration procedure had to be repeated for each run even if the runs were nominally the same (i.e. same freestream conditions and paint job). The main thermocouple selection criteria for the calibration procedure were that the selected thermocouples cover the range of temperatures that the test article experienced during a run and that the thermocouples are "streak-free", i.e. there are no localized time-varying heating spikes/variations due to particle impacts at the locations of the selected thermocouples. The TSP coating tends to create a lag in the thermocouple readings due to its insulative nature, which means that some of the rapid temperature changes due to the particle impacts may not be transmitted appropriately to the thermocouples, which in turn

may result in a bad calibration. The “streak-free” areas are easily identified by visual inspection of the raw run TSP images, like the ones shown in Fig. 31.

Once the six thermocouples were identified for the calibration procedure, their temperature readings were matched to the surface TSP ratioed intensity values at corresponding locations and times. The resulting calibration curves with corresponding equations for Run 3 and Run 5 are shown in Fig. 35 and Fig. 36, respectively. Note that while the two calibrations are slightly different, as would be expected since the paint jobs for the two runs were different, they are both linear. These calibrations were applied to the TSP data to convert the ratioed intensity values into temperatures at every pixel of every image. It is important to remember that the temperatures resulting from these calibrations are not the temperatures on the surface of the test article, but rather the temperatures that would be measured by thermocouples under the paint layer if there were a thermocouple located at every pixel under the paint. These temperature histories were then used as the input boundary conditions into a one-layer heat-transfer data reduction algorithm as described in Section 2.2.4. The next section describes some of the issues encountered during the data processing and analysis and the solutions that were implemented or can be implemented in the future to overcome these difficulties.

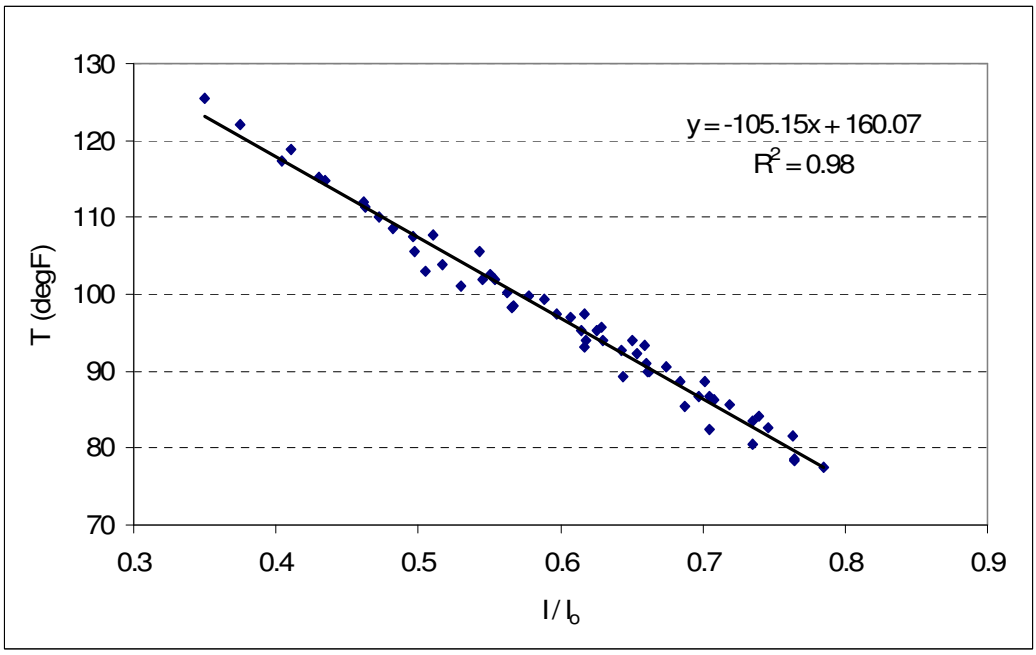

Fig. 35. Calibration curve for Run 3 data for the 3rd data reduction methodology.

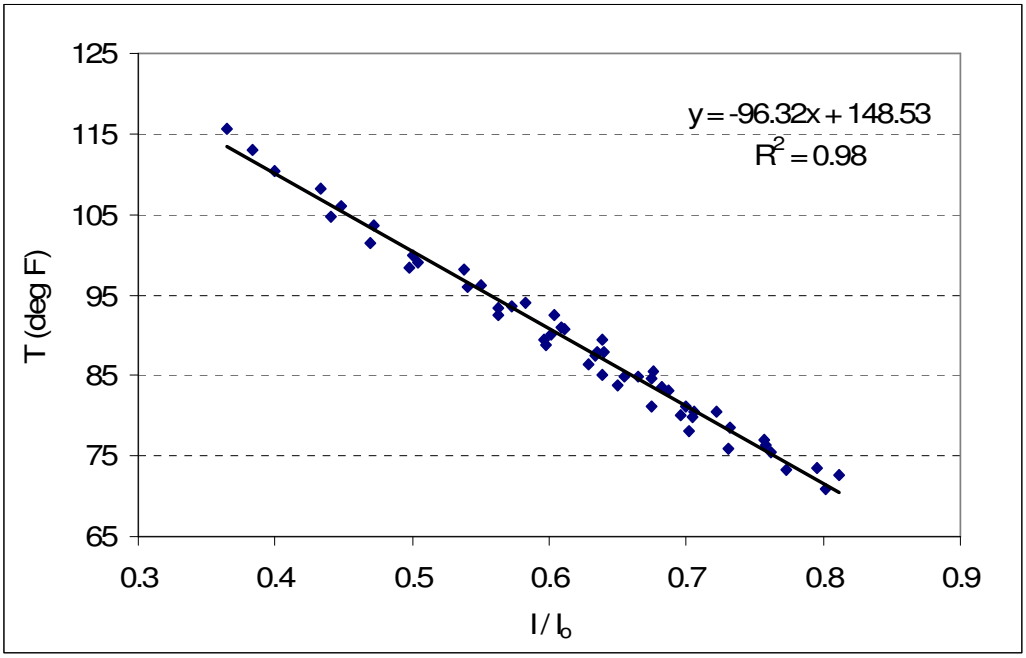

Fig. 36. Calibration curve for Run 5 data for the 3rd data reduction methodology.

3.5. Practical Data Reduction Considerations

The data processing methods outlined in the previous section result in a multitude of files which contain the location and the intensity or temperature value information for

each pixel in each image acquired during a run. The data in these files are not filtered in any way and contain any noise or "bad" data that may have been present in the original camera images. However, the data reduction techniques outlined in Chapter 2 are not well-equipped to deal with the real-world effects that most certainly will be present in any data set obtained experimentally. For instance, the proposed numerical scheme tends to amplify the random noise present in the data to the point where the calculated heat transfer is not within any reasonable margin of error. This section describes some of these issues and proposed solutions that were either applied to the data collected during the NASA CEV TSP test or can be implemented in the future.

3.5.1. Camera Frame Rate

The camera frame rate is an important system parameter for global heat-transfer measurement systems especially in a blowdown facility such as Tunnel 9 where the heat-transfer data reduction algorithm requires time histories of the surface temperature rise. The frame rate is defined by the camera capabilities, desired spatial resolution, and the size of the region of interest. The effective frame rate is also affected by the exposure time and the image readout rate. The required frame rate for heat-transfer calculations depends on the test conditions and the nature of the facility. To capture rapid changes in surface heating that may be encountered during a run where a test article is dynamically pitched, as high as possible frame rate is desired. For a static run with relatively low heating rates, however, a more modest frame rate may suffice.

As was mentioned earlier, the thermocouple data at Tunnel 9 are sampled at 500 Hz, but are low-pass filtered at 30 Hz, which is fast enough to resolve the majority of the heating loads models experience at the facility. With advancements in the CCD camera

technology, it is possible to acquire high quality images at relatively high frame rates, but there is always a tradeoff between image quality and quantity that can be acquired during a particular run.

Thus, a numerical study was conducted to investigate the influence of the data sample rate on the heat-transfer calculations. A number of representative thermocouple temperature histories collected at various tunnel conditions at the standard thermocouple sample rate of 500 Hz were taken, and the effective sample rate was reduced by down-sampling the data. For instance, to simulate the data collected at 250 Hz only every other data point was used. To maintain the convergence of the numerical scheme without altering the differential element size Δx, linear interpolation was applied to fill in the "reduced" data sets with points to artificially increase the sample rate back up to 500 Hz. These altered data sets were then used as inputs into the standard one-layer thermocouple data reduction algorithm described in Chapter 2, and the resulting heat fluxes were compared to the heat fluxes calculated using the original data sets. Two representative heating profiles, one from a static run and one from a dynamically pitching run, along with the errors associated with reducing the sample rate from 500 Hz all the way down to 10 Hz, are shown in Fig. 37 and Fig. 38, respectively. It is apparent that a sample rate as low as 25 Hz produces reasonable heat-flux results (within 2% error), but reducing the sample rate any lower may result in significant heating profile distortions. Note that this study did not take into consideration any random noise that may be present in the raw experimental data, which is likely to result in higher errors than predicted by this study. Much higher frame rates are required to allow for data filtering.

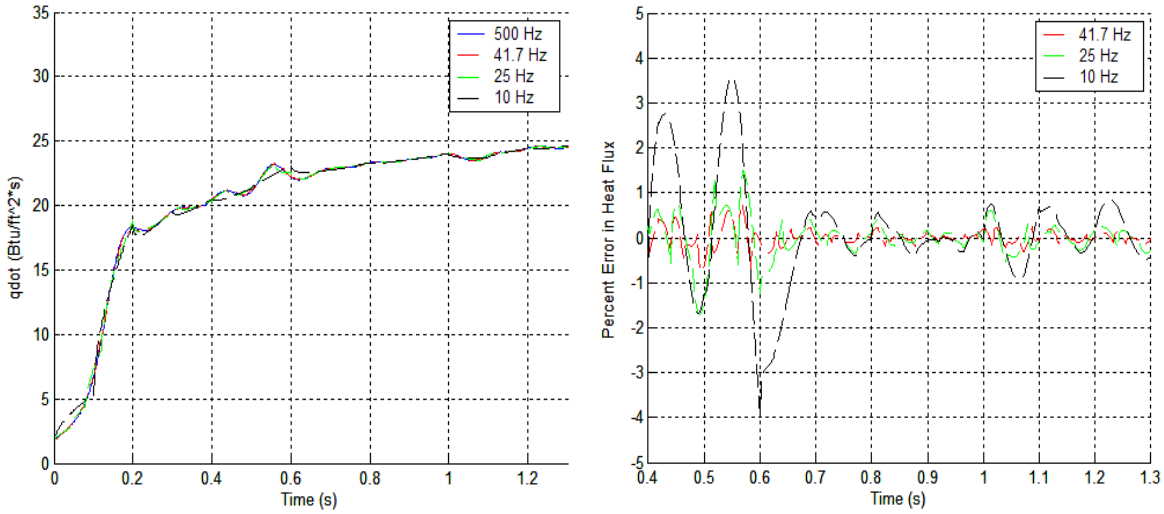

Fig. 37. Effect of reducing data sample rate on heat-flux calculations – sample heating profile #1.

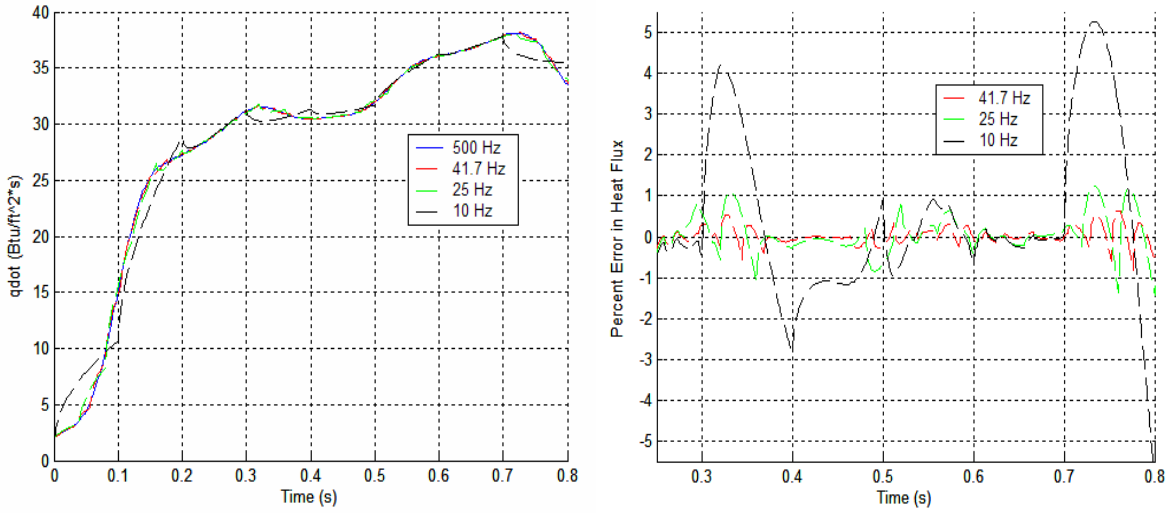

Fig. 38. Effect of reducing data sample rate on heat-flux calculations – sample heating profile #2.

3.5.2. Startup Data Recovery

As described in Section 3.3 and illustrated in Fig. 30, an image sequence from each run contains two sets of "dark" images (i.e. containing no data) as a result of the two condensation clouds passing through the test cell during the startup and obstructing the optical path to the cameras. The loss of data is inevitable since the phenomena that cause it are a part of the facility startup process. However, it presents a problem for the

numerical schemes proposed in Chapter 2 since they require continuous temperature histories from the start of the flow when the entire model is at a uniform initial temperature through the end of a run.

A numerical study was conducted to evaluate the error in calculated heat flux during the "good flow" period as a result of using ramps of various shapes to fill in the data gaps in the surface temperature time histories. A number of real thermocouple temperature histories representative of a range of heating profiles that may be encountered by a test article in Tunnel 9 were used for the study. Several ramp shapes were considered for filling in the data gaps including a straight line segment, a spline fit, and an exponential fit. To simulate the data loss due to a condensation cloud obstructing the optical path of a CCD camera, a data segment from startup portion of each thermocouple temperature history was removed and replaced by one of the ramp shapes mentioned above to connect the initial temperature, which is always known, and the next available data point. Subsequently, the heat flux was calculated using these new data sets and compared to the heat flux calculated using the original data. The results of the simulation were very encouraging: for all temperature profiles considered in this study the error in calculated heat flux was within 2.5% for the "good flow" portion of each run for linear fits, and it was within 1.5% for spline and exponential fits.

Sample original and modified temperature histories, resulting heat fluxes, and errors in calculated heat fluxes for linear ramp fits are pictured in Fig. 39, Fig. 40, and Fig. 41, respectively. The first plot in each figure corresponds to the data collected during a pitching run at $M_\infty = 10$, $Re = 4.5\times10^6$/ft condition, while the second plot in each figure corresponds to the data collected during a static run at $M_\infty = 10$, $Re = 14.6\times10^6$/ft

condition. Each plot contains several numbered curves, where each curve corresponds to a different thermocouple. Note that the error in Fig. 41 is plotted over the "good flow" period only for each of the two runs.

Plots of the temperature histories, calculated heat fluxes, and corresponding errors for the same two runs, but with the startup temperature data replaced with spline fits are presented in Fig. 42, Fig. 43, and Fig. 44, respectively. Corresponding plots with the startup data replaced with exponential fits are presented in Fig. 45, Fig. 46, and Fig. 47. Note that both spline and exponential ramps have their slopes matched to the slopes of the collected data sets at the location of the first available data point in each of the cases, which results in smooth calculated heat-transfer profiles in contrast to the ones calculated from the temperature histories with startup data replaced by linear ramps. The spline fits, however, are not representative of the real heating profiles. The temperature histories tend to dip below the initial temperature, which results in negative calculated heat transfer during a portion of the startup. This, however, does not significantly affect the error in calculated heat flux during the "good flow" portion of each run, so the spline ramps are still a good alternative to the liner ramps.

The exponential fits, in contrast to both linear and spline fits, are more representative of the actual heating profile shapes and are able to smoothly fill in the data gaps without falling into the negative region. Additionally, for some conditions (i.e. static runs with smooth heating profiles) the error in calculated heat flux is reduced by a factor of two or greater as compared to linear and spline fits. The exponential fits are described by the equation of the form $y = Ae^{Bx} + C$, where A and B are unknown coefficients and C is the initial temperature, which is known. A and B are the only two unknowns in the

equation. They can be found by solving the system of two equations in [Eq. (21)], where T and t are the temperature and the time at the first available data point and Slp is the slope of the temperature history curve at that point.

$$\begin{cases} T = \mathrm{A}e^{\mathrm{B}t} + \mathrm{C} \\ Slp = \mathrm{AB}e^{\mathrm{B}t} \end{cases} \tag{21}$$

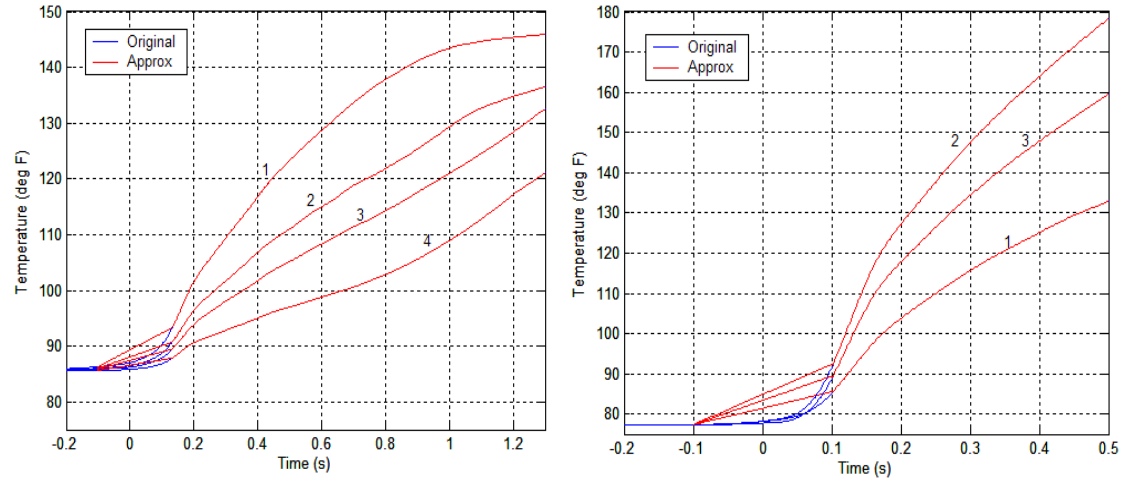

Fig. 39. Sample original temperature histories versus temperature histories with startup data replaced with straight line segments for two runs: M_∞ = 10, Re = 4.5×10^6/ft, pitching (left) and M_∞ = 10, Re = 14.6×10^6/ft, static (right).

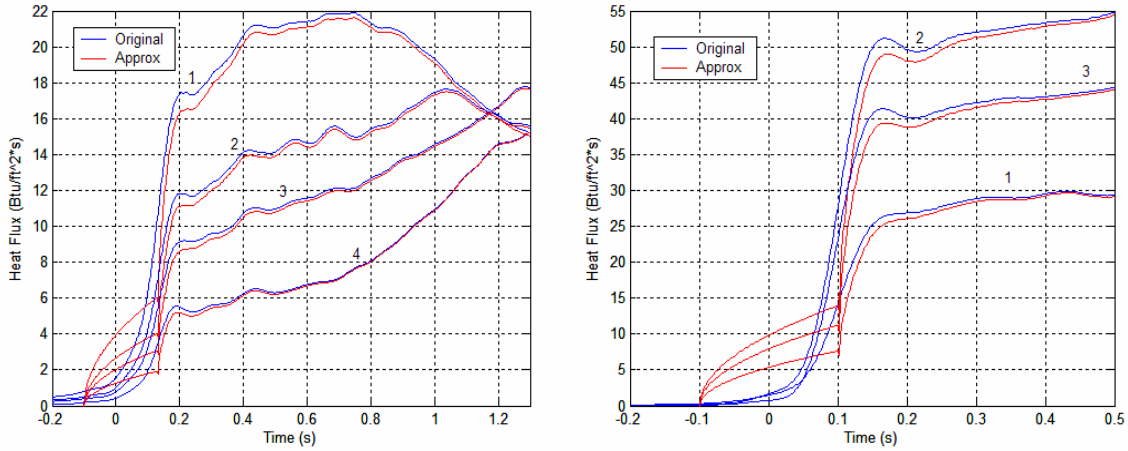

Fig. 40. Heat flux calculated using altered temperature histories versus the heat flux calculated using the original temperature histories (for straight line startup data fit).

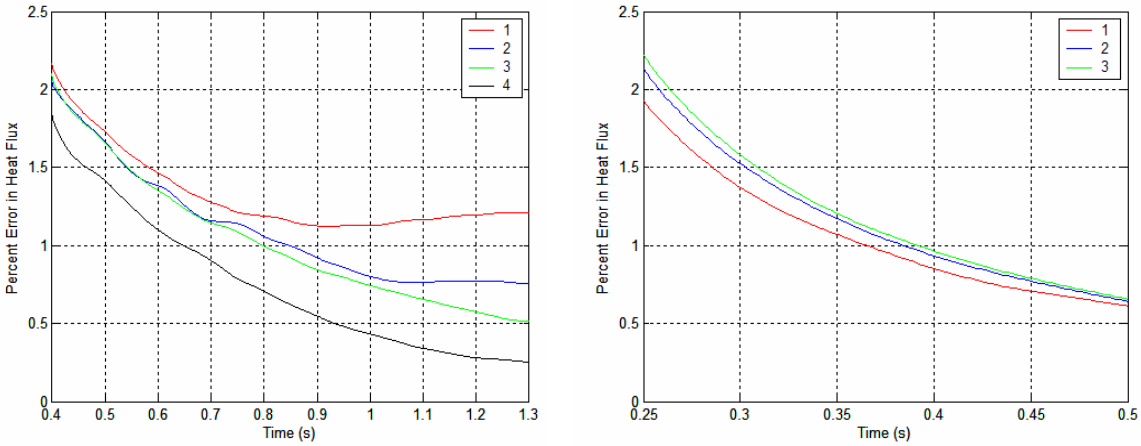

Fig. 41. Error resulting from replacing startup data with a straight line segment.

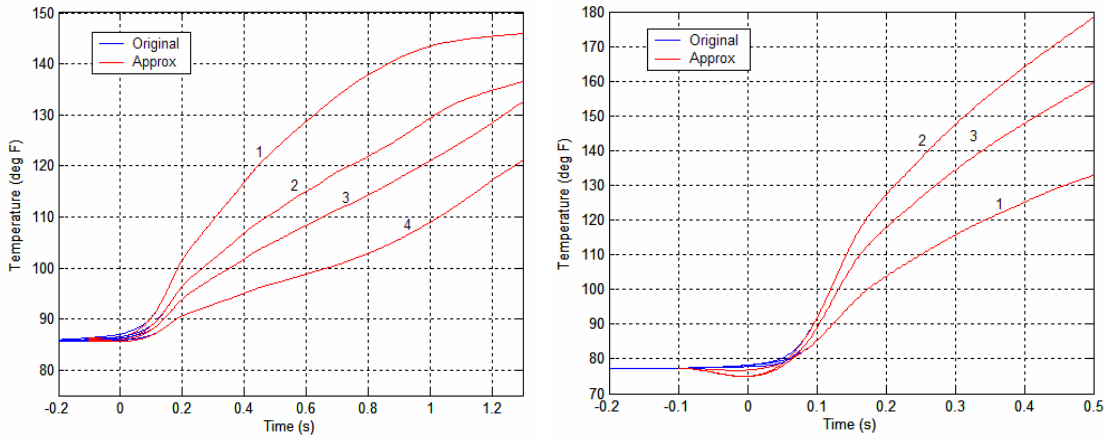

Fig. 42. Sample original temperature histories versus temperature histories with startup data replaced with spline segments for two runs: M_∞ = 10, Re = 4.5×10^6/ft, pitching (left) and M_∞ = 10, Re = 14.6×10^6/ft, static (right).

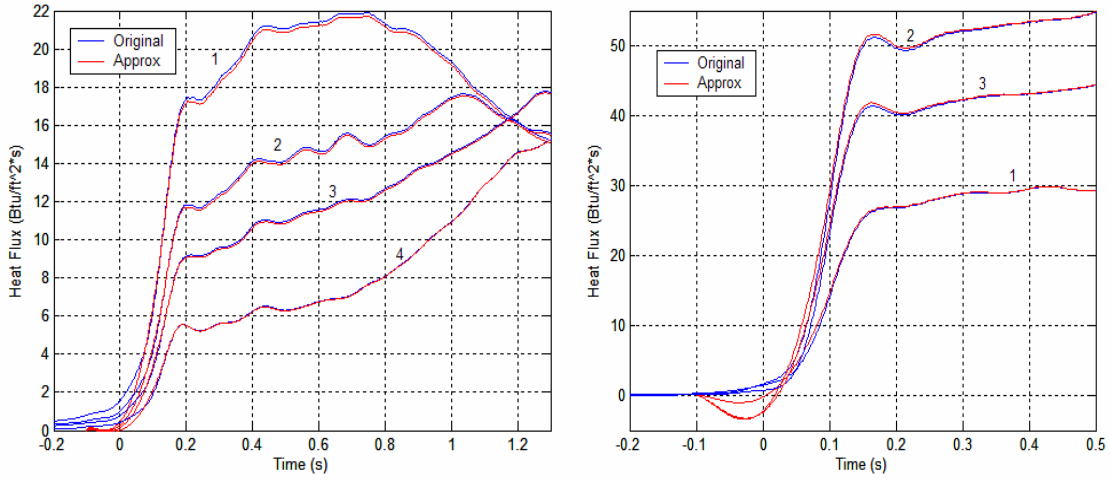

Fig. 43. Heat flux calculated using altered temperature histories versus the heat flux calculated using the original temperature histories (for spline startup data fit).

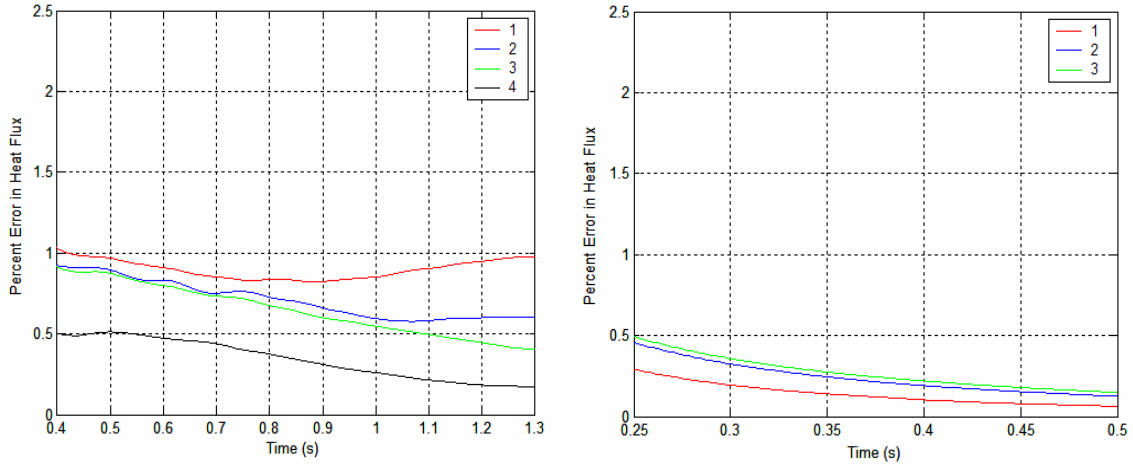

Fig. 44. Error resulting from replacing startup data with a spline segment.

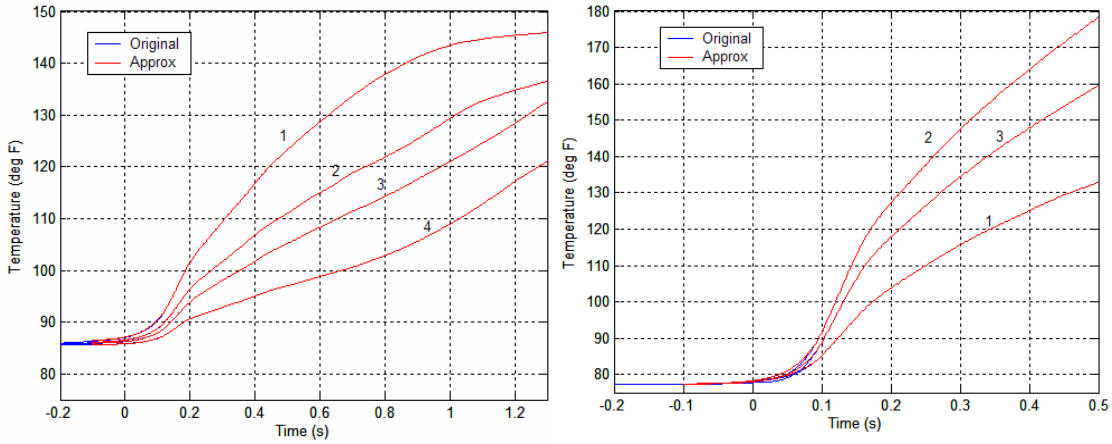

Fig. 45. Sample original temperature histories versus temperature histories with startup data replaced with exponential segments for two runs: M_∞ = 10, Re = 4.5×10^6/ft, pitching (left) and M_∞ = 10, Re = 14.6×10^6/ft, static (right).

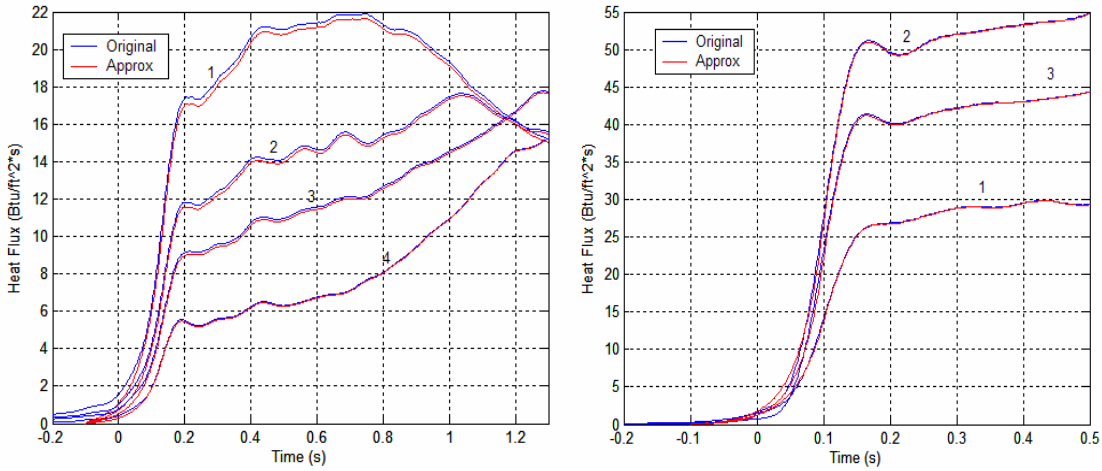

Fig. 46. Heat flux calculated using altered temperature histories versus the heat flux calculated using the original temperature histories (for exponential startup data fit).

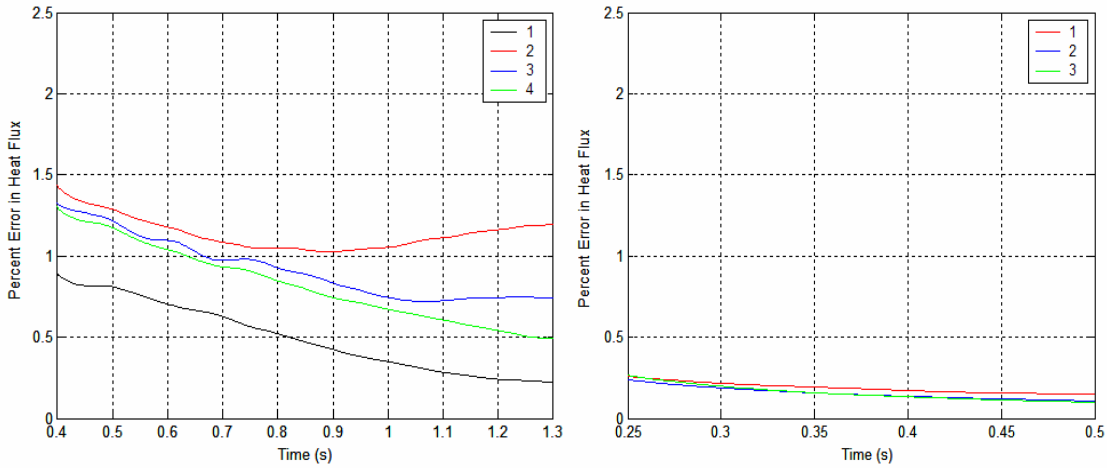

Fig. 47. Error resulting from replacing startup data with an exponential segment.

3.5.3. Noise

In any complex measurement system, there are many system- and test configuration-dependent factors that contribute to the noise in the experimentally obtained data. For the TSP system described in the present work, the noise due to each system component (e.g. CCD cameras, lights) as well as due to the facility itself has to be considered. In practice, however, it is difficult to distinguish between noise contributions from different sources. This section provides an indication of the overall noise level in the TSP data collected during the NASA CEV TSP test program described in Sections 3.1 – 3.4 and presents a method for dealing with the noise in the data reduction. Some possible noise sources are briefly discussed in the context of the TSP system developed at Tunnel 9.

The overall image-to-image (i.e. temporal) noise level for each run was assessed by comparing intensity values of a pixel from one frame to the next in the pre-run image sequences. The pre-run images were obtained at a wind-off condition when no temperature changes or model vibrations were occurring, so any intensity fluctuations were due to the noise present in the system. The plots of the normalized intensity time histories of a single pixel and of a spatial average of 4 adjacent pixels for 130 pre-run frames for Run 5 are presented in Fig. 48. The plots show that the temporal intensity fluctuations are about ± 2% for a single pixel and about ± 1% for a 4-pixel average. Thus, spatial averaging reduces the noise, but at the expense of reduced spatial resolution of the images. Similar noise levels were observed for other pixels in the image sequence as well as in the pre-run image sequences from other runs of the test program.

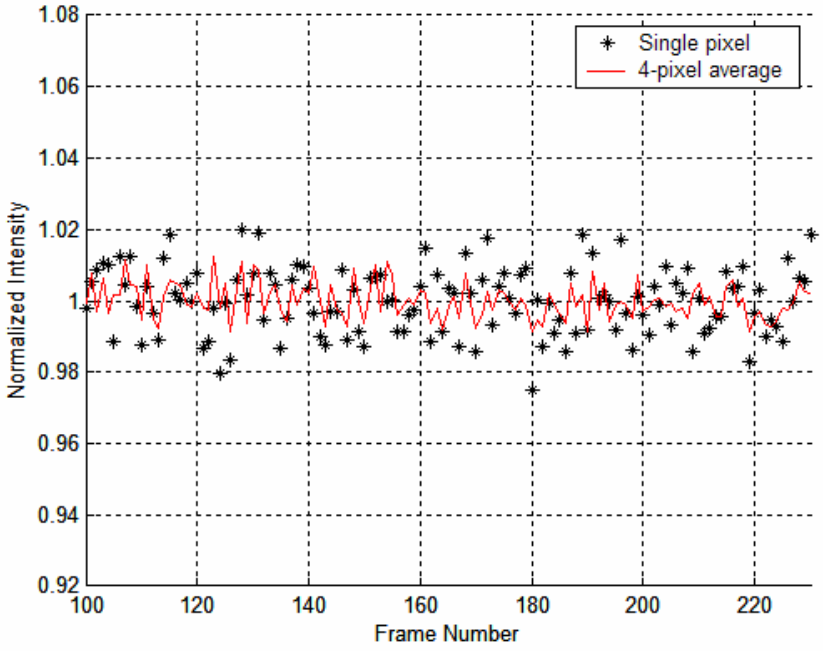

Fig. 48. Temporal variations of the normalized intensity of a single pixel and a 4-pixel average during a pre-run sequence for Run 5.

The noise levels present in the TSP data are problematic for the data reduction algorithms described in Chapter 2. The explicit finite-difference scheme used to calculate the heat transfer from the temperature data tends to amplify the noise, which results in excessive oscillations in the calculated heat flux if the TSP data are input into the data reduction algorithm as is. Furthermore, the camera frame rates, and thus the data sample rates, were too low to meet the convergence criteria defined by [Eq. (1)] in Section 2.2.1 for the scheme. To deal with these issues, the TSP temperature data were first re-sampled at a rate required for the finite-difference scheme to converge (e.g. 500 Hz; same as thermocouple sample rate). Subsequently, the data were low-pass filtered at about 5 Hz by a 4^{th} order Butterworth filter to "smooth out" the noise. Fig. 49 shows the original TSP temperature data for one pixel from Run 5 collected at 42 fps and the corresponding filtered curve obtained by first artificially increasing the sample rate to 500 Hz and then applying the low-pass Butterworth filter. Note that the startup data are missing from the

original data set. The data gap was filled in with a linear ramp prior to applying the filter as described in Section 3.5.2. The procedure was applied to smooth out the temperature histories at every pixel, and the filtered data sets were then used as the inputs into the data reduction algorithm to calculate the heat transfer for the NASA CEV TSP test. This method ensured the convergence of the finite-difference scheme used in the data reduction and also attenuated the excessive oscillatory behavior of the calculated heat flux. Some possible sources of the noise in the TSP data are discussed next.

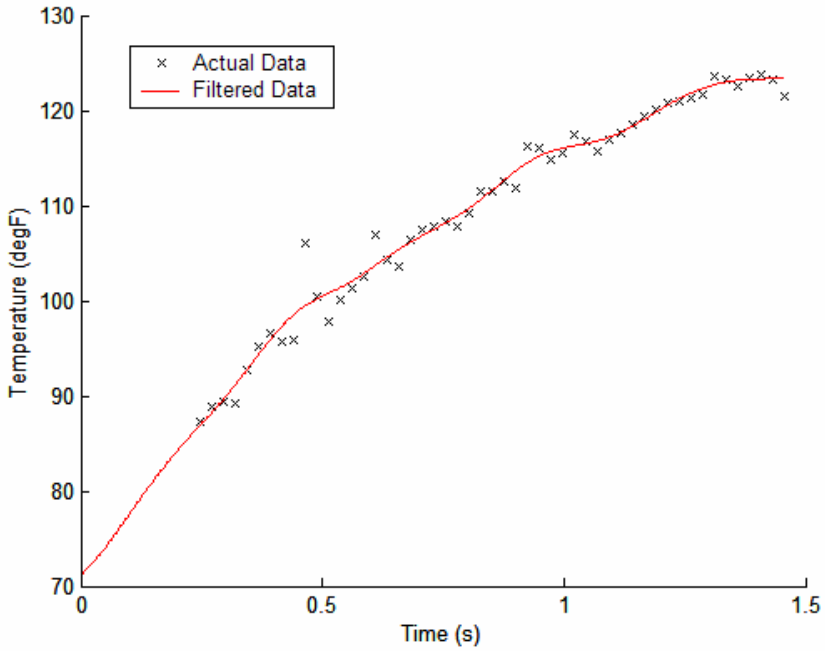

Fig. 49. A comparison of actual TSP temperature data history with the TSP data that was re-sampled, then filtered with 4th order Butterworth low-pass filter.

Examples of possible random noise sources include the CCD camera noise, which can include dark current, photon shot noise, and readout noise, spatial and temporal variations in the illumination field, image registration errors, and ambient lights.[37] Dark current is the thermally induced charge, which can accumulate on the detector in the absence of light. It is only important for long exposures in low-light level cases, and can

be significantly reduced or eliminated by cooling the CCD chip. The CCD cameras used at Tunnel 9 are cooled to -70 °C, and so the noise due to dark current is considered to be negligible. Any signal (dark or light) produces photon shot noise, which equal to the square root of the signal. It is a quantum effect described by Poisson statistics and cannot be eliminated. However, cooling of the CCD chip reduces shot noise due to the dark current by reducing the dark current itself. The readout noise is generated by the amplifier on the CCD array and sets the detection limit for cooled CCDs at low signal levels.[37] For high signal levels (as in the case of the NASA CEV TSP test) the photon shot noise dominates and the readout and the dark current noise can be neglected. The noise specifications as per manufacturer's description for the cameras used at Tunnel 9 are summarized in Table 3.

Table 3. PhotonMAX: 512B Noise Specifications

Readout noise (typical)	"On-chip multiplication gain" amplifier	"Traditional" amplifier
	~ 40 e- rms @ 5 MHz ~ 50 e- rms @ 10 MHz Read noise effectively reduced to < 1 e- rms with on-chip multiplication gain enabled	8 e- rms @ 1 MHz 15 e- rms @ 5 MHz
Dark current at -70 °C	0.005 e-/pixel/sec (typical) 0.01 e-/pixel/sec (maximum)	
Spurious events (typical)	0.005 e-/pixel/frame CIC measured with 33 sec exposure time and ~ 1000× (maximum) multiplication gain	

The image registration is performed to properly align the reference and the run images acquired at the wind-off and the wind-on conditions, respectively, as described in Section 3.4. However, this process of correction for the model's movement is itself error-prone. There are errors associated with the locations of the registration marks in the model and the pixel coordinates. These errors are exacerbated by the fact that the

registration marks may be several pixels in size (as in the NASA CEV TSP test). Additionally, any model movement during a single exposure tends to smudge the registration marks in an image, which results in additional errors. One way to eliminate the errors associated with the image registration is to eliminate the need for a reference image altogether, as discussed in more detail in the next section.

During the NASA CEV TSP test conducted at Tunnel 9, care was taken to turn off the room lights prior to each run to make sure they did not interfere with the acquired data. The temporal light fluctuations of each mercury-xenon arc lamp illuminating the model were monitored using photodiodes. The normalized light fluctuations for 4 of the 5 lights for Run 5 are shown in Fig. 50. It is evident that the temporal light fluctuations for the mercury-xenon arc lamps used at Tunnel 9 are much less than 0.05 % and can be neglected.

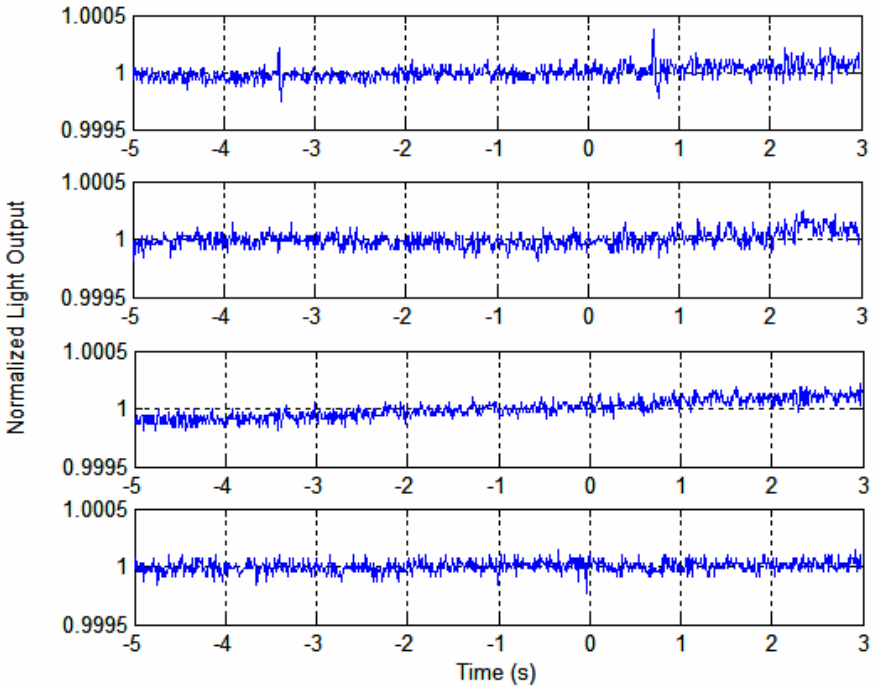

Fig. 50. Normalized light fluctuations for Run 5 for four of the five mercury-xenon arc lamps used during the NASA CEV TSP test.

The largest source of error for most intensity-based TSP systems is the relative motion between the test article and the illumination field during a run.[37] The relative motion is caused by the sting deflection between the wind-off and the wind-on conditions and by the model vibrations during a run. There also may be an additional noise component due to the spatial-temporal flutter of the arc of the mercury-xenon arc lamps used to illuminate the test articles during the TSP tests. For single luminophore intensity-based TSP systems, a reference image is usually acquired at the wind-off condition to correct for the spatial non-uniformities in the illumination field and in the coating itself. Such a reference image, however, cannot account for a shift in the illumination field due to the model deflection and/or vibrations, or arc flutter during a run. The next section provides a detailed discussion of the spatial-temporal illumination field variations issue and possible ways of dealing with it.

3.5.4. Reference Image Selection

A reference image is required for the intensity-based global measurement techniques to account for any possible spatial non-uniformities in the coating or the illumination field on a model's surface. Theoretically, when a run image is ratioed by a reference image acquired when the entire test article was at a uniform initial temperature, all of the surface emission variations that are not due to the temperature changes cancel out. If the reference and the run images are acquired at wind-off and wind-on conditions, respectively, or at different instants in time during a run, they have to be mapped to a common grid before dividing one by the other to make sure the images align properly. This works well to correct for any spatial coating non-uniformities since the coating at any given location on a model is fixed with respect to that location even as the model

deflects between the wind-off and the wind-on positions or vibrates during a run. This, however, is not true for an illumination field. Even if the lights themselves are perfectly stable, as the model deflects between the wind-off and the wind-on positions and vibrates during a run, the illumination field on the surface changes with time since the lights are fixed in the absolute frame of reference. This means that if the illumination field is not spatially uniform to begin with, the ratioing technique does not actually correct for these non-uniformities.

To reduce the data acquired on the NASA's CEV capsule model using the TSP system at Tunnel 9, one of the first few images of each run sequence was used as a reference image as described in Section 3.4. This means that while the coating non-uniformities were ratioed out, any non-uniformities in the illumination field that may have been present were not properly corrected for. Care was taken during the test setup to create a uniform illumination field on the model's surface. However, some non-uniformities were inevitable due to the optical access limitations and lights overlapping when attempting to illuminate the entire model surface with sufficient intensity. This resulted in additional noise in the data collected during the test.

Two-luminophore paints are designed to deal with this issue. In the case of TSP (similar ideas are applicable to PSP and thermographic phosphors), these paints combine temperature-sensitive (probe) and temperature-insensitive (reference) luminophores, where both are excited by a light of the same wavelength. Ideally, the emission wavelengths of the two luminophores do not overlap so that they could be completely separated by optical filters. Ratioing of the probe by the reference image corrects for the illumination non-uniformities since both images are acquired at the same instant in time,

i.e. it is actually the same image which contains two components: one is temperature-sensitive, and the other is temperature-insensitive. A wind-off image is still required to correct for any non-uniformities in the spatial distribution of the two luminophores in the paint mix. More specifically, a ratio of ratios is used to correct for both the illumination and the coating non-uniformities: first each probe image is ratioed with the corresponding reference image, and then each of these ratios for a run sequence is ratioed with the ratio of the wind-off probe and reference images.[15] A two-luminophore TSP formulation for the use at Tunnel 9 is currently under development.

3.5.5. Effects of Uncertainty in TSP Material Properties and Layer Thickness

As outlined in Section 2.2.2, the 1st data reduction methodology requires the knowledge of the temperature-sensitive coating thickness. A fairly accurate measurement of the paint layer thickness is possible, although tedious. A magnetic induction probe, which allows coating thickness measurements on metal substrates at discrete points was used successfully to measure the paint layer thickness on the NASA CEV model as described in Section 3.2. Nevertheless, it is important to determine the sensitivity of the heat-transfer calculations to the perturbations in the measured paint layer thickness values.

In addition to the coating thickness, the knowledge of the thermal conductivity, K is also required. The measurement of the thermal conductivity of the coating used at Tunnel 9 is much more difficult than the paint layer thickness measurement. The paint formulation has thermal conductivity which is a non-linear function of temperature. Furthermore, the thermal properties may change with paint layer thickness (bulk vs. thin film material properties)[38], and there may be variations in the properties from batch to

batch. The method presented in Section 2.2.3 proposes a way to estimate the thermal conductivity *in situ*, which provides an indication of the thermal conductivity as a function of temperature for the particular formulation and thickness used on a test article. However, it is still only an estimate, so it is important to determine the sensitivity of the heat-transfer calculations to the variations in the measured/estimated thermal properties of the coating if the 1st or 2nd methodologies proposed in Chapter 2 are to be utilized.

To assess the effect of perturbations in the thermal conductivity and the paint layer thickness on the calculated heat-transfer rate, a sensitivity analysis was performed using the same ANSYS 1D transient heat conduction model described in Section 2.3 (see Fig.17). First, a nominal temperature distribution was obtained on the surface of the model for a set of nominal properties and paint layer thickness with a nominally chosen step heat input applied for 1.4 sec, which is a representative run time for Tunnel 9. For the study of the sensitivity to the perturbations in the paint layer thickness, the thickness was varied in increments of 0.5 mil with all other parameters held constant, and the surface temperature distribution obtained from the nominal case was applied to the model as a boundary condition. The resulting heat flux was compared to the nominal values to determine the error in calculated heat flux. For the study of the sensitivity to the perturbations in the thermal conductivity, a similar procedure was implemented, except in this case the thermal conductivity was varied in increments of 10% with all other parameters held constant.

From this simple sensitivity analysis it was found that underestimating the thickness of the temperature-sensitive coating layer by 50% resulted in an approximately 35% error in the calculated heat transfer, while overestimating the thickness by 50%

resulted in an approximately 21% error. This nonlinear trend in the calculated heat-flux error with the change in the measured paint layer thickness is consistent with the experimental results presented by Ohmi et al.[27] To put these results in perspective, based on the standard deviation of 0.15 mil for the 2.1-mil paint layer thickness, which was measured on the surface of the NASA CEV model for the first paint job, the paint layer's thickness is known within 7.5%. This gives an estimated error of about 4% in the calculated heat-transfer rate based only on the uncertainty in the paint layer thickness. Note that the error in the calculated heat flux associated with the uncertainty in the measured paint layer thickness is greater than the error associated with the linear temperature gradient through the paint layer assumption, which was estimated to be ~ 1% for most Tunnel 9 test conditions (see Section 2.3).

Additionally, the study showed that the error in calculated heat flux increased linearly with increasing error in the thermal conductivity, K: a ±10% error in K resulted in approximately ±5% change in the calculated heat flux. Similarly, a ±20% error in K resulted in an approximately ±10% change in the calculated heat flux. The results from the sensitivity studies are presented in Fig. 51 and Fig. 52. The above analysis confirms that the coating thickness used for the NASA CEV TSP test (on the order of 2 mil) cannot be ignored in the data reduction since it would lead to excessive errors in the heat-transfer calculations. It is also evident that assuming a constant thermal conductivity of the coating for the heat-transfer calculations, as is done in other TSP data reduction algorithms, would lead to significant errors due to considerable variation in the thermal conductivity values over the temperature range that is likely to be encountered during a typical Tunnel 9 run. The above discussion leads to the conclusion that if the thermal

conductivity and/or thickness of the coating cannot be determined with sufficient accuracy, the 3rd data reduction methodology described in Section 2.2.4 would yield the best results since it does not require any knowledge of the thermal properties or of the thickness of the paint layer.

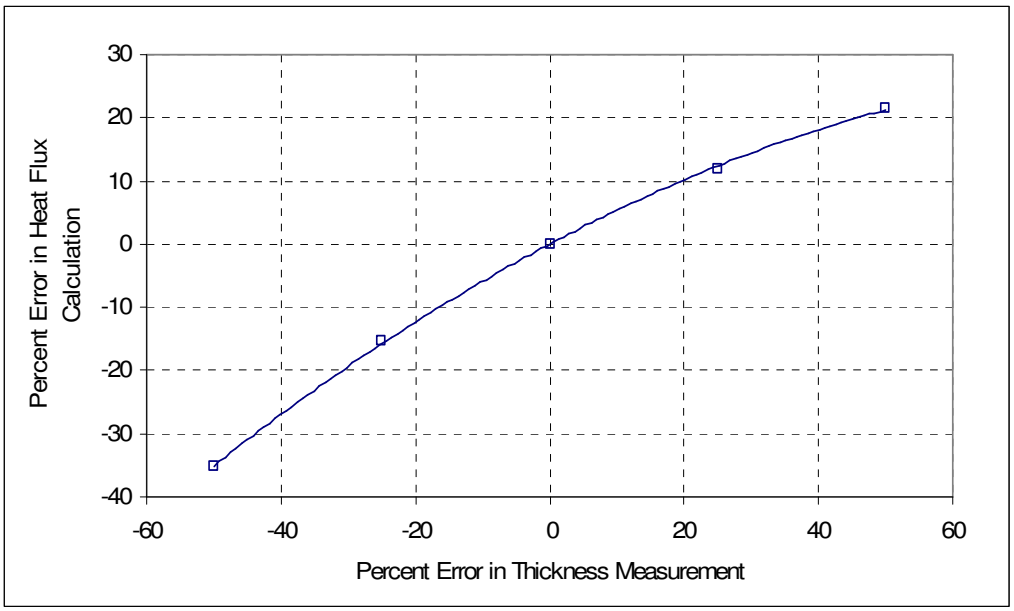

Fig. 51. Errors in calculated heat flux resulting from errors in paint layer thickness measurements.

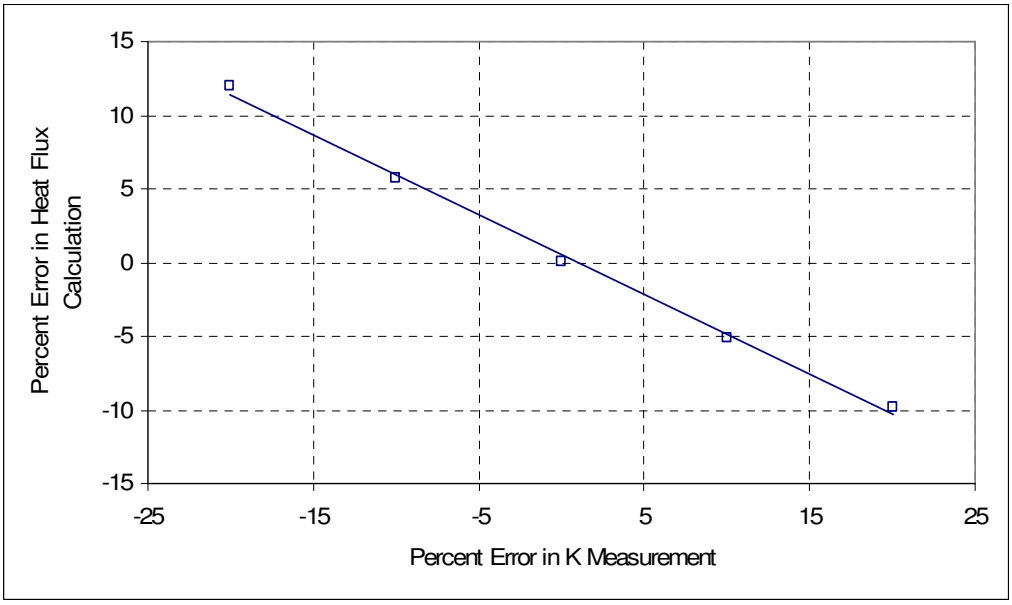

Fig. 52. Errors in calculated heat flux resulting from errors in thermal conductivity measurements.

Chapter 4. Results and Conclusions

4.1. Thermal Conductivity Estimate

An estimate of the thermal conductivity of the temperature-sensitive coating as a function of temperature was obtained using the TSP and the thermocouple data from Run 3 of the NASA CEV TSP test program as described in Section 2.2.3 (previously reported in Ref. 36). The resulting $K(T)$ estimate is plotted in Fig. 53 along with the $K(T)$ of the polyurethane-based synthetic enamel paint measured by Paul et al. The latter material is similar to the TSP formulation used at Tunnel 9 and is used for comparison with the TSP $K(T)$ estimate since no measured TSP thermophysical property data are currently available. The two thermal conductivities appear to be in a reasonable agreement. Note that the estimated $K(T)$ extends the temperature range to lower temperatures than $K(T)$ measured by Paul et al. It is observed that there is a strong gradient in K as a function of temperature at these lower temperatures. This reinforces the notion that K of the TSP formulation cannot be assumed constant for the heat-transfer calculations at Tunnel 9 since the test articles are initially at a room temperature and only reach higher temperatures corresponding to the more "level" part of the K-curve toward the end of a run.

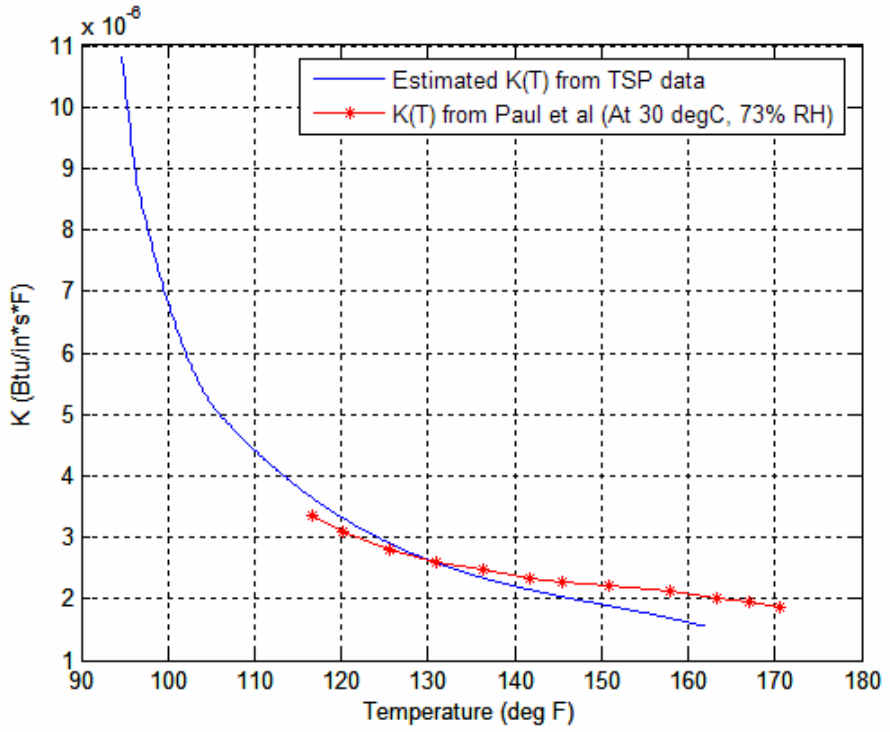

Fig. 53. *K*(*T*) of the TSP estimated using the data collected during the NASA CEV TSP test vs. *K*(*T*) reported by Paul et al. for a similar coating, Ref. 36.

4.2. Qualitative and Quantitative Heat-Transfer Results

The 3rd data reduction methodology described in Section 2.2.4 was used to calculate the heat transfer from the TSP data collected during the NASA CEV TSP test. This methodology was chosen for the final data reduction stage because it does not require any knowledge of the thermophysical properties or the thickness of the temperature-sensitive coating or of the calibration relating the TSP emission intensity to its temperature, hence eliminating any uncertainty associated with these parameters. Note that only the heat shield data from Runs 3 and 5 (M_∞ = 10, Re = 5×10^6/ft for both) are presented here. The heat shield geometry itself consists of a large radius of curvature spherical portion, which transitions to a small radius of curvature toroidal part at the edges as illustrated in Fig. 54. Based on the geometry, the heat transfer was calculated in Cartesian coordinates everywhere on the spherical heat shield portion (i.e. surface with

negligible curvature) and in cylindrical coordinates on the toroidal part where the curvature could not be neglected.

The TSP surface emission intensity data collected during Runs 3 and 5 were converted into temperatures using the calibrations presented in Fig. 35 and Fig. 36, respectively. These temperatures were used as the boundary conditions to calculate the heat-transfer rates as described in detail in Chapter 2. The heat-transfer results were then non-dimensionalized as Stanton number and normalized by the baseline stagnation point value. Note that the baseline heat-transfer data used for TSP data normalization and validation in the present work are the data obtained from the standard discrete instrumentation (i.e. thermocouples) during a non-TSP run at the same angle of attack and freestream conditions as the TSP runs examined here. All of the spatial coordinates (i.e. x, y, z, r) were normalized by the radius of the heat shield of the test article, R. The resulting non-dimensionalized and normalized heat-transfer maps are presented below. To validate the heat-transfer maps, the heat-transfer data along several vertical section cuts where thermocouples were present under the coating were compared to the heat flux calculated from the thermocouple data from a baseline run at the corresponding locations. The plots depicting the comparison are presented below as well.

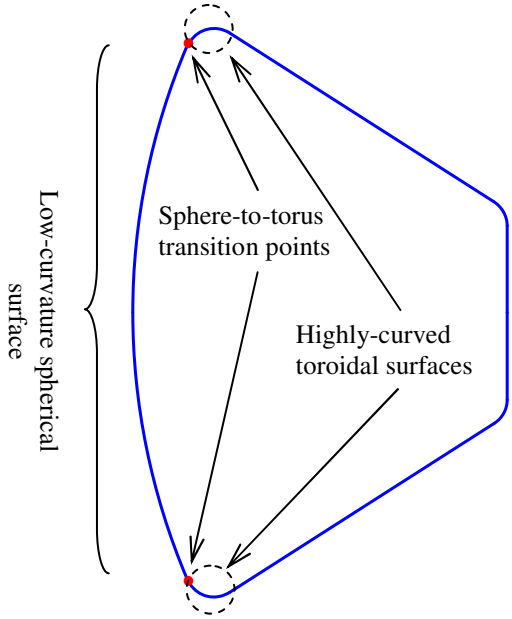

Fig. 54. Side view projection of the test article.

Fig. 55 shows the normalized Stanton number map of the test article's heat shield at time t = 0.7 sec for Run 3. Some of the features in Fig. 55 may be best understood by examining Fig. 56, which shows the temperature-sensitive coating on the surface of the heat shield prior to Run 3. Note that during the first TSP application used for Runs 1 – 4, three thermocouples were left unpainted versus just two unpainted thermocouples left during the second coating application, as described in Section 3.2 and shown in Fig. 28. Also note that the trip insert (an artifact from the non-TSP portion of the test program) was painted separately from the rest of the heat shield during the first coating application (Runs 1 – 4) as opposed to the entire heat shield being painted at once, as was done during the second paint application (Run 5). Additionally, the paint was touched-up prior to Run 3 in the areas where it incurred damage as a result of small particle impacts during the previous

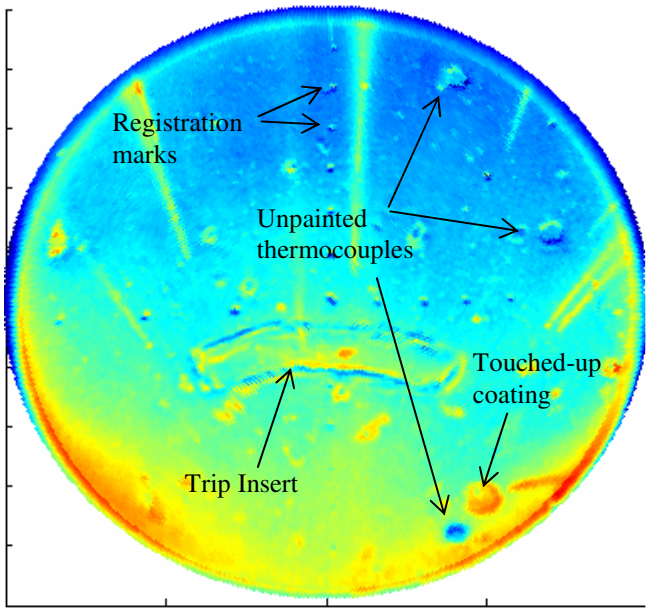

Fig. 55. Normalized Stanton number map at t = 0.7 sec for Run 3 (M_∞ = 10, Re = 5×10^6/ft).

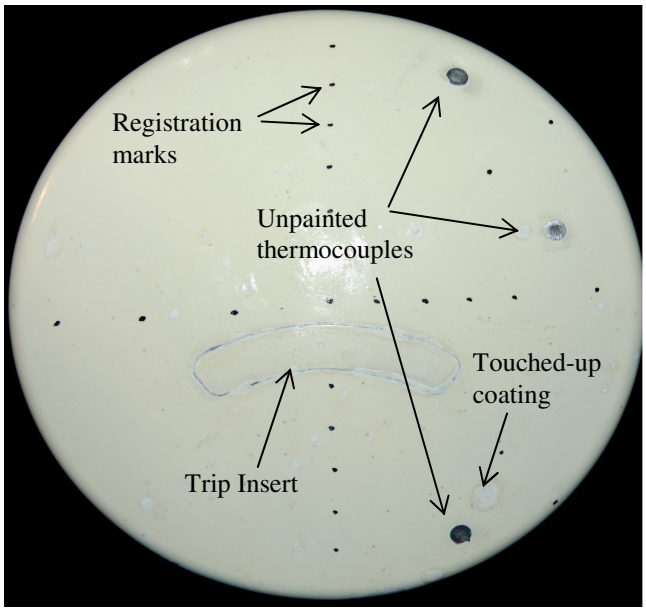

Fig. 56. Heat shield of the CEV model prior to Run 3.

high Reynolds number run. The unpainted areas around the thermocouples, the trip insert, and the paint touch-ups all contributed to the unevenness of the surface of the test article during Run 3, which locally affected the flow, and thus the surface heating pattern during the run, as can be seen in Fig. 55.

It is important to remember that no TSP data are available at the locations of the unpainted thermocouples, so any apparent color in those spots is due to the image processing software extrapolating between pixels and minor image registration and mapping errors. The "streaks" appearing in the image in Fig. 55 are due to small particles impacting the test article's surface and locally disturbing the boundary layer, which results in increased localized convective heating. These features appear in all of the heat-transfer maps presented in this section.

Fig. 57 shows the normalized Stanton number map of the test article's heat shield at time t = 1 sec for Run 3. The normalized Stanton numbers along six section cuts where thermocouples were present under the coating are shown in Fig. 58, Fig. 59, Fig. 60, Fig. 61, Fig. 62, and Fig. 63, which correspond to y/R = 0, -0.15, 0.15, 0.275, -0.4, and 0.4, respectively and are marked by the six vertical dashed lines in Fig. 57. The TSP data along the section cuts are validated against the thermocouple heat-flux data obtained during a baseline run at the corresponding locations. The two data sets appear to be in good agreement except for a few areas on the model's surface. Some of the discrepancies between the thermocouple and the TSP data present in Fig. 58 – Fig. 63 are discussed next.

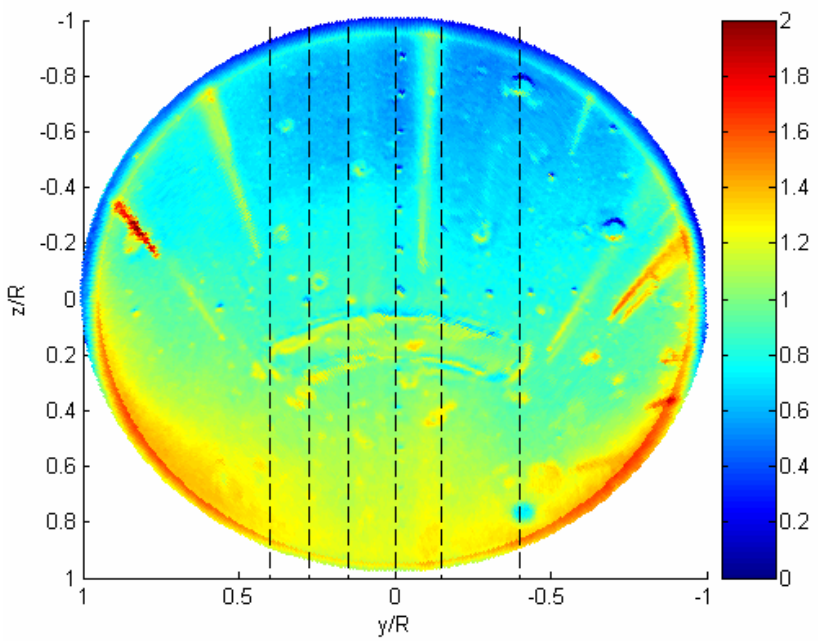

Fig. 57. Normalized Stanton number map at t = 1 sec for Run 3 (M_∞ = 10, Re = 5×10^6/ft); section cuts at y/R = -0.4, -0.15, 0, 0.15, 0.275, and 0.4 are marked with vertical dashed lines.

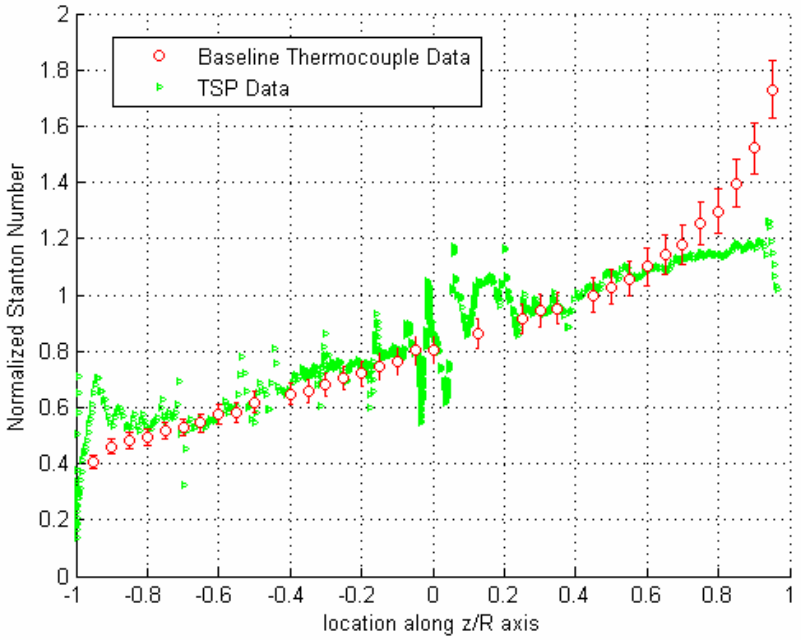

Fig. 58. Normalized Stanton number section cut at y/R = 0 (centerline) vs. z/R location at t = 1 sec for Run 3.

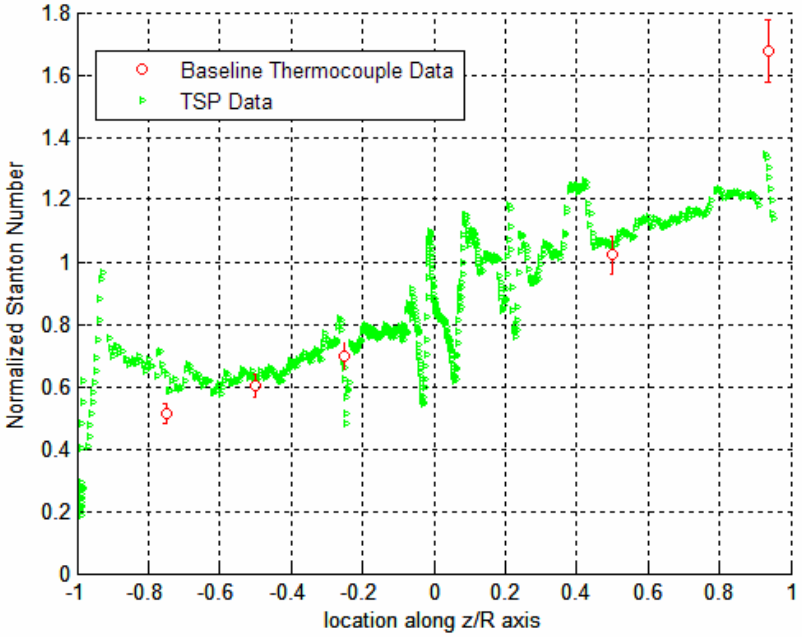

Fig. 59. Normalized Stanton number section cut at *y*/R = -0.15 vs. *z*/R location at *t* = 1 sec for Run 3.

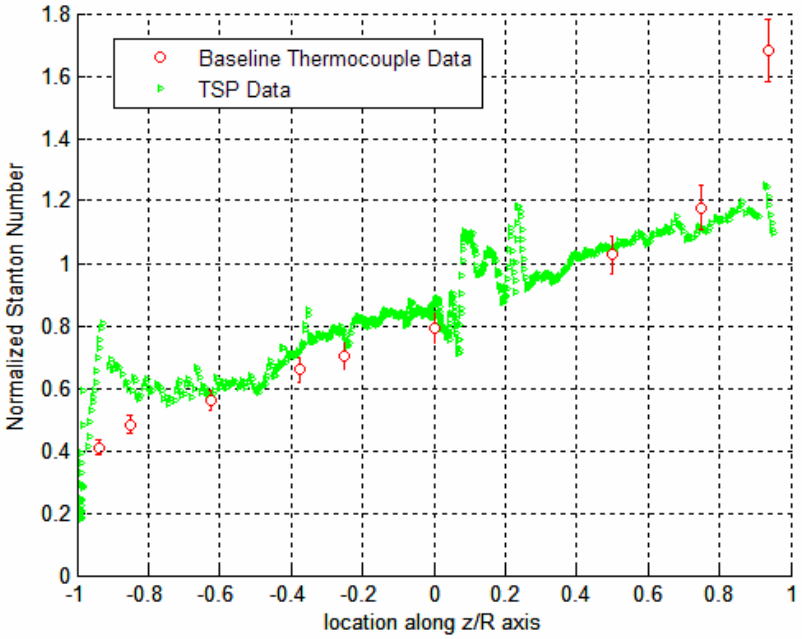

Fig. 60. Normalized Stanton number section cut at *y*/R = 0.15 vs. *z*/R location at *t* = 1 sec for Run 3.

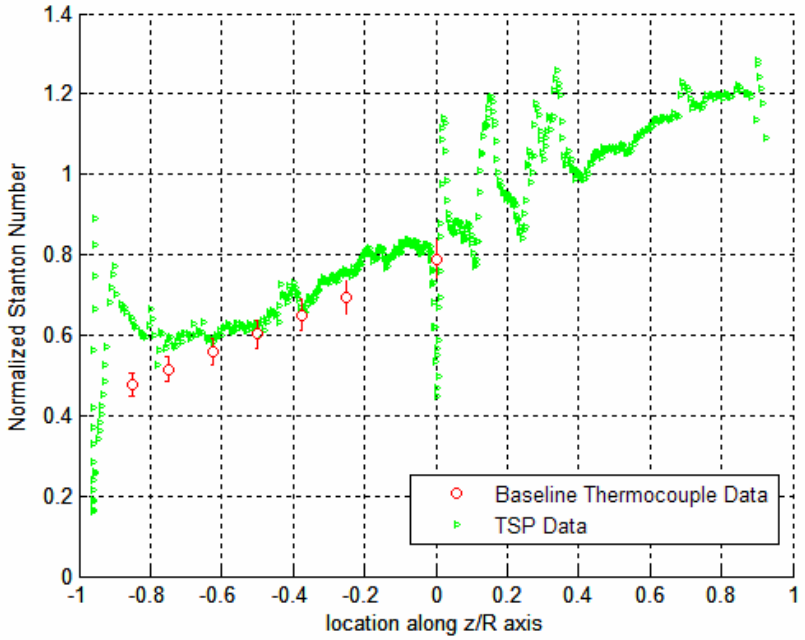

Fig. 61. Normalized Stanton number section cut at *y*/R = 0.275 vs. *z*/R location at *t* = 1 sec for Run 3.

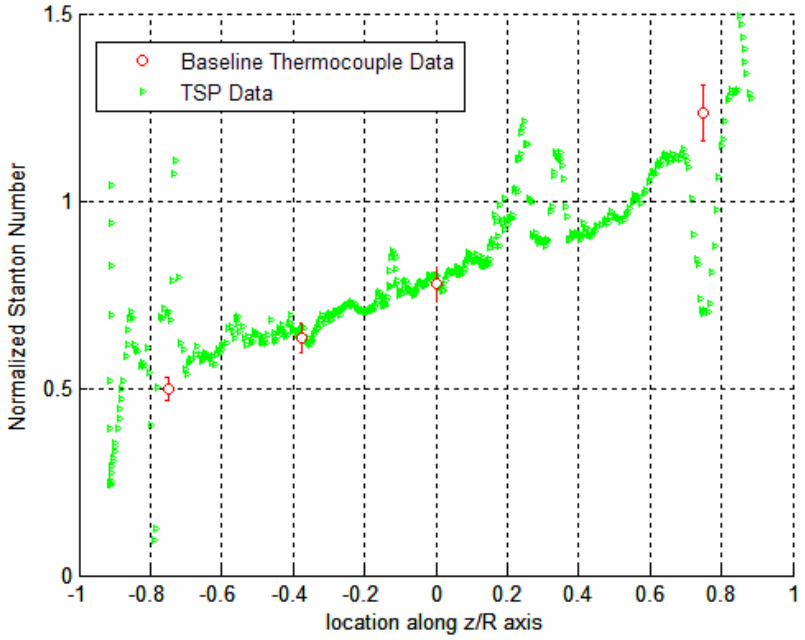

Fig. 62. Normalized Stanton number section cut at *y*/R = -0.4 vs. *z*/R location at *t* = 1 sec for Run 3.

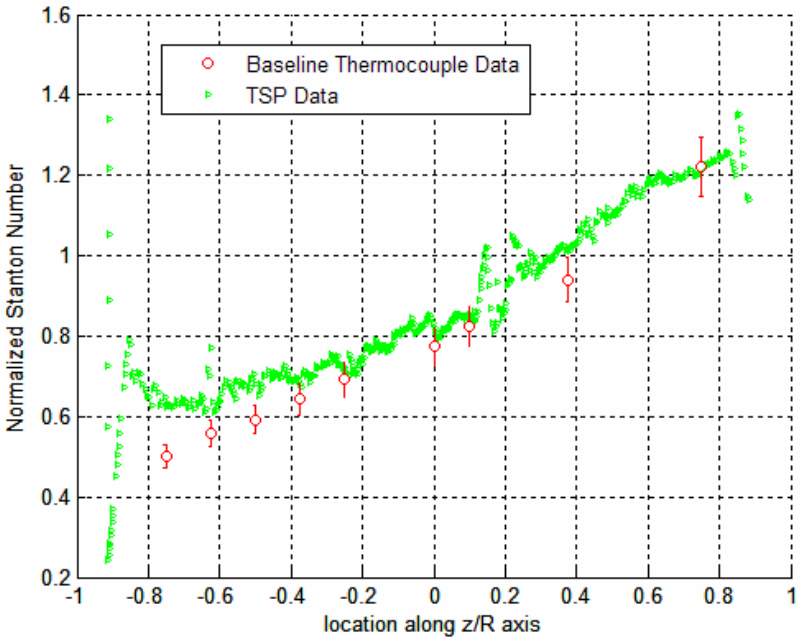

Fig. 63. Normalized Stanton number section cut at *y*/R = 0.4 vs. *z*/R location at *t* = 1 sec for Run 3.

There is a distinct spike present in the TSP data in Fig. 58 – Fig. 63 between *z*/R ~ -0.95 – -0.85, which in each figure corresponds exactly to the location where the heat shield geometry transitions from spherical to toroidal shape (*r*/R = 0.95), as shown in Fig. 54. As was mentioned above, the data reduction algorithm transitions from Cartesian to cylindrical coordinates at this location since the curvature of the toroidal section of the heat shield is non-negligible. The heating spike is expected to occur at this location and is absent from the thermocouple data partly because there was no thermocouple installed at the location of the transition between the two parts of the heat shield and partly due to 2D and 3D conduction effects washing out the spatial gradient. This illustrates one of the disadvantages of discrete instrumentation as compared to global measurement techniques: important flow features may be missed if there happen to be no sensors at the appropriate locations on a model's surface.

Each of the section cuts presented in Fig. 58 – Fig. 63 passes over the trip insert located in the center of the test article. Due to the unevenness and discontinuities in the coating in this area, the data in the region are scattered and should be disregarded. The TSP data between $z/R \sim -0.8 - -0.7$ and $z/R \sim 0.7 - 0.8$ in Fig. 62 are considered invalid since the section cut on these intervals passes over the regions around two of the unpainted thermocouples as can be seen in Fig. 57.

The TSP data deviate from the thermocouple data at $z/R > 0.8$ in Fig. 58 – Fig. 60. This is attributed to an extremely oblique camera viewing angle (12°-24°) with respect to the lower quarter of the heat shield surface, which resulted in the TSP data under-predicting the heat-transfer rate.

Fig. 64 shows a normalized Stanton number map of the test article's heat shield at time $t = 1$ sec for Run 5. As described in Section 3.4, the bright red region in the lower right-hand quadrant is attributed to invalid emission intensity reading due to two illumination fields' overlapping and should not be interpreted as a high-heating region. The heat-transfer maps from Runs 3 and 5 presented in Fig. 57 and Fig. 64, respectively are very similar (i.e. the heating levels and the flow patterns are similar), which is expected since the run conditions were the same for both runs. However, a few dissimilarities arise from the differences in the quality of the coating during each of the runs. Namely, the coating was reapplied to the entire test article (including the trip insert) prior to Run 5, so the paint layer was smooth and uniform as can be seen in Fig. 28, which resulted in less flow disturbances and a smoother heating profile as compared to Run 3.

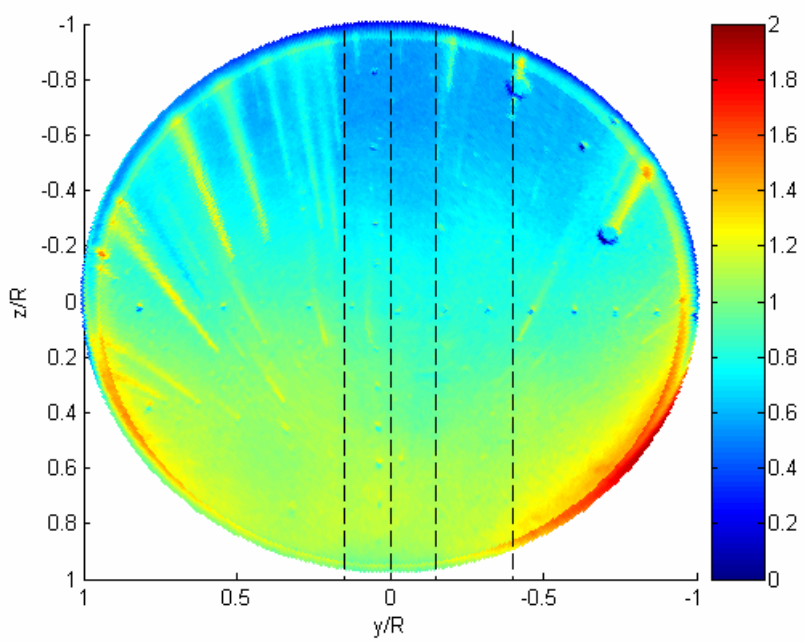

Fig. 64. Normalized Stanton number map at t = 1 sec for Run 5 (M_∞ = 10, Re = 5×10^6/ft); section cuts at y/R = -0.4, -0.15, 0, and 0.15 are marked with vertical dashed lines.

Similarly to Run 3, no TSP data are available at the locations of the two unpainted thermocouples in the top right-hand quadrant in Fig. 64. The normalized Stanton numbers along four section cuts where thermocouples were present under the coating are shown in Fig. 65, Fig. 66, Fig. 67, and Fig. 68, which correspond to y/R = 0, -0.15, 0.15, and -0.4, respectively and are marked by the four vertical dashed lines in Fig. 64. Once again, the TSP data are compared to the thermocouple heat-flux data from a baseline run, which was the same run for Runs 3 and 5 since the freestream conditions and the angle of attack were the same for both. The two data sets are in good agreement except for a few areas on the model's surface. The differences between the thermocouple and the TSP data present in Fig. 65 – Fig. 68 are discussed below.

Similarly to the data from Run 3, there is a distinct spike present in the TSP data in Fig. 65 – Fig. 67 at z/R ~ -0.95, which corresponds to the location where the heat

shield geometry transitions from spherical to toroidal shape, as discussed above. The TSP data deviate from the thermocouple data at $z/R > 0.7$ in Fig. 65, and at $z/R > 0.8$ in Fig. 66 and Fig. 67. A similar trend was noted in the Run 3 data and is attributed to an extremely oblique camera viewing angle with respect to the lower quarter of the heat shield surface. The TSP data between $z/R \sim -0.8$ and ~ -0.7 in Fig. 68 are also considered inaccurate since the section cut in this interval passes over one of the unpainted regions around a thermocouple as can be seen in Fig. 64.

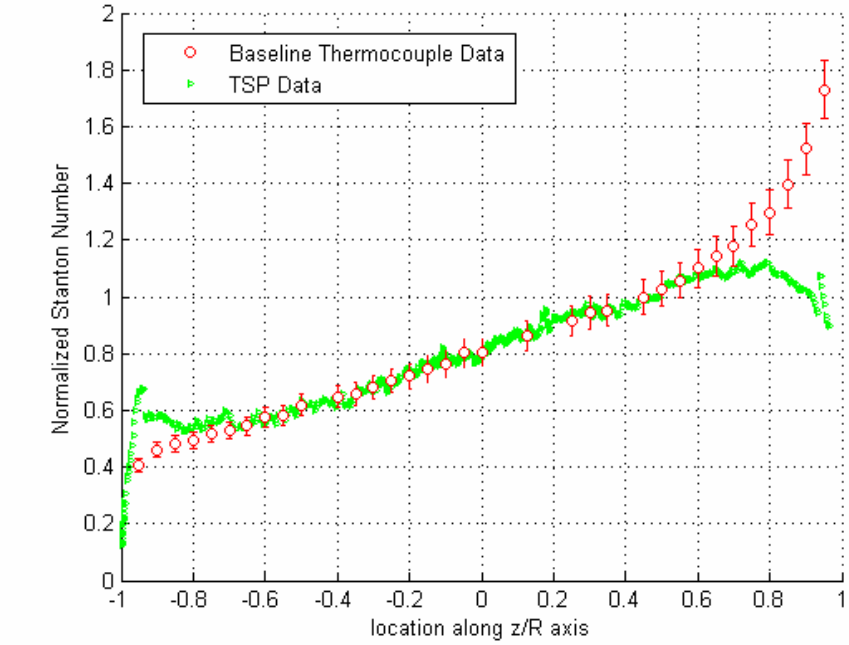

Fig. 65. Normalized Stanton number section cut at $y/R = 0$ (centerline) vs. z/R location at $t = 1$ sec for Run 5.

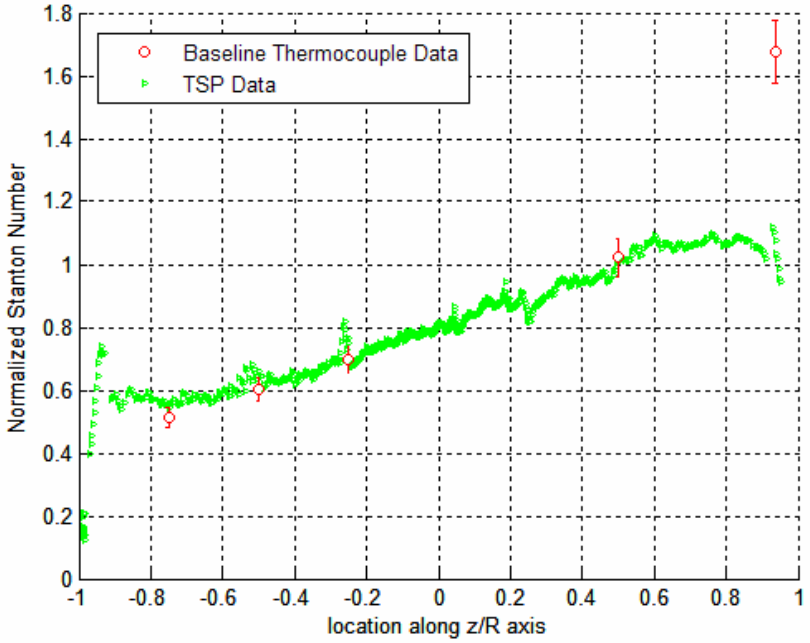

Fig. 66. Normalized Stanton number section cut at *y*/R = -0.15 vs. *z*/R location at *t* = 1 sec for Run 5.

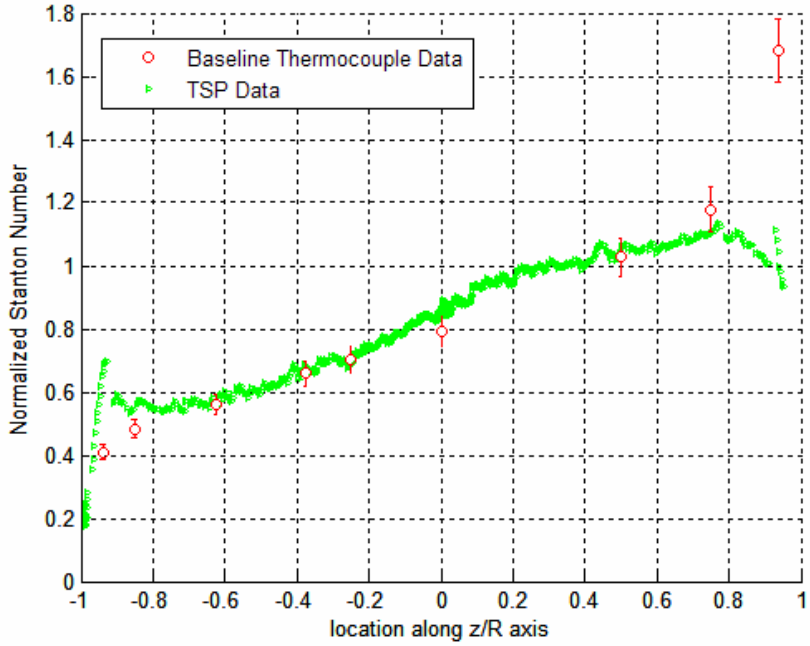

Fig. 67. Normalized Stanton number section cut at *y*/R = 0.15 vs. *z*/R location at *t* = 1 sec for Run 5.

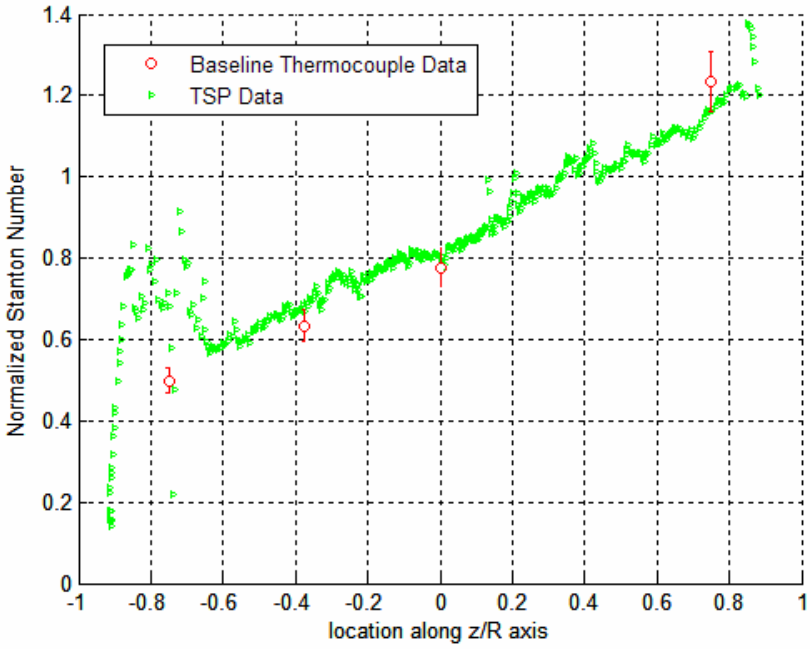

Fig. 68. Normalized Stanton number section cut at *y*/R = -0.4 vs. *z*/R location at *t* = 1 sec for Run 5.

A normalized Stanton number map of the heat shield for Run 5 at time t = 0.7 sec is depicted in Fig. 69. The comparison of Fig. 69 and Fig. 64 shows that the convective heating on the surface of the heat shield at 0.7 sec and 1 sec is virtually the same, which is the expected result since the Stanton number is expected to stay constant in time during the "good flow" portion of each run. Most of the differences in the surface heating pattern come from the hot "streaks" caused by small particles impacting the test article during a run, locally disturbing the boundary layer and increasing the heat flux, as was explained earlier. This phenomena is illustrated in Fig. 70 and Fig. 71, which show the heat transfer calculated from the TSP data and the thermocouple data from the baseline run along vertical section cuts at y/R = 0.55 and 0.7, respectively. The section cuts are also marked in Fig. 69 by the vertical dashed lines. The hot "streaks" in Fig. 69 appear as heating spikes in Fig. 70 and Fig. 71, which once again illustrates the TSP system's ability to effectively capture sharp spatial gradients and fine flow features which may be missed by

discrete instrumentation. Note that the majority of the thermocouples located along the two section cuts depicted in Fig. 70 and Fig. 71 happen to coincide with the increased heating areas due to the local boundary layer disturbances, so one-to-one comparison between the baseline thermocouple and the TSP data is not possible at those locations. The thermocouples that are not located in the areas of increased heating, however, track well with the TSP data.

The data reduction methodology employed here allows generating heat-transfer maps such as the ones in Fig. 55, Fig. 57, Fig. 64 and Fig. 69 at any instant in time during each run. Such heat-transfer maps for t = 0.6, 0.8, and 0.9 sec for Run 5 are shown in Fig. 72, Fig. 73, and Fig. 74, respectively.

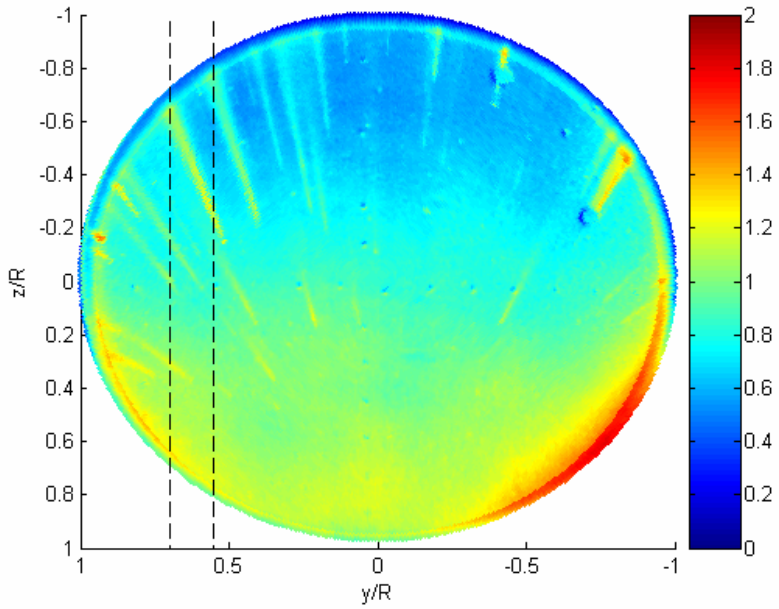

Fig. 69. Normalized Stanton number map at t = 0.7 sec for Run 5 (M_∞ = 10, Re = 5×10^6/ft); section cuts at y/R = 0.55 and 0.7 are marked with vertical dashed lines.

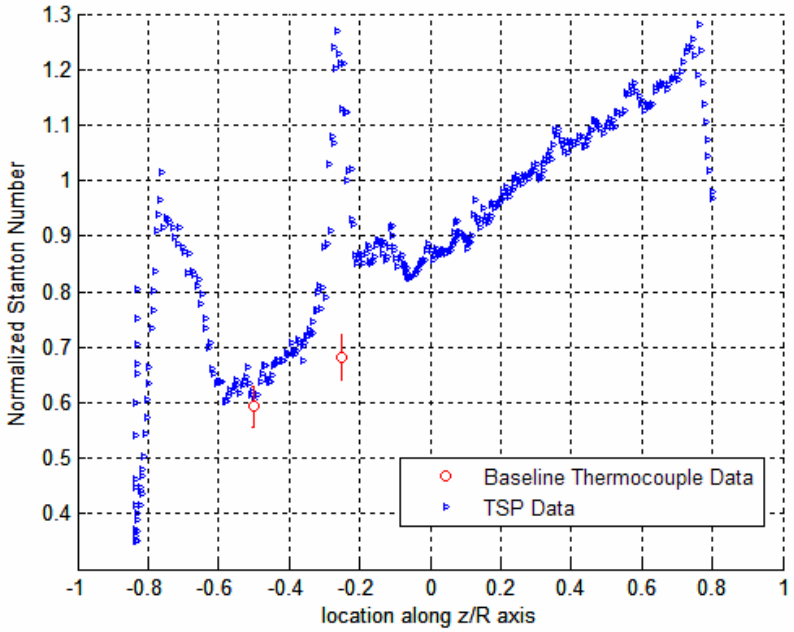

Fig. 70. Normalized Stanton number section cut at *y*/R = 0.55 vs. *z*/R location at *t* = 0.7 sec for Run 5.

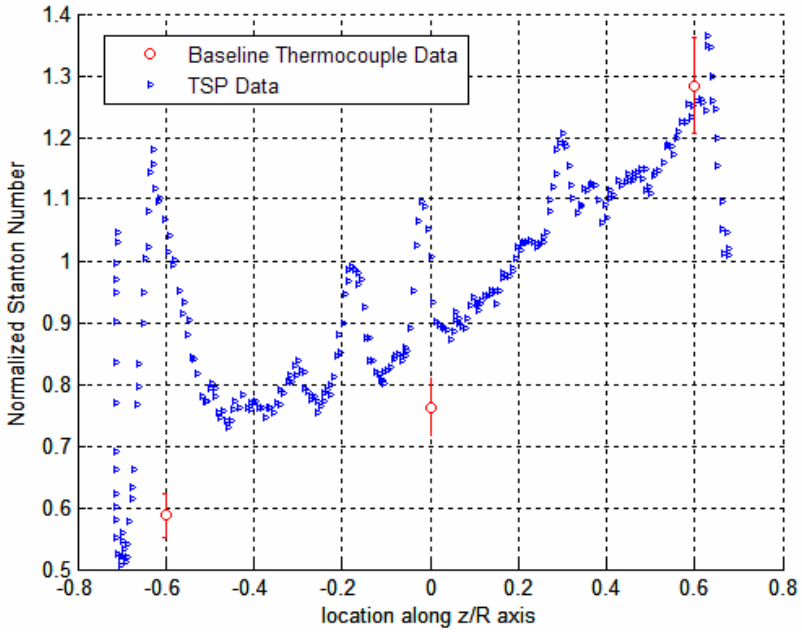

Fig. 71. Normalized Stanton number section cut at *y*/R = 0.7 vs. *z*/R location at *t* = 0.7 sec for Run 5.

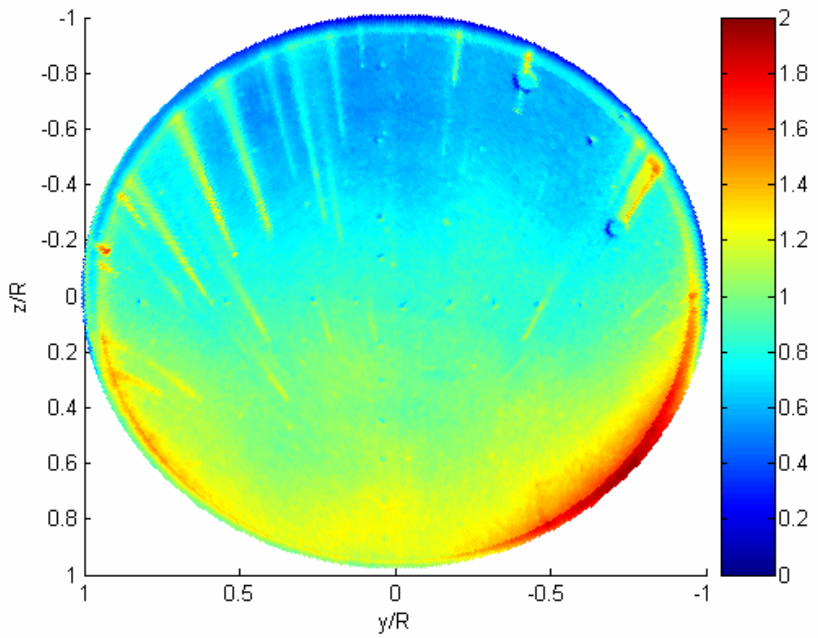

Fig. 72. Normalized Stanton number map at t = 0.6 sec for Run 5 (M_∞ = 10, Re = 5×10^6/ft).

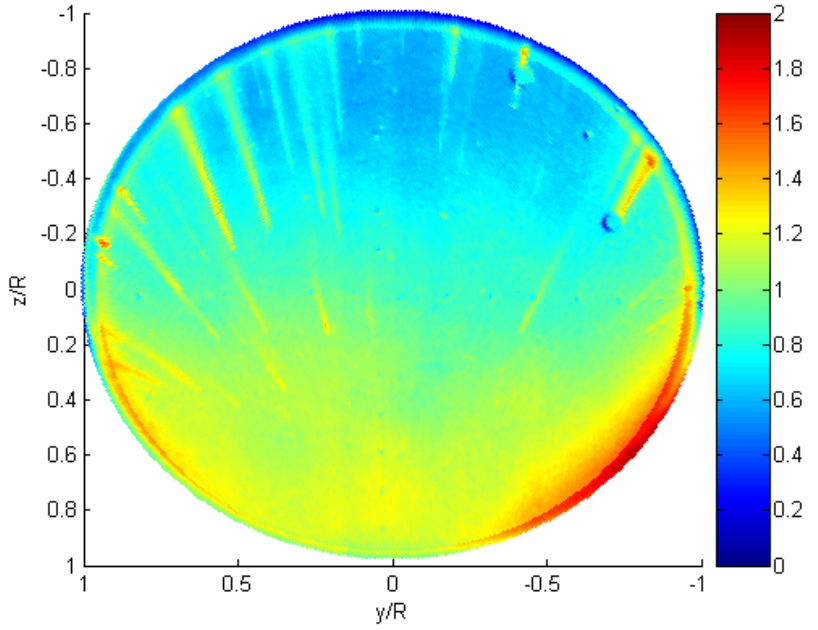

Fig. 73. Normalized Stanton number map at t = 0.8 sec for Run 5 (M_∞= 10, Re = 5×10^6/ft).

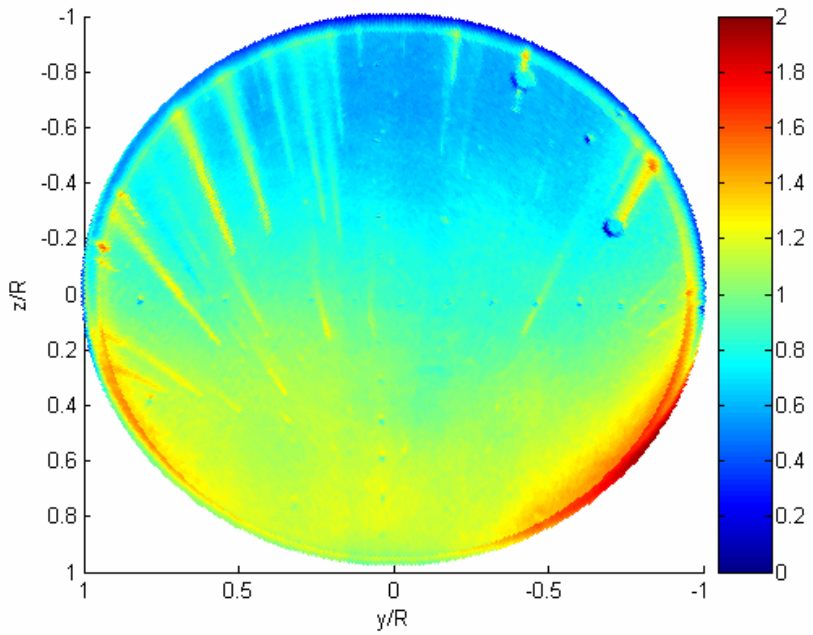

Fig. 74. Normalized Stanton number map at t = 0.9 sec for Run 5 (M_∞ = 10, Re = 5×10^6/ft).

4.3. Summary and Conclusions

A global quantitative intensity-based TSP heat-transfer measurement system was developed for the use in long-duration hypersonic facilities such as AEDC Hypervelocity Wind Tunnel No. 9. Several methodologies for reducing the TSP emission intensity/temperature data into convective heat flux were proposed. The proposed data reduction techniques are based on a single general approach, which takes into consideration the ramp-like heating profiles characteristic of blowdown facilities such as Tunnel 9 and can be used with metal test articles in long-duration flows. ANSYS finite-element modeling software was used to analyze the underlying assumptions of the data reduction approach and its sensitivity to perturbations in various measured quantities to determine its limitations. Namely, an analysis of the temperature gradient through the temperature-sensitive coating layer was conducted using the estimated TSP material properties.

It was found that for the majority of conditions tested at Tunnel 9 the error associated with the linear temperature gradient through the paint layer assumption is expected to be on the order of 1% during the "good flow" period, which is an encouraging result. The error analysis, however, was based on the assumed TSP properties and should be refined once a better estimate/measurement of the properties becomes available. The sensitivity of the data reduction algorithm to the accuracy of measured temperature-sensitive coating parameters, such as $K(T)$ and L, and also to various system parameters and real world effects, such as camera frame rate an noise, was examined.

The TSP system was used to collect the emission intensity data on a model of a NASA CEV capsule during a five-run test program at $M_\infty = 10$, $Re = 5\times10^6$/ft and $Re = 10\times10^6$/ft conditions. One of the data reduction methodologies was applied to obtain an estimate of the thermal conductivity of the paint as a function of temperature, and the resulting estimate was compared to the $K(T)$ values for a similar coating. Another data reduction methodology was applied to the TSP data from two of the runs at $M_\infty = 10$, $Re = 5\times10^6$/ft condition to obtain a number of high-resolution quantitative heat-transfer maps of the entire surface of the test article's heat shield. The resulting heat-transfer maps were validated against the heat flux calculated from the thermocouple data collected during a non-TSP run at the same conditions. The comparison revealed a good agreement between the two data sets over the majority of the model's surface for both of the runs, thus demonstrating the ability of the TSP system to provide high-resolution global quantitative convective heat-transfer measurements on metal wind tunnel models in long-duration hypersonic flows.

4.4. Suggestions for Future Work

The ability of the TSP system to provide high-resolution quantitative heat-transfer maps of the regions where the heat conduction can be assumed normal to the surface (i.e. 1D) has been demonstrated in the present work. The TSP system developed at Tunnel 9 can supply a quantitative heat-flux measurement anywhere on the model's surface where a coaxial thermocouple can since the data reduction methodologies for both are based on the same algorithm. One of the appeals of the global measurement techniques, such as TSP, however, is the potential to provide the heat-transfer measurements where a discrete sensor cannot be installed (e.g. sharp leading edges, fins) and also in the regions of high spatial heat-flux gradients. This can be done with the Tunnel 9 TSP system in its present form provided that a data reduction algorithm that accounts for 2D and 3D heat conduction effects, which are present in the aforementioned regions, is developed. The formulation of such algorithm, or of an appropriate correction scheme of the 1D data reduction algorithm for 2D and 3D effects, is the next step in the TSP system development effort at Tunnel 9.

A two-luminophore TSP is currently being developed for the use at Tunnel 9. The new formulation will eliminate the noise inherent in the present single-luminophore TSP system due to spatial-temporal variations in the illumination field on the surface of a test article, as discussed in Sections 3.5.3 – 3.5.4. Furthermore, the two-color paint would enable collecting the TSP data while dynamically pitching a model during a run since all of the changes in the illumination field will be corrected for by ratioing of the two wavelength components of the same image.

Finally, an accurate measurement of the temperature-dependent thermophysical properties (i.e. $K(T)$ and $\alpha(T)$) of the TSP formulation would allow using the 1st data reduction methodology described in Section 2.2.2 for the heat-transfer calculations. Additionally, new and more accurate data reduction algorithms could be devised if the TSP material properties are known. For instance, if both $K(T)$ and $\alpha(T)$ of the TSP formulation are known with sufficient accuracy, the temperature-sensitive coating layer could be divided into multiple nodes much like the steel model wall in the algorithms described in Chapter 2. Then, the nodal temperatures within the TSP layer could be solved for numerically and the linear temperature gradient through the paint layer assumption would no longer be necessary. Additionally, more accurate parametric finite-element studies could be performed to determine the effect of changing the paint layer thickness on the data reduction algorithms and on the behavior of the two-layer model wall subject to various heating loads.

References

[1] Blanchard, R. C., Anderson, B. P., Welch, S. S., Glass C. E., Berry, S. A., Merski, N. R., et al., "Shuttle Orbiter Fuselage Global Temperature Measurements from Infrared Images at Hypersonic Speeds," AIAA 2002-4702, AIAA Atmospheric Flight Mechanics Conference and Exhibit, Monterey, CA, 5 – 8 August 2002.

[2] Daryabeigi, K., "Global Surface Temperature/Heat Transfer Measurements Using Infrared Imaging," AIAA 92-3959, AIAA 17th Aerospace Ground Testing Conference, Nashville, TN, 6 – 8 July 1992

[3] Kontis, K., Yoshikawa, N., "Surface Thermography by Laser-Induced Fluorescence for Transient Heat Transfer Measurements in High-Speed Flows," AIAA-99-3170

[4] Horvath, T., Berry, S., Alter, S., Blanchard, R., Schwartz, R., Ross, M., et al, "Shuttle Entry Imaging Using Infrared Thermography," AIAA 2007-4267, 39th AIAA Thermophysics Conference, Miami, FL, 25 – 28 June 2007.

[5] Collier, A. S., Lafferty, J. F., Swinford, S. S., Witte, D. W., "Aerodynamic Heat Transfer Testing in Hypersonic Wind Tunnels using an Infrared Imaging System," AIAA-90-0189, 28th Aerospace Sciences Meeting, Reno, NV, 8 – 11 January 1990.

[6] Klein, E. J., and Margozzi, A. P., "Exploratory Investigation on the Measurement of Skin Friction by Means of Liquid Crystals," *Israel Journal of Technology*, Vol. 7, Nos. 1-2, 1969, pp. 173-180.

[7] Klein, E. J., "Application of Liquid Crystals to Boundary Layer Flow Visualization," AIAA Paper 68-376, Jan 1968.

[8] Schöler, H., "Application of Encapsulated Liquid Crystals on Heat Transfer Measurements in the Fin/Body Interaction Region at Hypersonic Speed," AIAA Paper 78-777, April 1978.

[9] Roberts, G. T., East, R. A., "Liquid Crystal Thermography for Heat Transfer Measurement in Hypersonic Flows: A Review," *Journal of Spacecraft and Rockets*, Vol. 33, No. 6, November – December 1996.

[10] Liu, T., Campbell, B. T., Sullivan, J. P., "Thermal Paint for Shock/Boundary Layer Interaction in Inlet Flows," AIAA 92-3626, AIAA/SAE/ASME/ASEE 28th Joint Propulsion Conference and Exhibit, Nashville, TN, 6 – 8 July 1992.

[11] Babinsky, H., Edwards, J. A., "The Application and Analysis of Liquid Crystal Thermographs in Short Duration Hypersonic Flow," AIAA 93-0182, 31st Aerospace Sciences Meeting & Exhibit, Reno, NV, 11 – 14 January 1993.

[12] Buck, G., "Surface Temperature/Heat Transfer Measurement Using A Quantitative Phosphor Thermography System," AIAA-91-0064, 29th Aerospace Science Meeting, Reno, NV, January 1991.

[13] Merski, N. R., "Global Aeroheating Wind-Tunnel Measurements Using Improved Two-Color Phosphor Thermography Method," *Journal of Spacecraft and Rockets*, Vol. 36, No. 2, March – April 1999.

[14] Watkins, A. N., Buck, G. M., Leighty, B. D., Lipford, W. E., Oglesby, D. M., "Using Pressure- and Temperature-Sensitive Paint for Global Surface Pressure and Temperature Measurements on the Aft-Body of a Capsule Reentry Vehicle," AIAA 2008-1230, 46th AIAA Aerospace Sciences Meeting and Exhibit, Reno, NV, 7 – 10 January 2008.

[15] Liu, T., Sullivan, J. P., *Pressure and Temperature Sensitive Paints*, Springer, New York, 2005.

[16] Hubner, J., Carroll, B., and Schanze, K., "Heat Transfer Measurements in Hypersonic Flow Using Luminescent Coating Techniques," AIAA 2002-0741, 40th AIAA Aerospace Sciences Meeting & Exhibit, Reno, NV, January 2002.

[17] Matsumura, S., "Streamwise Vortex Instability and Hypersonic Boundary-Layer Transition on the Hyper-2000," Master's Thesis, School of Aeronautics and Astronautics, Purdue University, West Lafayette, IN, Dec 2003.

[18] Hamner, M. P., "Demystifying Luminescent Paint Technology. A Guide for Non-Developers," AIAA 2001-2981, 31st AIAA Fluid Dynamics Conference & Exhibit, Anaheim, CA, 11 – 14 June 2001.

[19] Hamner, M. P., Norris, J. D., Lafferty, J. F., "Recent Developments in TSP/PSP Technologies Focusing on High Velocity-Temperature and Non-Oxygen Environments (Invited)," AIAA 2004-2187, 24th AIAA Aerodynamic Measurement Technology and Ground Testing Conference, Portland, OR, 28 June – 1 July 2004.

[20] Goss, L. P., Trump, D. D., Sarka, B., Lydick, L. N., Baker, W. M., "Multi-Dimensional Time-Resolved Pressure-Sensitive Paint Techniques: a Numerical and Experimental Comparison," AIAA 2000-0832, 38th Aerospace Sciences Meeting & Exhibit, Reno, NV, 10 – 13 January 2000.

[21] Drouillard II, T. F., Linne, M. A., "Luminescence Lifetime Response of Pressure-Sensitive Paint to a Pressure Transient," *AIAA Journal*, Vol. 43, No. 5, May 2005.

[22] Rabek, J. F., *Mechanisms of Photophysical Processes and Photochemical Reactions in Polymers*, Wiley, New York, 1987, Chap. 1.

[23] Strobel, H. A., Heineman, W. R., *Chemical Instrumentation: A Systematic Approach*, 3rd ed., Wiley, New York, 1989, Chap. 15.

[24] Berry, S. A., Horvath, T. J., Weilmuenster, K. J., Alter, S. J., Merski, N. R., "X-38 Experimental Aeroheating at Mach 10," *Journal of Spacecraft and Rockets*, Vol. 41, No. 2, March – April 2004.

[25] Roberts, G., East, R., "The Use of Thermochromic Liquid Crystals for Heat Transfer Measurement in Short Duration Hypersonic Wind Tunnel Facilities," AIAA-95-6115, AIAA 6th International Aerospace Planes and Hypersonics Technologies Conference, Chattanooga, TN, 3 – 7 April, 1995.

[26] Nakakita, K., Osafune, T., and Asai, K., "Global Heat Transfer Measurement in Hypersonic Shock Tunnel Using Temperature Sensitive Paint," AIAA Paper 2003-743, 41st Aerospace Sciences Meeting & Exhibit, Reno, NV, January 2003.

[27] Ohmi, S., Nagai, H., and Asai, K., "Effect of TSP Layer Thickness on Global Heat Transfer Measurement in Hypersonic Flow," AIAA Paper 2006-1048, 44th Aerospace Sciences Meeting & Exhibit, Reno, NV, January 2006.

[28] Ishiguro, Y., Nagai, H., Asai, K., Nakakita, K., "Visualization of Hypersonic Compression Corner Flows using Temperature- and Pressure-Sensitive Paints," AIAA 2007-118, 45th AIAA Aerospace Sciences Meeting and Exhibit, Reno, NV, 8 – 11 January 2007.

[29] Liu, T., Campbell, B. T., Sullivan, J. P., Lafferty, J., Yanta, W., "Heat Transfer Measurement on a Waverider at Mach 10 Using Fluorescent Paint," *Journal of Thermophysics and Heat Transfer*, Vol. 9, No. 4, October – December 1995.

[30] Ragsdale, W. C. and Boyd, C. F., *Hypervelocity Wind Tunnel 9 Facility Handbook* Third Edition, NAVSWC TR 91-616, Silver Spring, MD, July 1993.

[31] Norris, J., Hamner, M., Lafferty, J., Smith, N., and Lewis, M., "Adapting Temperature-Sensitive Paint Technology for Use in AEDC Hypervelocity Wind Tunnel 9," AIAA Paper 2004-2191, 24th AIAA Aerodynamic Measurement Technology and Ground Testing Conference, Portland, OR, 28 June – 1 July, 2004.

[32] Princeton Instruments, *PhotonMAX System User Manual Version 1.B*, 13 March, 2006.

[33] The Boeing Company, *Greenboot User Guide Version 2.10*. Contract NASI-20268, NASA, 1997.

[34] Boyd, C. F., and Howell, A., "Numerical Investigation of One-Dimensional Heat-Flux Calculations," Dahlgren Division, Naval Surface Warfare Center, Silver Spring, MD, 25 October 1994.

[35] Paul, K. C., Pal, A. K., Ghosh, A. K., and Chakraborty, N. R., "Thermal Measurements of Coating Films Used for Surface Insulation and Protection," *Surface Coatings International Part B: Coatings Transactions*, Vol. 87, B2, 71-148, June 2004.

[36] Kurits, I., Lewis, M., Hamner, M., Norris, J., "Development of a Global Heat Transfer Measurement System at AEDC Hypervelocity Wind Tunnel 9", 22nd International Congress on Instrumentation in Aerospace Simulation Facilities (ICIASF), Pacific Grove, CA, June 2007.

[37] Cattafesta III, L. N., Liu, T., Sullivan, J. P., "Uncertainty Estimates for Temperature-Sensitive Paint Measurements with Charge-Coupled Device Cameras," *AIAA Journal*, Vol. 36, No. 11, November 1998.

[38] Goodson, K. E., Ju, Y. S., "Heat Conduction in Novel Electronic Films," *Annual Review of Materials Science*, 29: 261-293, 1999.